BURIED WIRE DETECTION USING GROUND PENETRATING RADARS

A THESIS SUBMITTED TO
THE GRADUATE SCHOOL OF NATURAL AND APPLIED SCIENCES
OF
MIDDLE EAST TECHNICAL UNIVERSITY

UTKU YILMAZ

IN PARTIAL FULFILLMENT OF THE REQUIREMENTS
FOR
THE DEGREE OF MASTER OF SCIENCE
IN
ELECTRICAL AND ELECTRONICS ENGINEERING

JULY 2017

Approval of the thesis:

BURIED WIRE DETECTION USING GROUND PENETRATING RADARS

submitted by **UTKU YILMAZ** in partial fulfillment of the requirements for the degree of **Master of Science in Electrical and Electronics Engineering Department, Middle East Technical University** by,

Prof. Dr. Gülbin Dural Ünver
Dean, Graduate School of **Natural and Applied Sciences** ____________

Prof. Dr. Tolga Çiloğlu
Head of Department, **Electrical and Electronics Engineering** ____________

Prof. Dr. Gözde Bozdağı Akar
Supervisor, **Electrical and Electronics Engineering, METU** ____________

Examining Committee Members:

Prof. Dr. Gönül Turhan Sayan
Electrical and Electronics Eng. Dept., METU ____________

Prof. Dr. Gözde Bozdağı Akar
Electrical and Electronics Eng. Dept., METU ____________

Prof. Dr. Çağatay Candan
Electrical and Electronics Eng. Dept., METU ____________

Prof. Dr. Ziya Telatar
Electrical and Electronics Eng. Dept., Ankara University ____________

Assoc. Prof. Dr. İlkay Ulusoy
Electrical and Electronics Eng. Dept., METU ____________

Date: ____________

I hereby declare that all information in this document has been obtained and presented in accordance with academic rules and ethical conduct. I also declare that, as required by these rules and conduct, I have fully cited and referenced all material and results that are not original to this work.

Name, Last Name: UTKU YILMAZ

Signature :

ABSTRACT

BURIED WIRE DETECTION USING GROUND PENETRATING RADARS

YILMAZ, Utku
M.S., Department of Electrical and Electronics Engineering
Supervisor : Prof. Dr. Gözde Bozdağı Akar

July 2017, 134 pages

Buried explosives pose great threat for national security of the countries struggling with these explosives as the damage caused by them increase day by day. There are several sensors developed for detection of buried explosives such as land mines, unexploded ordnances and improvised explosive devices (IEDs). Among these, IEDs are quite hard to detect with majority of sensors due to their irregular shape and contents. The difficulties in IED detection have led researchers to aim the triggering mechanisms of IEDs. As the new jamming systems in the military industry can successfully block the wireless control links of IEDs, the threat has shifted to the use of command wires. So, the detection of buried command wires become a critical ability for buried explosive detection systems.

Ground penetrating radars have shown their capabilities on detection of buried objects in many operational concepts. Ground penetrating radars can construct the 3-D image of the subsurface medium with high spatial and temporal resolution and distinguish objects with different electromagnetic properties.

In this thesis, wire detection problem is studied using ground penetrating radars. Firstly, extensive simulations are carried out on gprMax software, a powerful open source FDTD simulation environment, by changing simulation parameters such as transmitting frequency, electromagnetic properties of soil and clutter, depth and radius of wire, in order to observe the effects of these parameters. Then, a simulated 3-D GPR database is generated consisting of wires in different orientations together with different types of clutter. In the second step, wire detection and classification problem is studied. The possible wire locations are found using a morphologically improved version of 2-D LMS filtering. Then a novel 3-D feature set is extracted with the help of 3-D curve reconstruction algorithm. Using the generated database, SVM classifier is trained and the performance of proposed algorithms is shown.

Keywords: Ground Penetrating Radar, Detection, Feature Extraction, Classification, Wire Detection

ÖZ

YERE NÜFUZ EDEN RADARLAR İLE GÖMÜLÜ TEL TESPİTİ

YILMAZ, Utku
Yüksek Lisans, Elektrik ve Elektronik Mühendisliği Bölümü
Tez Yöneticisi : Prof. Dr. Gözde Bozdağı Akar

Temmuz 2017 , 134 sayfa

Yere gömülü patlayıcıların neden olduğu hasar günden güne artmakta; bu da bu patlayıcılar ile mücadele içinde olan ülkelerin milli güvenliği için tehdit oluşturmaktadır. Mayın, patlamamış mühimmat ve el yapımı patlayıcı (EYP) gibi yere gömülü patlayıcıların tespiti için çeşitli sensörler geliştirilmiştir. Bu patlayıcılar arasında, EYP'lerin boyut ve içeriklerinin çok çeşitli olması, EYP'lerin tespit edilmesini güçleştirmektedir. Tespit konusundaki bu problemler, araştırmacıları EYP tetik mekanizmalarını hedeflemeye yönlendirmiştir. Askeri sanayideki yeni karıştırıcı sistemler ile kablosuz kontrol bağlantıları engellenebildiği için tehdit, kablolu tetik mekanizmalarının kullanımına yönelmiştir. Bu nedenle, yere gömülü komuta tellerinin tespiti, yere gömülü patlayıcı sistemleri için çok kritik bir yetenek olmaktadır.

Yere nüfuz eden radarlar, yere gömülü objelerin tespitindeki kapasitelerini çeşitli operasyonel konseptlerde göstermiştir. Yere nüfuz eden radarlar, yer altı ortamının yüksek uzamsal ve zamansal çözünürlükte 3 boyutlu görüntüsünü oluştu-

rabilmekte ve farklı elektromanyetik özellikteki objeleri ayırt edebilmektedirler.

Bu tezde, yere nüfuz eden radarlar ile tel tespiti problemi üstüne çalışılmıştır. Öncelikle, güçlü bir açık kaynak sonlu farklar yöntemi yazılımı olan gprMax ile benzetim parametrelerinin etkilerini inceleme amacıyla yayın frekansı, toprağın ve diğer objelerin elektromanyetik özellikleri, telin çapı ve derinliği gibi benzetim parametreleri değiştirilerek detaylı benzetimler yapılmıştır. Ardından farklı tel ve kargaşa konumları için 3 boyutlu bir veri kütüphanesi hazırlanmıştır. Tezin ikinci bölümünde, tel tespit ve tehis problemi çalışılmıştır. Matematiksel biçimsellik ile iyileştirilmiş 2 boyutlu LMS ile olası tel konumları ön görüntülenmiştir. Ardından, 3 boyutlu eğri oluşturma metodu ile, yenilikçi bir 3 boyutlu öz nitelik kümesi çıkarılmıştır. Veri kütüphanesi ile, SVM sınıflandırıcısı eğitilmiş ve önerilen metotların performansları incelenmiştir.

Anahtar Kelimeler: Yere Nüfuz Eden Radar, Tespit, Öznitelik Çıkarımı, Sınıflandırma, Tel Tespiti

To my mother and father

ACKNOWLEDGMENTS

First of all, I would like to extend my sincere gratitude to my supervisor, Prof. Dr. Gözde Bozdağı Akar, for her valuable comments and advices throughout my study. Her guidance enlightened my way from the beginning till the completion of this thesis.

Secondly, I would like to thank ASELSAN for providing high power computing server and I thank my colleagues for sharing their valuable ideas.

I would like to thank TUBITAK BIDEB, for the 2210/A scholarship that they have provided.

I would also like to express my deepest gratitude for my parents, Necmiye and İsmail Yılmaz. Their top priority was my education from the beginning and without their support I wouldn't be able to reach this far. And finally, I would like to thank Hazal for her support. I completed this thesis mostly by her side, studying together.

TABLE OF CONTENTS

LIST OF TABLES

TABLES

LIST OF FIGURES

FIGURES

List of Algorithms

LIST OF ABBREVIATIONS

2-D 2 Dimensional

3-D 3 Dimensional

AP Anti-Personnel

EMI Electromagnetic Induction

FDTD Finite Difference Time Domain

GPR Ground Penetrating Radar

GSOM Growing Self Organized Maps

HF High Frequency

HPC High Power Computing

ICA Independent Component Analysis

IED Improvised Explosive Device

IR Infra-red

KLMS Kernel Least Mean Squares

LIDAR Laser imaging detection and ranging

LMS Least Mean Squares

MIMO Multiple Input Multiple Output

MLS Moving Least Squares

NN Nearest Neighbour

PCA Principal Component Analysis

RBF Radial Basis Function

RF Radio Frequency

ROC Receiver Operating Characteristics

RPCA Robust Principal Component Analysis

RX Receiver

SAR Synthetic Aperture Radar

SFCW Stepped Frequency Continuous Wave

SVD Singular Value Decomposition

SVM Support Vector Machine

T/R   Transmit and Receive

TX   Transmitter

UNIDIR   United Nations Institute for Disarmament Research

UXO   Unexploded Ordnance

CHAPTER 1

INTRODUCTION

1.1 The Concept of Humanitarian Demining

Humanitarian demining of various explosives is a serious problem for the countries those have struggled in major wars like World War II and those are struggling with asymmetric warfare. There are still millions of buried explosives scattered around the world [1], [2]. The explosives that are buried underground can be mainly divided into three groups; landmines, unexploded ordnances (UXO) and improvised explosive devices (IED).

The landmines are produced in different sizes; such as anti-tank landmines and anti-personnel landmines. In Ottawa Convention, 1999, the use and stockpiling of anti-personnel landmines are prohibited [1]. But still there are millions of landmines buried underground unexploded . Anti-tank landmines are triggered with great pressure, or magnetically; aiming to damage tanks and armoured heavy vehicles. Anti-personnel landmines on the other hand, are triggered with very little pressure and aims to kill or maim the person stepping on the landmine. As the detection technology advances, the metal content of the mines gets lower for minimum detectability. For instance, there exist minimum metal landmines that are quite hard to detect with electromagnetic induction (EMI) sensors. Although their size and metal content differ a lot; they share the very same structure in general. Their shape observed with an underground imaging sensor mainly shares the same characteristics, which creates a framework that allows the classification of mines from any form of clutter.

UXOs are the unexploded remains of warfare, such as missiles and various kinds of bombs. There still exist many UXOs in the heavily bombed areas of major wars such as World War II and they pose a great danger for construction industry. Their shape and size differ a lot. Yet, the areas possibly containing UXO are known; and with some extra carefulness; these UXO can be detected and demined well. Since the conflict is over at these areas, demining missions are not time critical. However, despite being not time critical, UXOs are still perilous. UN (United Nations) statistics have shown that two deminers dies for every 1000 UXOs demined as stated in [3].

The IEDs, also known as the handmade explosives however is a great problem in case of an asymmetric warfare. They can be created in any shape and any size. Also very simple and easy to find materials can be used for creating IEDs. Therefore detection of such explosives is a great problem for humanitarian demining [4]. The IEDs can be detonated with various ways. UNIDIR (United Nations Institute for Disarmament Research) classifies IEDs under three triggering mechanisms [5], namely victim operated, time operated and command operated IEDs.

The victim operated IEDs are designed to detonate when the victim contacts the triggering mechanism. When enough precautions are taken, these kind of IEDs are safe to demine mostly.

Another triggering mechanism is time operated IEDs. These IEDs are detonated with an alarm, or a timer. These IEDs are commonly seen inside cities; rather than the roads in rural areas.

The last triggering mechanism is command operated IEDs. These IEDs are the most dangerous and harmful ones since they are triggered with exact timing to cause the highest impact on the target. They pose a great challenge for IED detection in rural areas. The command operated IEDs can be divided into three subsections. Infra-red controlled IEDs works like victim operated IEDs; they are triggered when the victim blocks the light beam. The radio / remote controlled IEDs are triggered with electromagnetic waves such as car alarms, wireless sensors, cell phones, pagers, radios. The common countermeasure for these IEDs is jammers. The new jamming systems in the military industry can successfully block the triggering signal. The last command type is command wire operated IEDs. These IEDs can be commanded from great distances. They cannot be jammed effectively, and they can be triggered with exact timing; which would cause great harm. As there is a lack in countermeasures for command wire operated IEDs, these IEDs poser a great challenge for humanitarian demining.

1.2 Sensors and Methods Used for Landmine, IED and UXO detection

Landmines, UXOs and IEDs can be detected by using many different sensors. These sensors can be listed as ground penetrating radars (GPR), infra-red (IR) and hyper spectral cameras, electromagnetic induction (EMI) sensors, magnetometers, acoustic and seismic sensors, nuclear quadrupole resonators, X-ray backscattering sensors and even the biological methods including dogs, bees and fungi [6]. The list can be extended further including radiometers, trace explosive detection systems, neutron based methods and remote sensing systems [7]. All these sensors have their pros and cons.

Ground penetrating radars can detect objects that have different electrical properties than the general soil profile. GPR detections also includes the depth information. The detection range varies from very shallow points to the mid range for an anti-personnel (AP) landmine. The detection range can be extended for massive objects. On the other hand, hardware design of ground penetrating radars can be quite complex compared to majority of other sensor types.

The infra-red (IR) and hyper spectral cameras can also be used for explosive detection [8]. These electro-optical sensors can successfully detect the anomalies on the soil surface at a large distance. Therefore, they are quite useful to detect the explosives betimes, without approaching the explosive, when explosives are shallowly buried or recently buried and left an anomaly on the soil surface. However, when the explosives are buried deeper these cameras fail to detect these objects. Also, if the explosives are buried long ago, then the anomalies on the soil surface disappear and it becomes impossible to detect these explosives.

Electromagnetic induction sensors, also known as the metal detectors, are one of the oldest methods used for landmine detection. They can locate the metal particles buried under ground. They have the greatest detection range compared to all other sensors; they can locate massive metal particles buried very deep. Also the EMI sensors with differential coil structures can detect very small metal particles. However, most EMI designs are not capable of finding the depth of objects. Also EMI sensors struggle at detecting the minimum metal landmines.

Magnetometers are passive sensors that sense the small anomalies in the magnetic field of the earth. However, they can't be used with other active electromagnetic sensors. Therefore, their usage in terms of hybrid solutions are limited.

In addition to these, acoustic and seismic sensors can be used for explosive detection as well. However, the major problem of these sensors is that very low percentage of the acoustic waves penetrate the soil due to air to ground interference. Moreover, seismic sensors are quite infeasible for moving vehicle detection systems.

Nuclear quadrupole resonators and X-ray backscattering sensors are some other alternatives that can be used for explosive detection; yet their performance is debatable and only a few examples are seen in the industry.

The biological methods, especially dogs are used commonly for explosive detection. Also, rats are being used for landmine and UXO detection. For instance, Apopo organization [9], states that they have demined over 100.000 landmines and UXOs using rats.

The fusion of all these sensors used for explosive detection generally shows an improvement in the detection capability of the system. For instance, the fusion of GPR and EMI is widely studied in both literature [10] and industry. In [11], a context dependent EMI and GPR sensor fusion method is suggested for landmine detection. Moreover, fusion of IR cameras with GPR is also another hot topic in the literature [8].

Along all these sensors, GPRs have shown their potential in terms of detecting the explosives regardless of the metal content of explosives and locating explosives in 3-D with a high precision at the cost of complex hardware and software design.

1.3 Wire Detection Problem

Although, GPRs are capable of detecting various objects underground, detection of IEDs is still a major problem for GPRs due to the irregular shapes and contents of IEDs [4]. Therefore, researchers aim to detect or block the remote command links of IEDs rather than detecting the IEDs. As the new jamming systems achieve a high success rate of blocking wireless command links, the threat has shifted to wired command links. As a consequence, the need to develop a system capable of detecting command wires has urged [12]. In the literature, to the best of our knowledge, there are a few studies focusing on the command wire detection problem.

In [13], antenna and hardware design problem for buried wire detection is studied. The hybrid dual polarization system has one spiral antenna for transmitting and two vivaldi antennas for receiving, placed perpendicular to each other. The system works in the frequency band starting from 1.2 GHz to 4 GHz and it's placed 3 cm above the ground surface. The wires, having diameter of 3 mm and length of 80 cm are buried 15 cm deep inside the soil with $\epsilon_r = 4$. Only a B-scan data is collected using the system, with the step size of 1 cm. The hyperbola signatures caused by wire scattering are observed in the B-scan data. However, this study only focuses on the hardware design of the GPR; therefore the detection and classification of wires are not investigated. Moreover, [13] is the only study that focuses on the detection of buried wires, to the best of our knowledge.

In [14], different measurements are conducted for command wire detection using electromagnetic waves in anechoic chambers in air medium. The study has concluded that use of circular polarization is best for linear object detection.

In [12], unburied command wire detection problem is studied using LIDARs (laser imaging detection and ranging). The study has shown that LIDARs can be used for detection of command wires having diameter at least 3 mm. The study has also shown the image processing algorithms for detecting linear objects in LIDAR images.

Also, there is a patent application, [15], for a frequency stepped forward looking sensor in HF (high frequency) band. However, the details regarding the system design is missing and the concept is unclear in the patent application.

In [16], detection of unburied thin wires is investigated using forward looking multiple input multiple output synthetic aperture radar (MIMO SAR). The experimental set-up successfully detected the IED command wires with diameter of 0.98 mm, which are placed on the ground surface. Detection of buried wires is not investigated in this study, but the authors conclude that the detection of buried wires is much harder. The reason behind the difficulty mentioned is not stated explicitly in the paper. However, it is likely that the height of the antenna being more than 2 meters and the forward looking structure play a role in the penetration performance of the GPR.

Pipe detection is studied in the literature ([17], [18]) for urban uses of ground penetrating radar; yet the diameter of pipes are quite large compared to command wires. Moreover, wires are electrically very thin, compared to the wavelength of the electromagnetic waves propagating in the soil medium. However, diameter of pipes are generally comparable with the wavelength of the electromagnetic waves. Therefore, the problem cannot be considered as linearly scalable in this concept.

There are some hand-held cable detector devices in the military industry yet their performance are not proven. Even, some producers avoid publishing the sensor types used in these devices; which leaves a big question mark behind.

The antenna design of GPR is different but highly related topic. In [19], the antenna design is studied for maximizing signal returns from different objects. It concludes that, antenna footprint plays significant role in detection of long metal pipes. Also, it investigates the effects on the return signal with different angles of metal pipe.

1.4 Scope of the Thesis

The scope of this thesis is to investigate the buried command wire detection problem using ground penetrating radars and to propose signal processing algorithms for detection and classification of buried wires.

Firstly, a database of 2-D (B-scan) and 3-D (C-scan) GPR data is generated by gprMax software, a powerful 3 Dimensional Finite Difference Time Domain (3-D FDTD) simulation environment. The effects of various simulation parameters and the characteristics of the buried wires are investigated extensively.

Then, command wire detection problem is investigated, which is divided into six steps; ground bounce and mutual coupling removal, depth weighing, prescreening, curve reconstruction, feature extraction and classification. Morphologically Improved 2-D LMS prescreener is proposed for detection of possible wire locations. A novel 3-D curve based feature extraction method is proposed. The extracted features are used for training and testing of classifier. Performance of proposed algorithms is shown. The flowchart of the processing methods are presented in Figure 1.1.

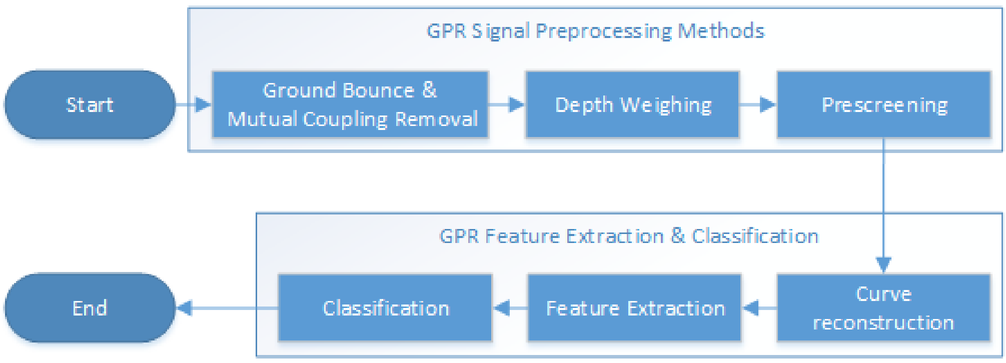

Figure 1.1: Flowchart of the processing methods

1.5 Outline of the Thesis

In Chapter 1, firstly, an overall information is presented about humanitarian demining activities, including different sensor types to detect various kinds of explosives. The studies in the literature related with command wire detection problem is summarized afterwards. Then, the scope of thesis is explained and the outline of thesis is presented.

In Chapter 2, the basics of ground penetrating radar is introduced. The problem definition regarding the scope of thesis is explained in detail.

In Chapter 3, firstly, the simulation environment is defined. Then, the analysis on simulation parameters are presented in order to observe the possible effects regarding different parameters. Then, the C-scan simulations are explained in detail.

In Chapter 4, the preprocessing methods are presented, which are divided into three steps. In the first step, the ground bounce signal and mutual coupling is eliminated. In the second step, the attenuation effect occurring along depth axis is normalized. In the last step, possible wire locations are detected using prescreening algorithm.

In Chapter 5, the classification problem is studied, which is divided into three steps. In the first step, the free form 3-D curve of wire detections is reconstructed. In the second step, a novel set of 3-D features are extracted using the reconstructed curve and the original detections. In the last step, a feature based classification algorithm is used for classifying objects. After all these, the performance of the overall algorithm chain is evaluated.

In Chapter 6, the thesis is summarized with few words, the final remarks are discussed to conclude the thesis and the possible future works are suggested.

CHAPTER 2

BACKGROUND INFORMATION AND PROBLEM DEFINITION

Ground penetrating radars are active electromagnetic sensors that transmits electromagnetic waves in a frequency band into the air medium. The waves penetrate into the ground and propagate in the subsurface medium. They scatter as they propagate and gets reflected at certain discontinuities in the subsurface medium. Presence of an object which has different electromagnetic properties than the general soil profile would make a discontinuity in the electromagnetic profile of the soil. These reflections are received by the receiving antenna element. The basics of ground penetrating radar is well described in [20] and [21].

The wire detection problem using GPR can be modelled as in Figure 2.1. The radar, which has multiple transmitting and receiving antennas (T/R pairs), is mounted on a platform, such as a ground vehicle. The dimension that antennas are stacked is called cross-track dimension, the movement direction is called as along-track dimension and the time axis is mapped to depth axis. The antenna array is held up at a predefined height above the surface. A thin wire is placed in a free form inside the soil medium. GPR antenna array transmits and receives the electromagnetic waves as it moves in along-track dimension.

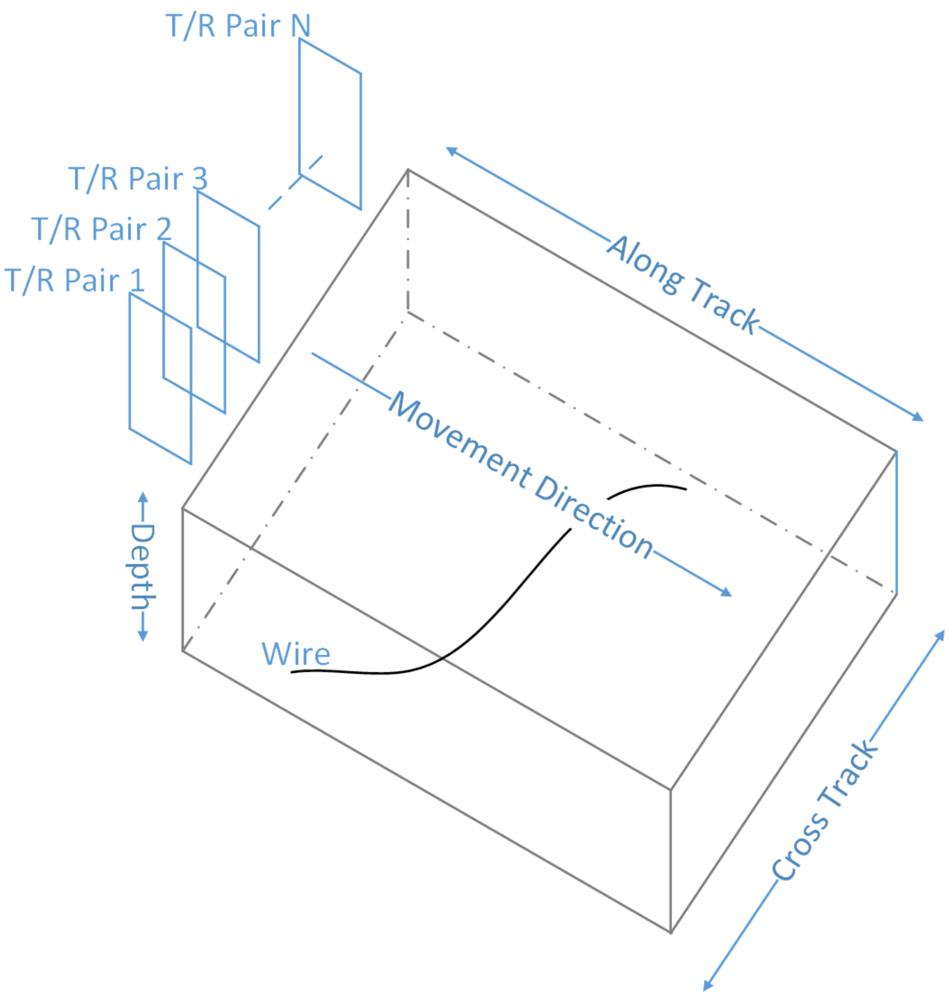

Figure 2.1: The problem definition for command wire detection using GPR

2.1 Electromagnetic Wave Propagation Model

The basic idea of wave propagation is presented in Figure 2.2. The received signal is divided into three categories; mutual coupling, ground bounce and target signals.

In each transmit/receive (T/R) pair, the transmitting (TX) element will radiate the electromagnetic waves. A portion of waves will be directly received by the receiving (RX) element, which is the mutual coupling signal numbered as (1) in the Figure 2.2.

The waves will also reach the ground surface. Majority of the waves will get reflected at the surface, and received by the RX element, which is the ground bounce signal numbered as (2) in Figure 2.2.

The remaining waves will penetrate into the soil and propagate and scatter in this lossy medium. When the waves reaches a distinct discontinuity in the electromagnetic profile of the soil medium, such as a wire, waves will get reflected at this point, propagates in soil and air and finally received by RX element. This is the target reflection numbered as (3) in Figure 2.2.

There also exist subsurface reflections, which is not presented in Figure 2.2. As the electromagnetic waves propagate inside soil, waves also scatter back and received by RX element.

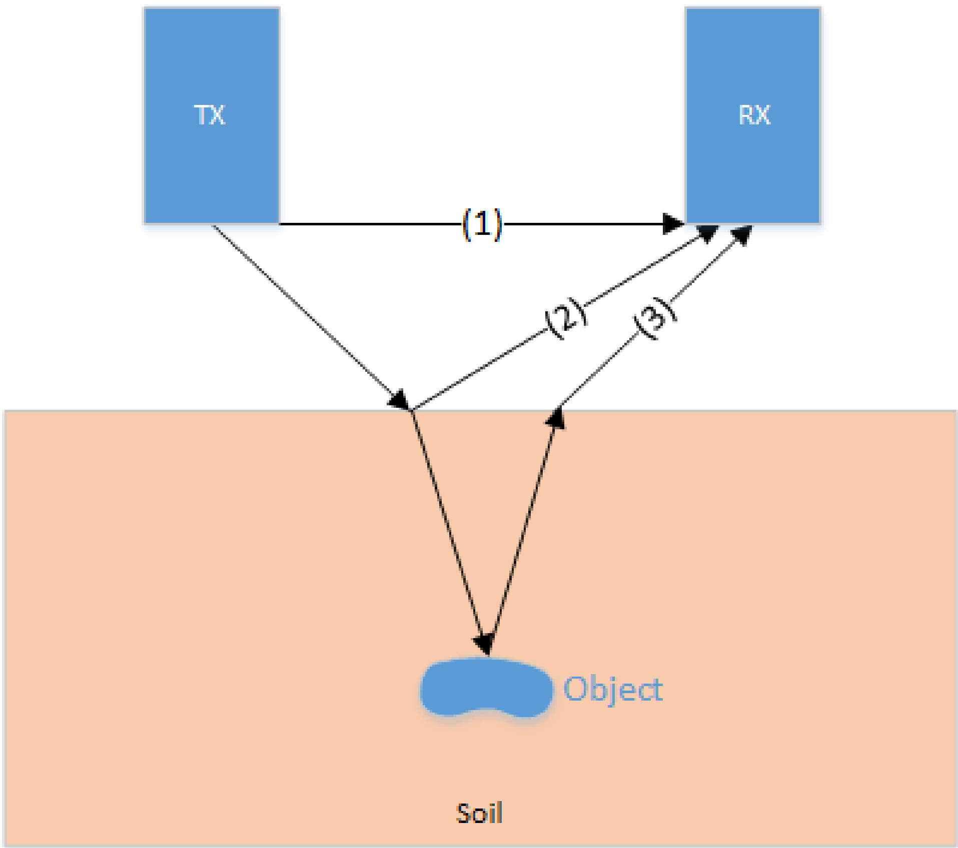

Figure 2.2: Electromagnetic wave propagation model of GPR, where the received signals are divided into three categories; the mutual coupling signal (1), the ground bounce signal (2) and the target reflection (3)

2.2 Definition of GPR Data Outputs

2.2.1 Definition of A-scan

This transmitting and receiving process, explained in Electromagnetic Wave Propagation Model section, for a single pair at a single location is called A-scan, as described in Figure 2.3; which is a time domain data modelling the backscatters in depth direction.

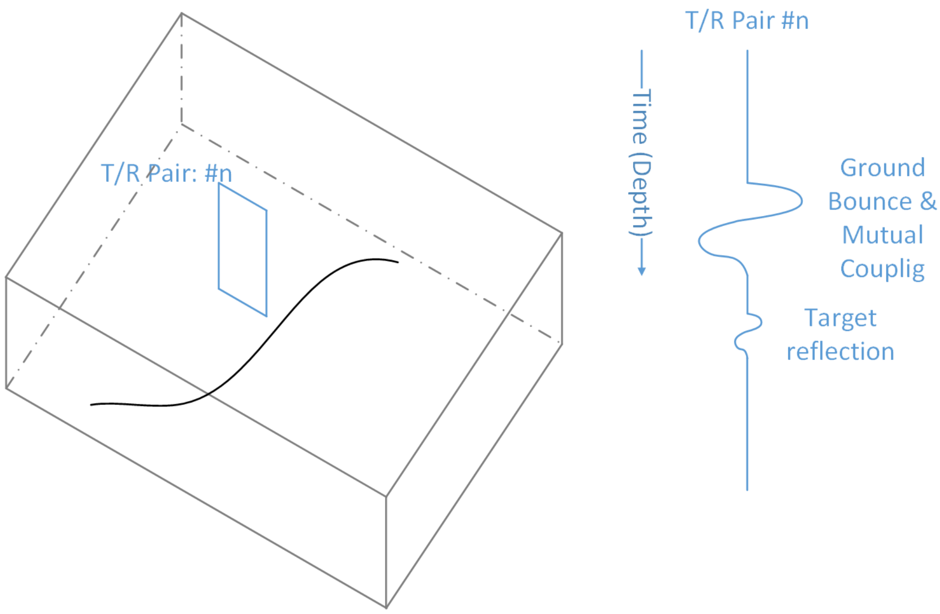

Figure 2.3: Description of GPR A-scan

A sample raw A-scan data is presented in Figure 2.4. The target reflection is not visible since ground bounce and mutual coupling signals, occurring at the early time indices, dominate the signal. Ground bounce and mutual coupling removal algorithm which is explained in detail in Chapter 4 is applied on the data. After the ground bounce and mutual coupling removal, the target reflection becomes visible as presented in Figure 2.5.

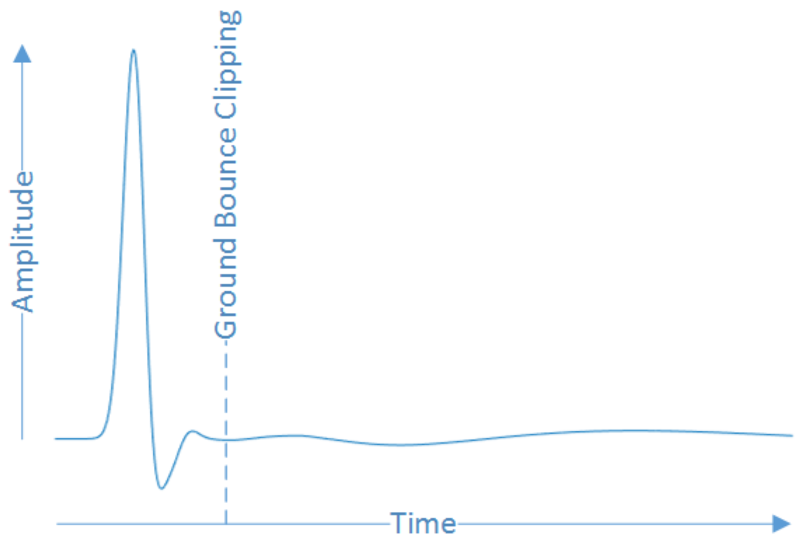

Figure 2.4: Raw A-scan data. Since mutual coupling and ground bounce dominates the signal, the target reflection is not visible at all.

Figure 2.5: A-scan data, after ground bounce and mutual coupling removal. The target reflection becomes visible after the removal.

2.2.2 Definition of B-scan

The sensor array stands perpendicular to the along track direction, parallel to the ground. The direction that antenna array is aligned is called as cross-track. The output of a sensor array is called B-scan as shown in Figure 2.6, which is the combination of all transmit/receive pairs in the antenna array. Alternatively, B-scan can be defined such that it is the combinations of the A-scans for a single transmit/receive pair as it moves in along-track direction. Briefly, the B-scan is a 2-D data which is the combinations of A-scans at several cross-track, or alternatively, along-track positions.

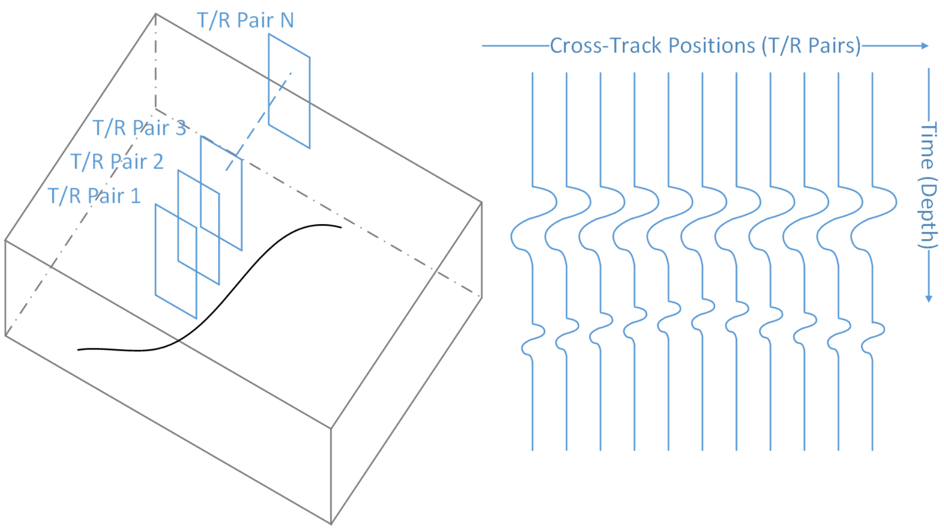

Figure 2.6: Description of GPR B-scan

A sample B-scan simulation output is given in Figure 2.7 and 2.8. In Figure 2.7, the raw data is presented; which is mainly dominated by the ground bounce signal and mutual coupling signals defined earlier occurring in the early time samples. As a result, target reflection is merely visible in Figure 2.7. Ground bounce and mutual coupling signals, as stated previously, are major components of raw GPR data. These two signals occur at the early time indices of RX sampling and dominate the GPR data generally. In Figure 2.8, the ground bounce and mutual coupling signals are removed. After the removal, the target reflection becomes much more visible.

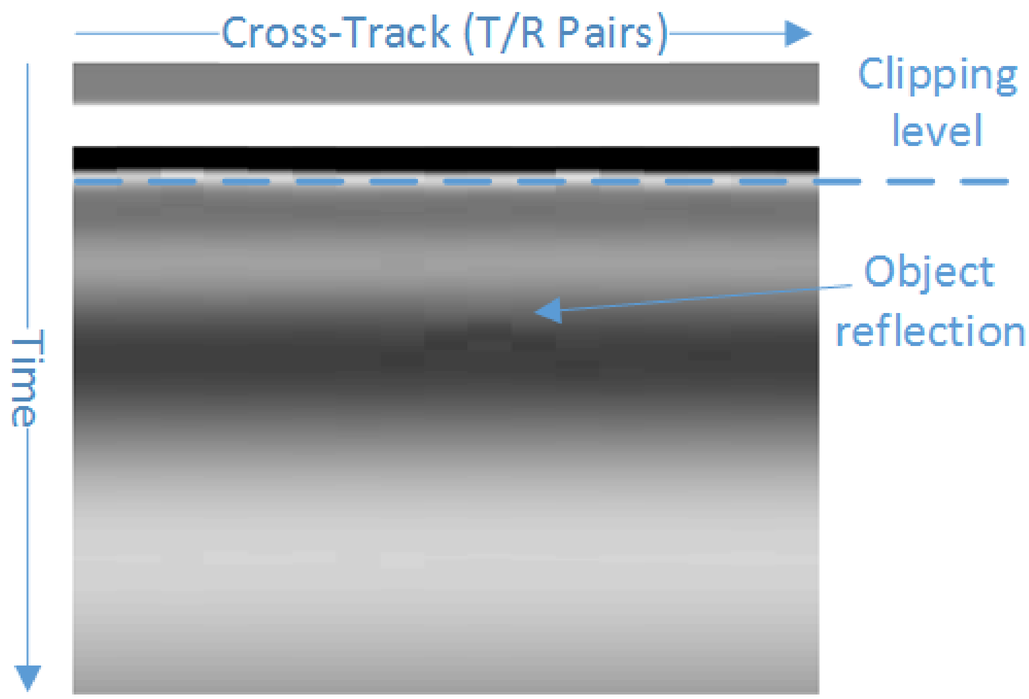

Figure 2.7: Raw B-scan data. Since mutual coupling and ground bounce dominates the signal, the target reflection is not visible at all.

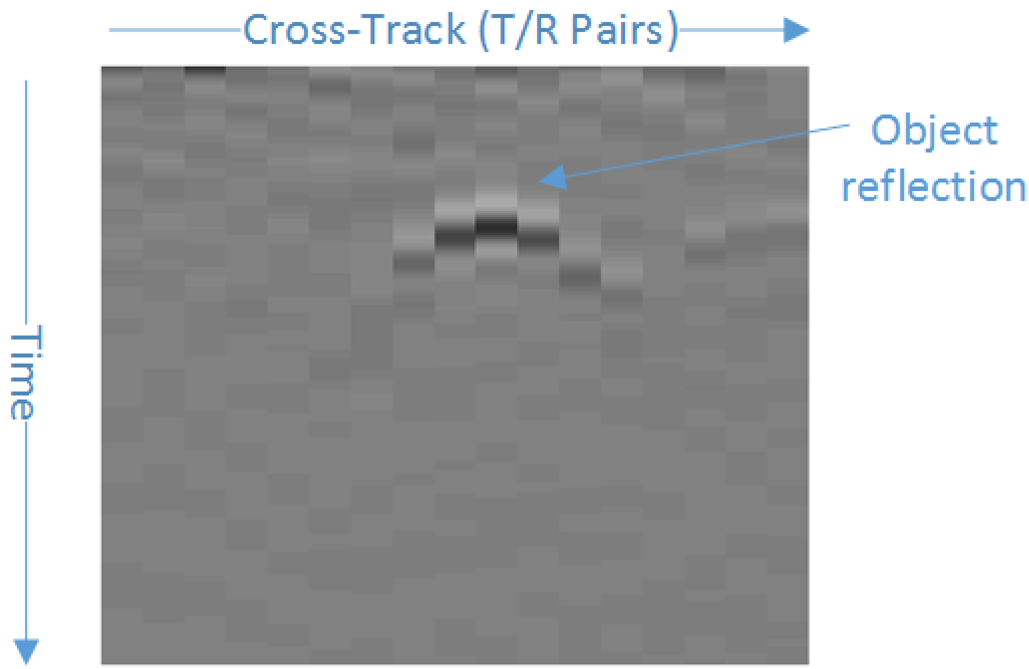

Figure 2.8: B-scan data, after ground bounce and mutual coupling removal. The target reflection becomes visible after ground bounce removal.

2.2.3 Definition of C-scan

The B-scan is usually collected using an antenna array. Therefore, whole data is collected at one time instant. In order to create the third dimension, the antenna array is moved in the along-track direction. As the vehicle moves, antenna array collects data for several along-track positions as shown in Figure 2.9. The combination of the data collected from all transmit/receive pair for several along track positions creates the C-scan data, which is a 3-D data as shown in Figure 2.10.

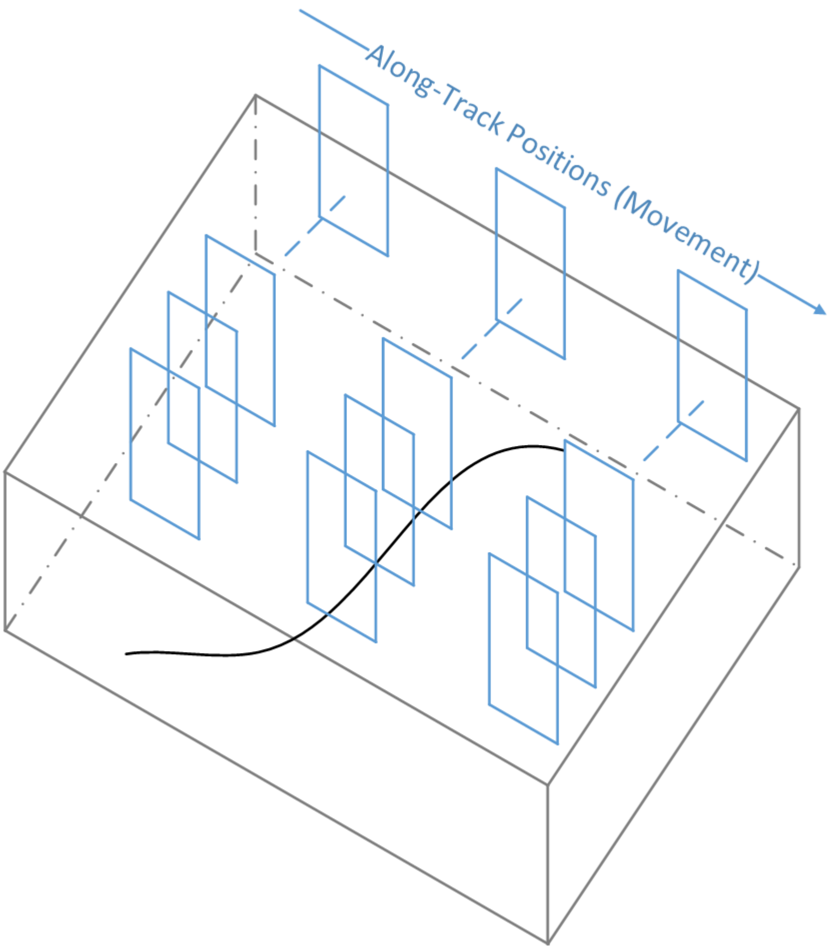

Figure 2.9: C-scan data acquisition model

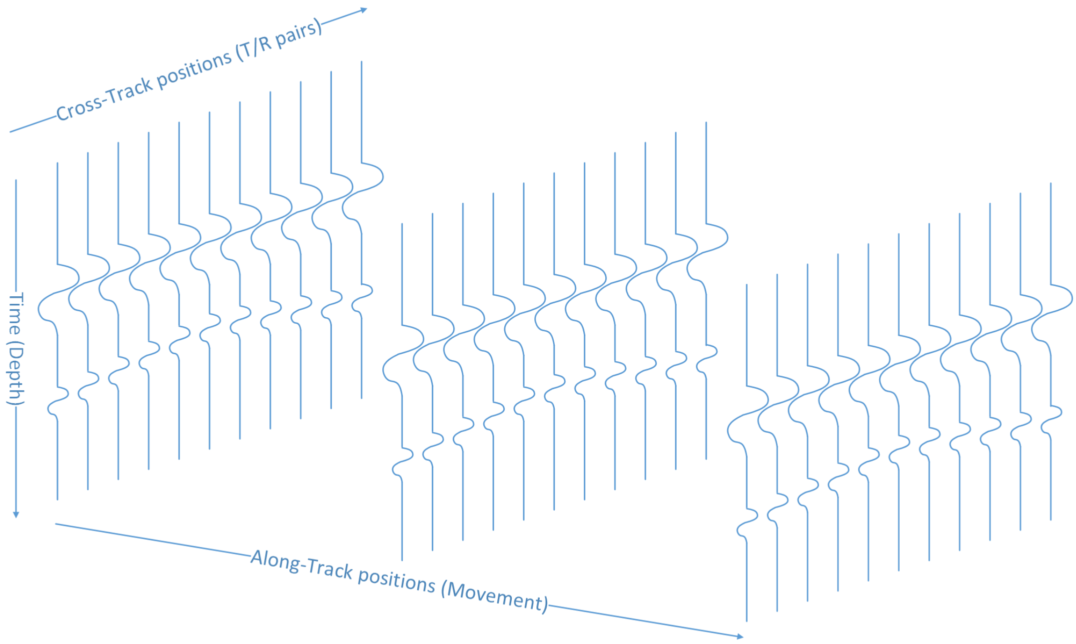

Figure 2.10: Description of GPR C-scan

As the number data sampling positions increase, the information obtained from the data increases. For instance, it's very hard to distinguish a target from clutter only using an A-scan since any clutter-like objects may result in same response easily. B-scan is the most studied GPR output in the literature since it's easy to generate and process; and also offers quite valuable information about the target. Most GPR signal processing algorithms can successfully process B-scan images and detect targets. C-scan outputs, however, need more computational power since the number of A-scans to be processed is increased by the multiple of the number of along-track positions. Nevertheless, the C-scan offers even more information about the environment, therefore offers more capabilities for detection of complex targets.

A sample C-scan simulation output is presented in Figure 2.11 and 2.12. In Figure 2.11, the raw data is presented; which is mainly dominated by the ground bounce signal. In Figure 2.12, the ground bounce signal and mutual coupling signals are removed. Note that, after the removal, the target reflections become much more visible.

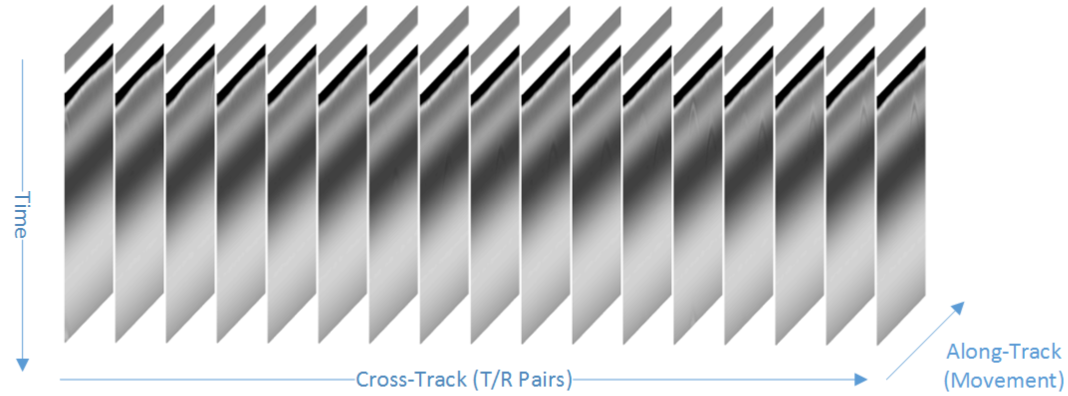

Figure 2.11: Raw C-scan data. Since ground bounce and mutual coupling dominate the signal, the target reflections are not visible at all.

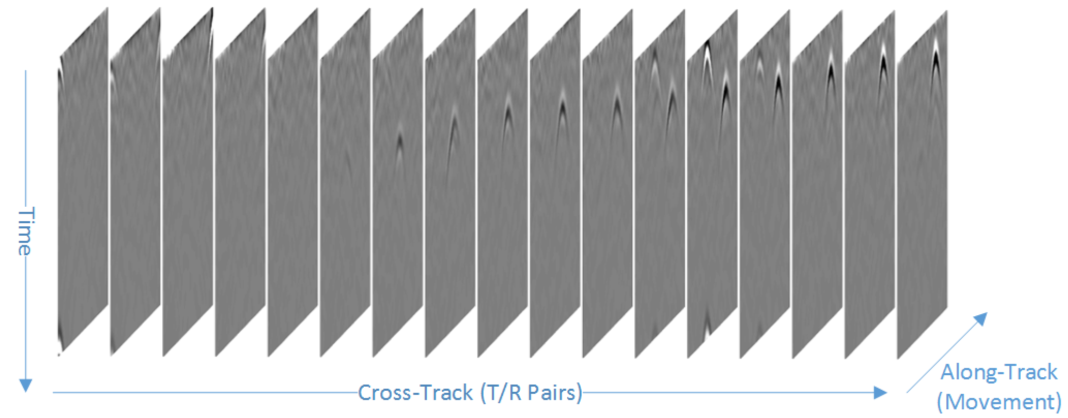

Figure 2.12: C-scan data, after ground bounce and mutual coupling removal. The target reflections became visible after ground bounce and mutual coupling removal.

CHAPTER 3

SIMULATION ENVIRONMENT

In this thesis, wire detection and classification problem is studied on the simulated data generated on gprMax software [22], which is an open source FDTD simulator specifically developed for ground penetrating radar applications. Currently, there are more than 150 studies published in well-respected journals [23] in the literature citing the Reference [22] and [24]. These two references explains the newest capabilities of the gprMax software, which are also applied in this thesis.

The gprMax software allows users to define materials with different electromagnetic properties with different geometries, define sources and receivers at desired locations with different waveforms and polarizations. The medium is divided into a number of FDTD cells (also known as Yee cells [25], named after Kane S. Yee) and the simulation is performed for each receiver and transmitter positions for a given time window, fully implemented in time domain.

The simulation software also allows stepping the source and receivers spatially in order to create B-scans. The capabilities of the simulation software also covers some advanced soil modelling, including inhomogeneous soils with different water densities and roughness [24]. The inhomogeneous soil model is based on the real measurements of the dielectric properties of various soil types conducted in [26].

The gprMax software also allows parallel computing. In order to create a C-scan, simply the B-scans are repeated for several cross-track positions in parallel using an High Power Computing (HPC) system supplied by Aselsan. The HPC system in Aselsan consists of 640 cores of state-of-art CPUs (central processing unit) and terabytes of RAM (random access memory) and it expands annually.

The default simulation environment is described in Table 3.1. In each simulation, only a single parameter of the environment is changed in order to observe the effect of the specific change in the parameter. The geometric view of the default simulation environment is presented in Figure 3.1. There is a single T/R pair and it only moves in along-track (Y) dimension. The input file of gprMax software for the default simulation environment described in Table 3.1 is presented in Appendix B1.

Table3.1: Default Simulation Parameters

Name	Value	Unit	Explanation
x	300	mm	Size of the simulation along x
y	500	mm	Size of the simulation along y
z	150	mm	Size of the simulation along z
Δx	1	mm	Size of discreet Yee cells along x
Δy	1	mm	Size of discreet Yee cells along y
Δz	1	mm	Size of discreet Yee cells along z
t	7.5	ns	Size of time window
Δt	1.924	ps	Sampling interval in time axis
ϵ_r	6	-	Relative permittivity of the soil
σ	10^{-5}	S/m	Conductivity of the soil
μ_r	4	-	Relative permeability of the soil
σ_*	10^{-2}	Ohms/m	Magnetic loss of the soil
f_c	2.5	GHz	Center frequency of the waveform
h_s	100	mm	Height of the soil on z direction
h_a	50	mm	Height of the air on z direction
h_w	50	mm	Depth of wire buried inside soil
r	2	mm	Radius of the wire
Pol_{TX}	x	-	Polarization of transmitting antenna
Pol_{RX}	x	-	Polarization of receiving antenna
ϕ	90	Degrees	Angle of the wire in XY plane
$\underline{x}_{TX}$	(130, 100, 120)	mm	Initial position of transmitter (x,y,z)
$\underline{x}_{RX}$	(170, 100, 120)	mm	Initial position of receiver (x,y,z)
$\Delta\underline{x}_{TX}$	(0, 10, 0)	mm	Spatial sampling step of TX
$\Delta\underline{x}_{RX}$	(0, 10, 0)	mm	Spatial sampling step of RX
K	31	-	Number of spatial sampling points

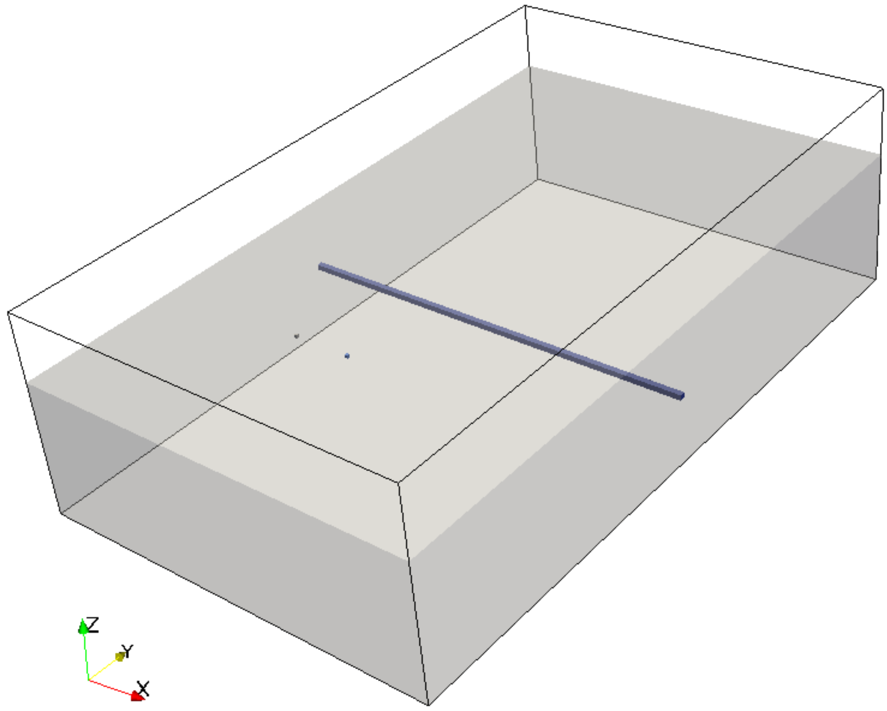

Figure 3.1: Geometrical view of default simulation environment

3.1 Analysis on Simulation Parameters

The simulation parameters in Table 3.1 are kept constant except the parameters examined in the analysis section unless stated otherwise. In this section, frequency of signal, depth, angle, isolation and radius of wire, TX/RX separation and polarization of antennas, electromagnetic properties, inhomogeneity and roughness of soil, looping wire, presence of other wires and rocks are investigated.

The effects of these specific changes in the simulation parameters are observed. In all figures of this chapter, the simulation outputs are time clipped to eliminate ground bounce and mutual coupling signals in order to enhance the contrast in the images. The B-scan images are presented with gray scale color mapping. The contrast in all images are adjusted to the same value. The color mapping is described in Figure 3.2.

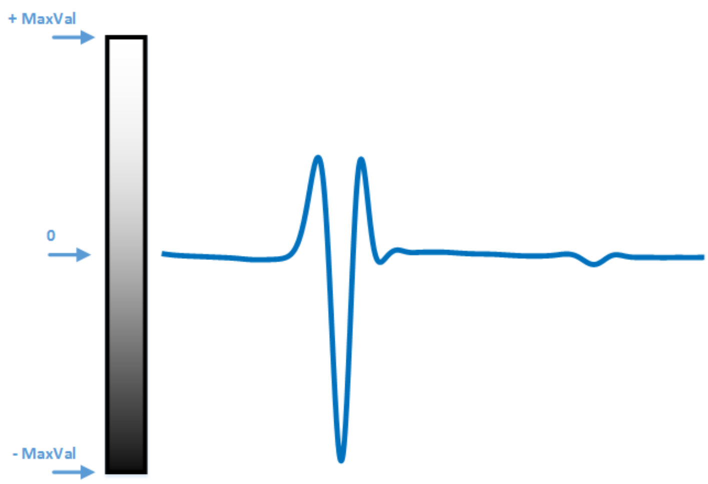

Figure 3.2: Colour mapping used for B-scan visualization. The data after ground bounce clipping is presented in gray scale, mapped between "+ Maximum Value" and "- Maximum Value".

In all simulations, "Gaussian Derivative" waveform is used always. Gaussian derivative signal can be expressed as Equation 3.1, where t is the time in seconds, f_c is the center frequency in Hertz. The time domain and frequency domain Gaussian Derivative signals at center frequency, f_c of 2.5 GHz are presented in Figure 3.3 and 3.4 respectively.

$$w(t) = -4\pi^2 f_c^2 \left(t - \frac{1}{f_c}\right) e^{-2\pi^2 f_c^2 \left(t - \frac{1}{f_c}\right)^2} \tag{3.1}$$

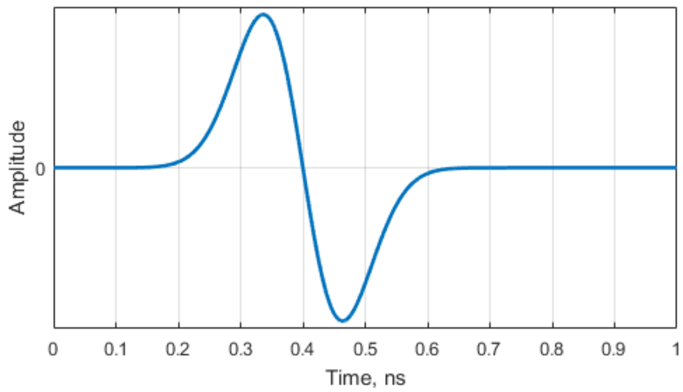

Figure 3.3: Time domain Gaussian Derivative waveform for the center frequency of 2.5GHz

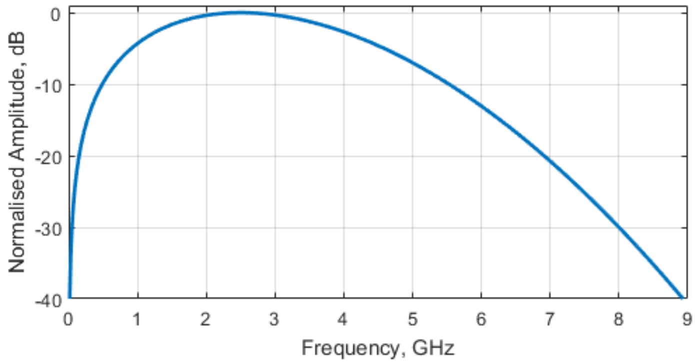

Figure 3.4: Frequency domain Gaussian Derivative waveform for the center frequency of 2.5GHz

3.1.1 Frequency of GPR Signal

In the default simulation parameters listed in Table 3.1, the center frequency was selected as 2.5 GHz. In order to observe the effects of center frequency of the signal, center frequency has changed for 1, 1.5, 2, 2.5, 3 and 4 GHz. The GPR B-scans after ground bounce and mutual coupling removal are presented in Figure 3.5, 3.6 and 3.7

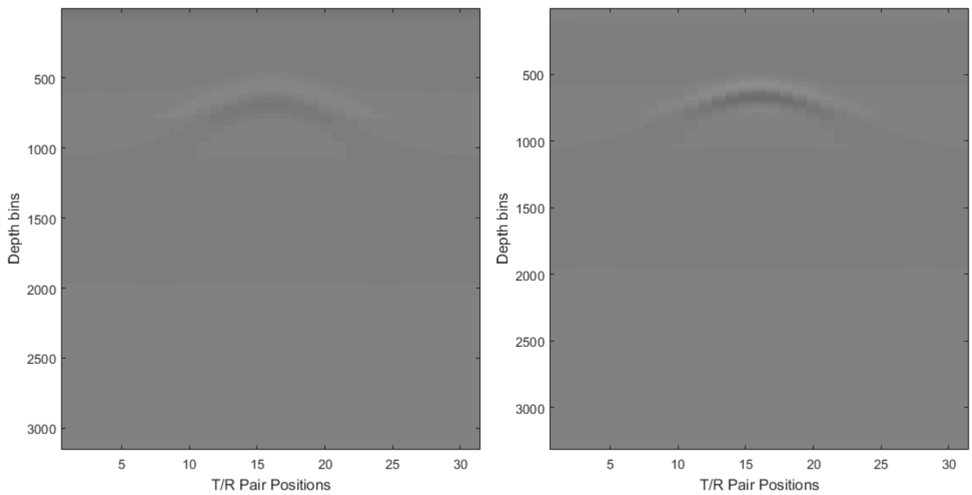

Figure 3.5: B-scans for Gaussian Derivative waveform with center frequency of 1 GHz (left) and 1.5 GHz (right)

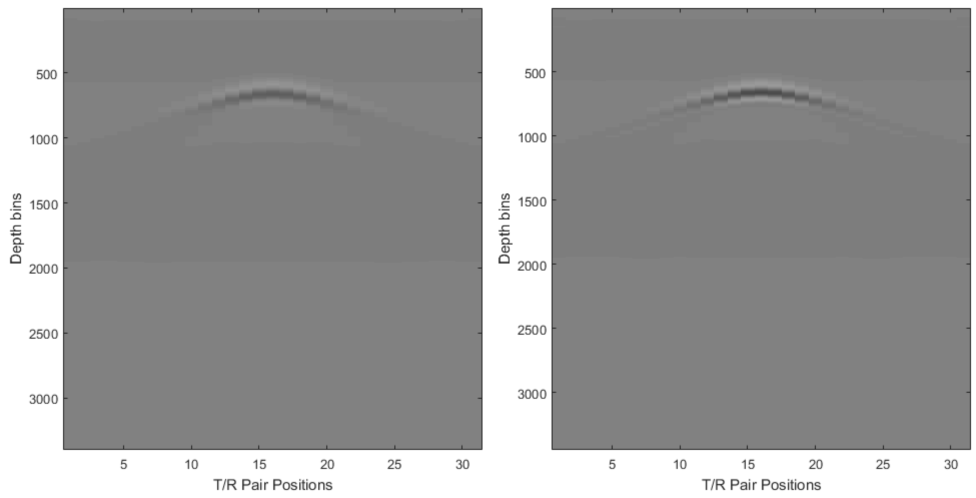

Figure 3.6: B-scans for Gaussian Derivative waveform with center frequency of 2 GHz (left) and 2.5 GHz (right)

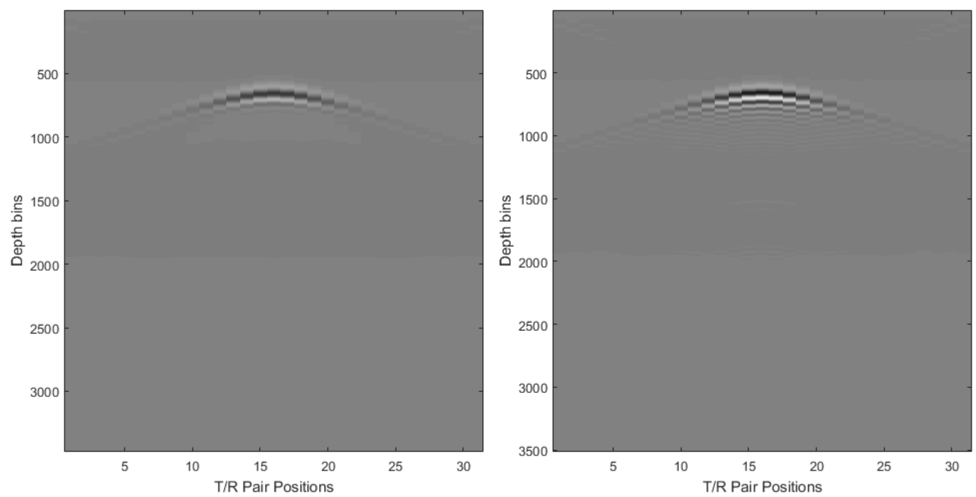

Figure 3.7: B-scans for Gaussian Derivative waveform with center frequency of 3 GHz (left) and 4 GHz (right)

Frequency plays key role in all kinds of radar systems. The radar cross section is directly related with the frequency of the radar system [27] [21]. Radius of the wire in the simulations is 2 mm by default, as given in Table 3.1. The wavelength, λ, of an electromagnetic wave at the center frequency, f_c, propagating underground can be obtained with $\lambda = \frac{c_{soil}}{f_c}$ relation where c_{soil} is the speed of light in the soil medium that can be expressed as $c_{soil} = \frac{c_0}{\sqrt{\epsilon_r \mu_r}}$, where c_0 is the speed of light in vacuum, ϵ_r is the relative permittivity of the soil medium and μ_r is the relative permeability of the soil medium. In [26], the relative permittivity of the soil medium, ϵ_r, for different soil types with changing moisture contents are measured for several frequencies in 0.3 - 1.3 GHz range. Dependent of the soil moisture, ϵ_r can be as low as 4.5 and it increases as the moisture content increases. It has been observed that, wavelength of the GPR signal, λ is quite large compared to the radius of the wire. Therefore, as stated in [27], the amplitude of the signal return is most likely to increase as the frequency increases. In the Figure 3.5 and 3.6, the strength of the signal return increases as the frequency increases as expected. Moreover, resolution of the received signal gets better as the bandwidth of the signal increases [27], [21]. In Figure 3.5 and 3.6, it's observed that the resolution gets better as the frequency, therefore bandwidth, of the signal increases.

However, changing frequency has several drawbacks. The first drawback is that higher frequencies get attenuated faster than the lower frequencies as they propagates in lossy medium. Therefore, deeper targets may become undetectable if the frequency is increased too far. The second drawback is about the hardware design. Most GPR systems are designed as ultra wide band (UWB) in order to increase the resolution of the GPR data, since resolution of a radar system is directly related with the bandwidth of the signal [27], [21]. Increasing the center frequency of Gaussian Derivative signal will result in a need for higher bandwidth; which may be infeasible after some bandwidth / center frequency ratio for hardware design in reality. The last drawback is that increasing frequency in FDTD simulations will require smaller Yee cell sizes [25]; which will drastically increase the simulation time. Also, using a large Yee cell with a relatively high frequency will result in mismatches in FDTD simulation and the results will be incorrect.

The frequency analysis has shown that 2.5 GHz center frequency is sufficient and feasible in reality [28]. The rest of the simulations are performed using 2.5 GHz center frequency.

3.1.2 Electromagnetic Properties of the Soil

In Table 3.1, relative permittivity of the soil, ϵ_r, is given 6 and relative permeability of the soil, μ_r, is given 4 as default. These properties play significant role in the propagation of the electromagnetic waves. ϵ_r is changed to 4 and 8 while μ_r stays as default value, 4, in order to observe the effects due to the change in ϵ_r. Similarly, μ_r is changed to 2 and 6 while ϵ_r stay as default value, 6. GPR B-scans after ground bounce and mutual coupling removal are shown in Figure 3.8 and 3.9.

The speed of the electromagnetic wave changes with $c_{soil} = \frac{c_0}{\sqrt{\epsilon_r \mu_r}}$ relation, where c_0 is the speed of light in vacuum, ϵ_r is the relative permittivity of the soil medium and μ_r is the relative permeability of the soil medium. As expected, the location of the target signal return along time axis changes according to the $\epsilon_r \mu_r$ product. Moreover, the amplitude of the target reflection signal gets smaller for higher $\epsilon_r \mu_r$ product. The soil moisture plays significant role on ϵ_r as stated in [26]. The default simulation parameters in Table 3.1 are valid choices for soils with volumetric moisture content of 5% [26]. Therefore, ϵ_r is selected as 6 and μ_r as 4 for default values for the rest of the simulations.

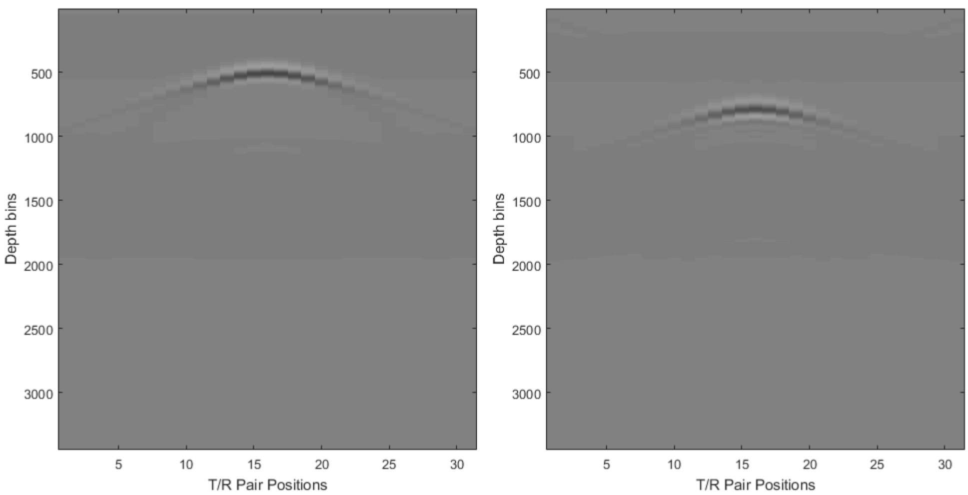

Figure 3.8: B-scans in the soil with μ_r of 4 and ϵ_r of 4 (left) and ϵ_r of 8 (right)

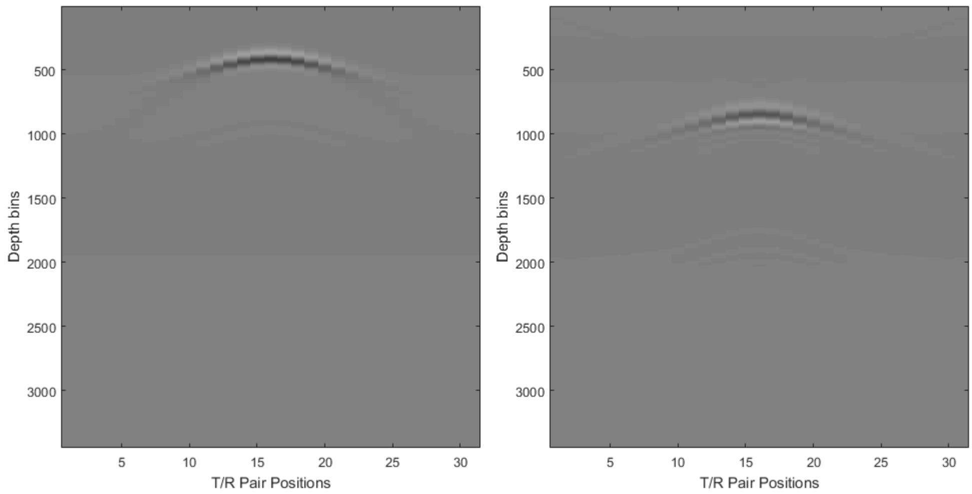

Figure 3.9: B-scans in the soil with ϵ_r of 6 and μ_r: 2 (left) and μ_r of 6 (right)

3.1.3 Depth of Wire

The depth of wire was 5 cm by default given in Table 3.1. It is changed to 3, 4, 6 and 7 in order to observe the effects of depth of wire on the output signal. The results of ground bounce clipped GPR B-scans are shown in Figure 3.10 and 3.11.

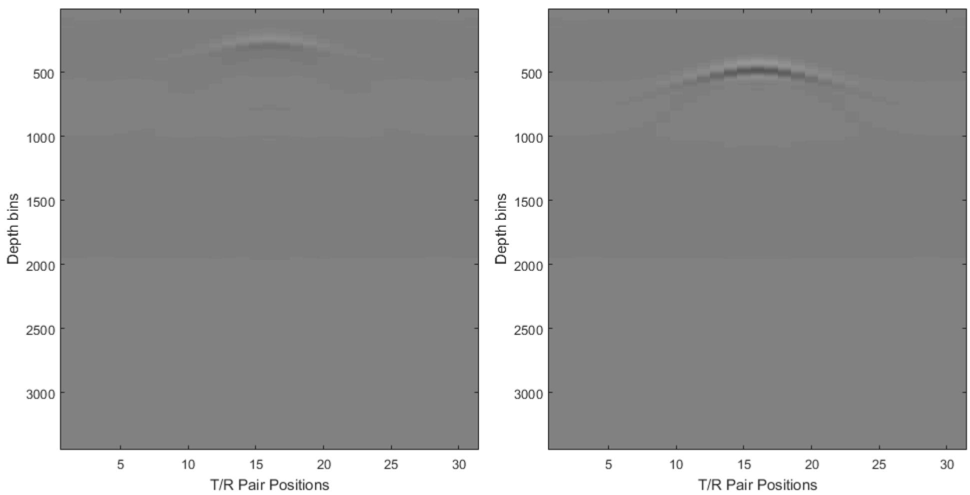

Figure 3.10: B-scans for wire depth of 1 cm (left) and 3 cm (right)

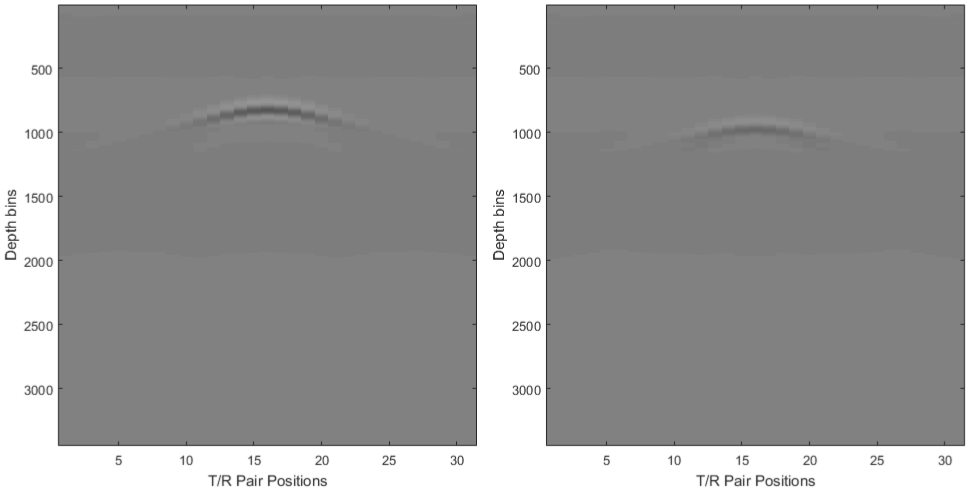

Figure 3.11: B-scans for wire depth of 7 cm (left) and 9 cm (right)

As the depth of wire increases, the time index that the target reflection is observed gets delayed. The amplitude of the target reflection signal is expected to decrease as the depth of wire increases since the electromagnetic waves would propagate in lossy medium longer. However, Figure 3.12 shows the contrary, where the A-scans at the positions where T/R pair is most close to the wire are plotted for different depth values. It was seen that the amplitude of the target reflection is not just related with depth for shallowly buried wires; other environment parameters also play a significant role in this.

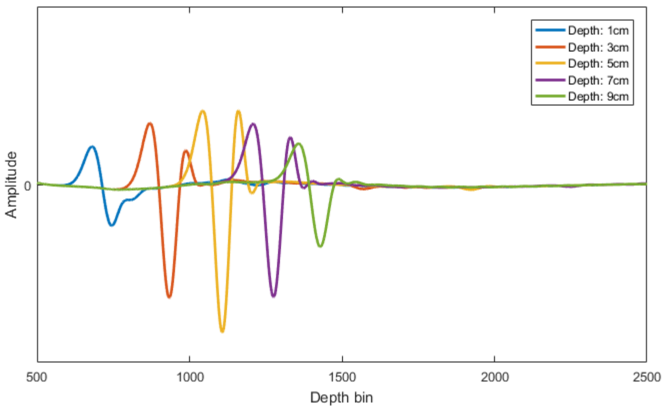

Figure 3.12: A-scans at the closest T/R pair position to the wire for changing wire depths

3.1.4 Radius of the Wire

In Table 3.1, the radius of the wire is given as 2 mm; which is a suitable value for real applications as investigated in [13]. Although in reality, command wire diameters may decrease up to 1 mm [16], [14]. The radius is changed as 3, 5 and 6 mm and the outputs of the simulations are presented in Figure 3.13 and 3.14.

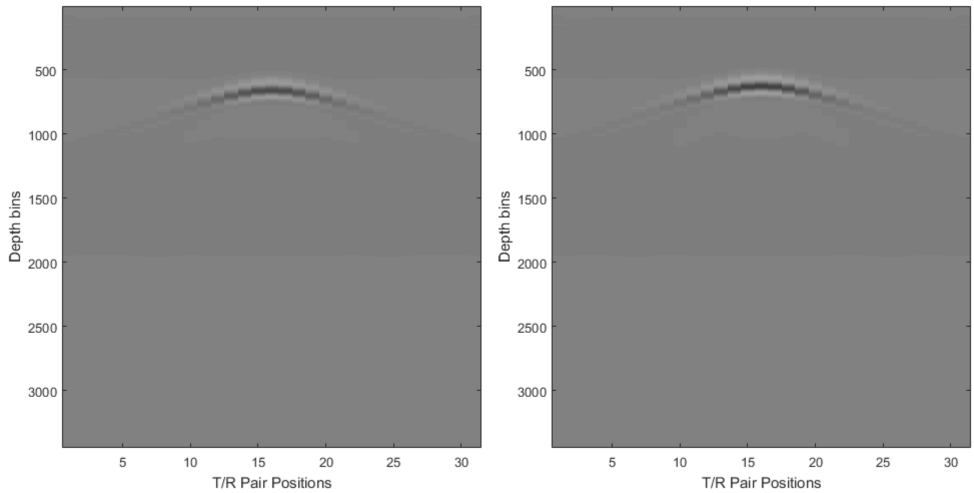

Figure 3.13: GPR B-scan for wire radii of 2 mm (left) and 3 mm (right)

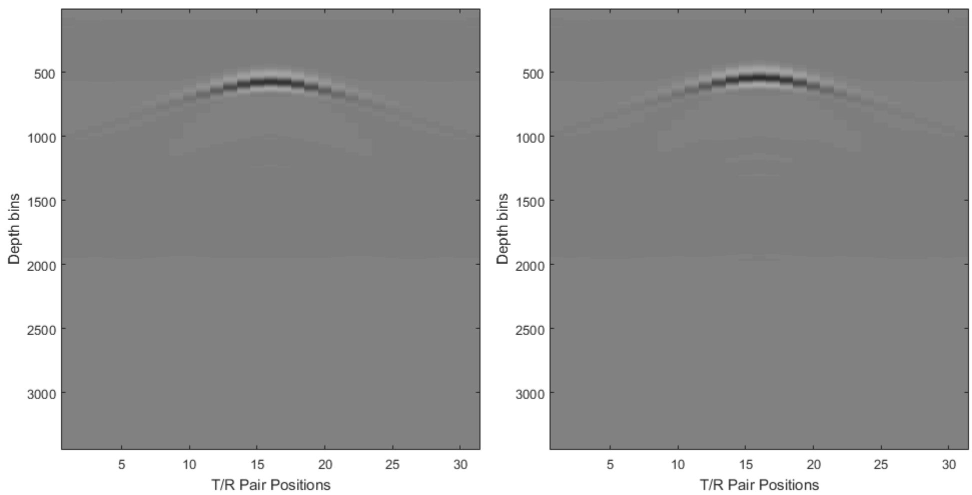

Figure 3.14: GPR B-scan for wire radii of 5 mm (left) and 6 mm (right)

The radius of the wire is expected to directly be related with the amplitude of the return signal; since it plays key role in the radar cross section of the wire.

As expected, the signal return gets smaller for smaller radii; yet the wire is easily distinguishable at the default value, that is 2 mm of radius. Note that, Yee cells ([25] which was explained in the beginning of the chapter) of FDTD simulations are 1 mm in each directions as given in Table 3.1.

Therefore, in order to correctly model the wires in 3-D, having radius smaller than 2 mm, Yee cell size should be made smaller. The change in Yee cell sizes dramatically affects the simulation time. Especially in the C-scans, the simulation time is a great concern. Therefore, Yee cell sizes are kept constant for reasonable C-scan simulation times; and hence, wires with smaller radii are not modelled. For a more detailed analysis, A-scans at the positions where T/R pair is closest to the wire are plotted in Figure 3.15.

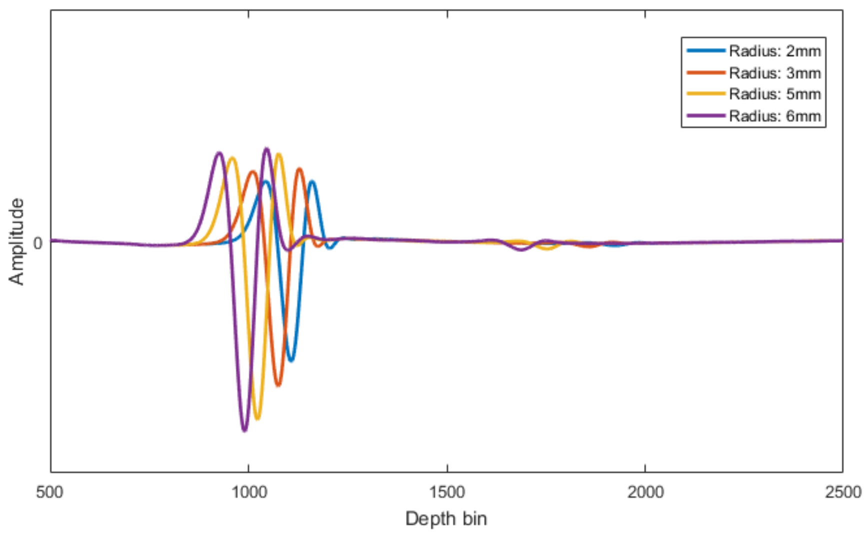

Figure 3.15: A-scans at the closest T/R pair position to the wire for changing wires radii

The amplitude of the target reflection signal gets smaller for smaller radii in Figure 3.15. Moreover, the time index that the peak amplitude is observed also changes as the radius changes. The reason behind is that the depth of the wire is defined as the center of the wire.

Therefore, as the radius of the wire decreases, the upper most border of the wire goes to a deeper location. Moreover, since the command wire is modelled as perfect electric conductor, the ϵ_r is infinity and therefore all of the electromagnetic wave is directly reflected back without any penetration into the wire. Hence, the target reflection that is observed is mainly composed of the electromagnetic waves that are reflected at the upper boundary of the wire in the depth axis.

3.1.5 TX-RX Separation

The transmitting and receiver element separation is another parameter that affects the GPR outputs. If the T/R pair is separated too much, the amplitude of the return signal gets smaller since the electromagnetic waves propagate longer distances. The separation is also an important parameter for hardware design. The distances should be realistic for antenna T/R array design. The default value of T/R element separation in Table 3.1 is 4 cm. TX/RX Separation of 2, 4, 6 and 8 cm are investigated and the ground bounce and mutual coupling removed B-scans are presented in Figure 3.16 and 3.17. The TX/RX separation plays significant role on the return signal amplitude. The amplitudes of the A-scan signals are plotted in Figure 3.18. For the separation of 8 cm, the return signal has been decreased drastically.

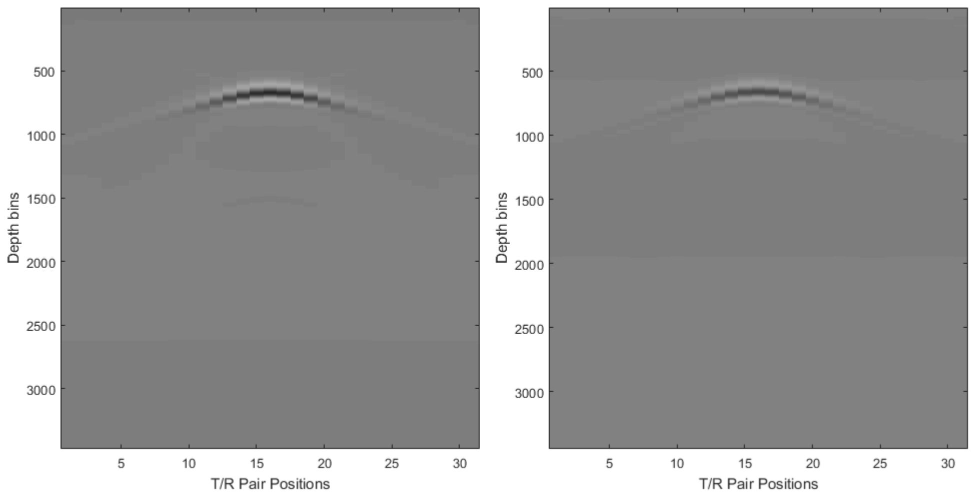

Figure 3.16: GPR B-scan with TX/RX separation of 2 cm (left) and 4 cm (right)

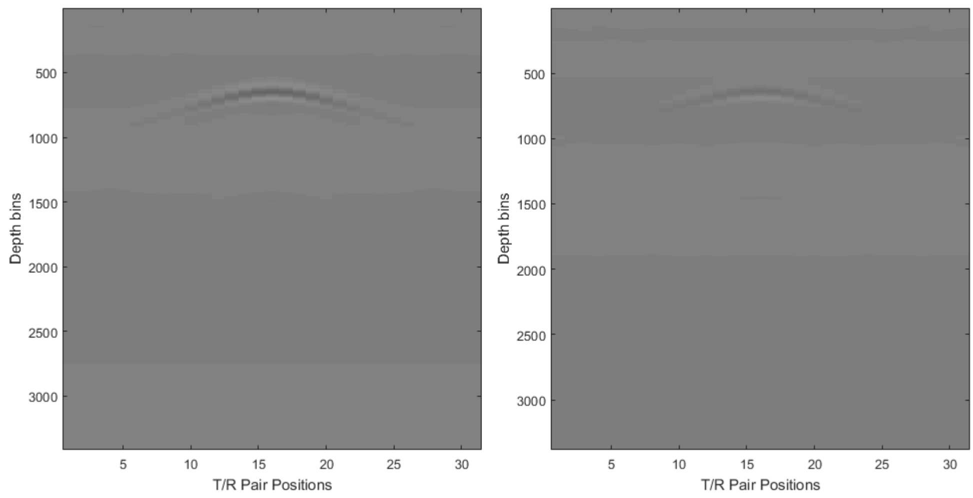

Figure 3.17: GPR B-scan with TX/RX separation of 6 cm (left) and 8 cm (right)

It can be concluded that; shorter TX/RX separation would result in better target returns for shallowly buried targets. Yet, 2 cm of separation is not very feasible for hardware design in reality. However the default value, 4 cm, is more feasible for antenna design. Therefore for the rest of the simulations, the TX/RX separation value is kept constant as 4 cm, as given in Table 3.1.

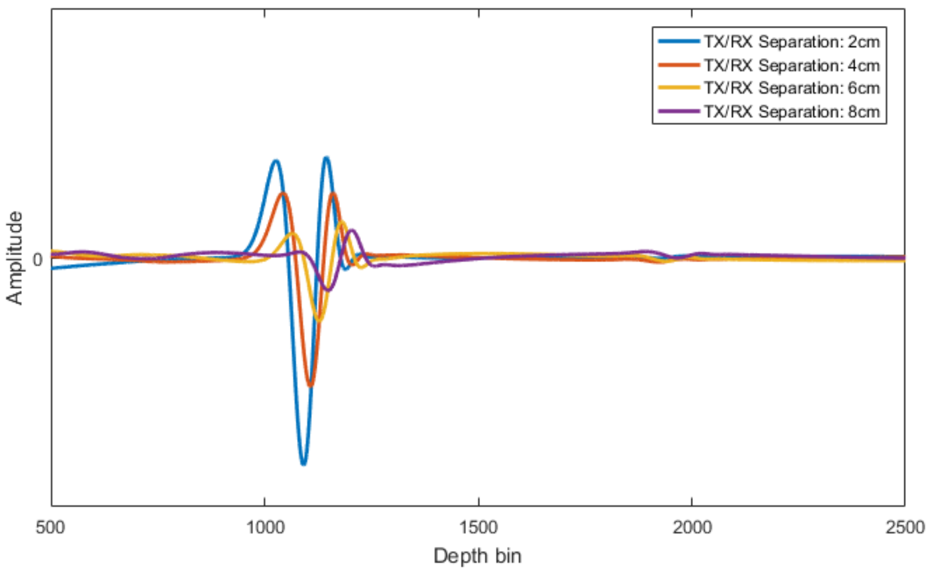

Figure 3.18: A-scans at the closest T/R pair position to the wire for changing TX/RX separations

3.1.6 Presence of Isolation Material on the Wire

In the environment defined in Table 3.1, the wire is modelled as a perfect electric conductor without coating. Yet, in reality, there can be an isolation material on the wire; which may affect the GPR signal. An isolation layer, having electromagnetic properties of $\epsilon_r = 2$ and $\mu_r = 1$, with thickness of 5 and 10 mm is modelled and analyzed. The results of ground bounce and mutual coupling removed GPR B-scans for isolated wires are shown in Figure 3.19.

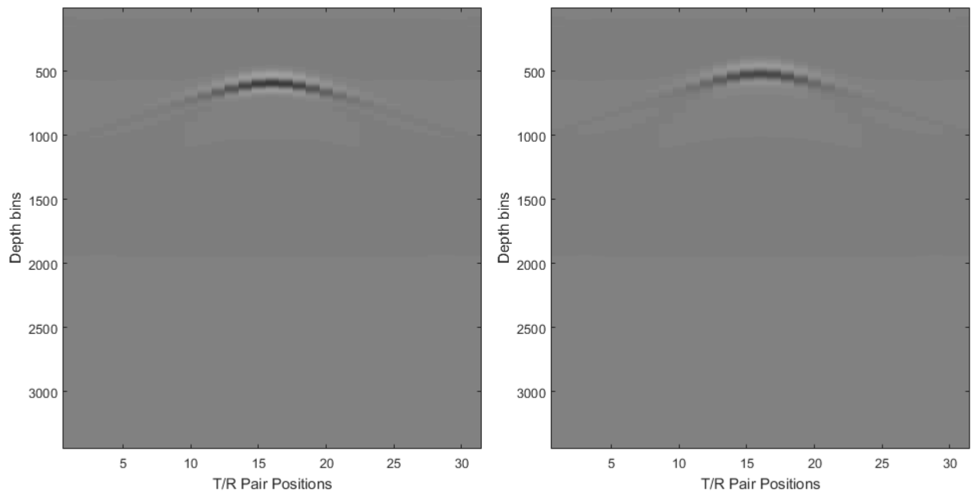

Figure 3.19: GPR B-scan of wires with isolation layer of 5 mm thickness (left) and 10 mm thickness (right)

The A-scans at the closest point of T/R positions to the wire is plotted in Figure 3.20. The isolation is modelled as a plastic with a small ϵ_r and unity μ_r. The only significant observation was that the target reflections for isolated wires occur at earlier time indices.

The reason behind is that electromagnetic wave propagates faster in the isolation medium having smaller ϵ_r and μ_r values than soil. Since isolation does not affect simulation much, rest of the simulations were generated without isolation.

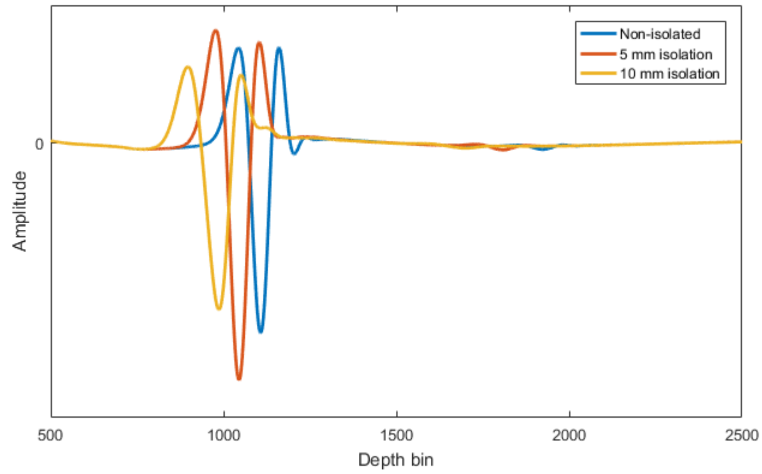

Figure 3.20: GPR A-scan of wires with isolation layer of 5 and 10 mm thickness

3.1.7 Angle of the Wire

In the simulation environment defined in Table 3.1, the wire is placed perpendicular to the along-track direction in XY plane, making the angle of 90^o with the movement direction. In reality, wire may go in any directions. Therefore an analysis on the wire positioning is conducted to observe the possible effects. Direction of the wire is changed from 75^o to 0^o with steps of 15^o. The positioning of the wire with $\phi = 30^o$ is presented in Figure 3.21.

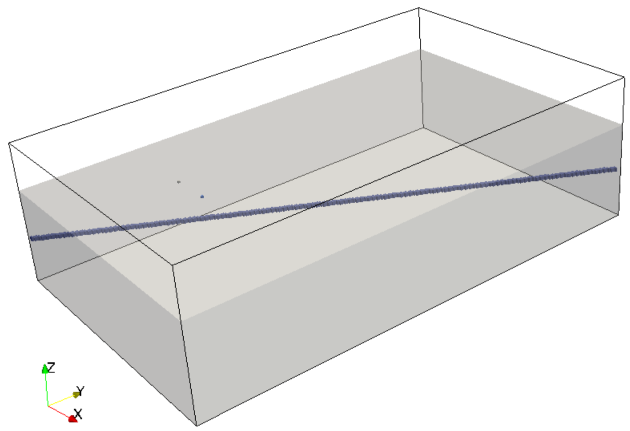

Figure 3.21: Simulation set-up for wire positioned with 30 degrees in XY plane

The GPR data after ground bounce and mutual coupling removal for the wire directions swept from 75^o to 0^o with linear steps of 15^o are shown in Figure 3.22, 3.23 and 3.24. The problem has been also investigated in [19] antenna design for pipe detection problem and in [13] antenna design considering buried wire detection problem. The results were matching with the simulation results presented.

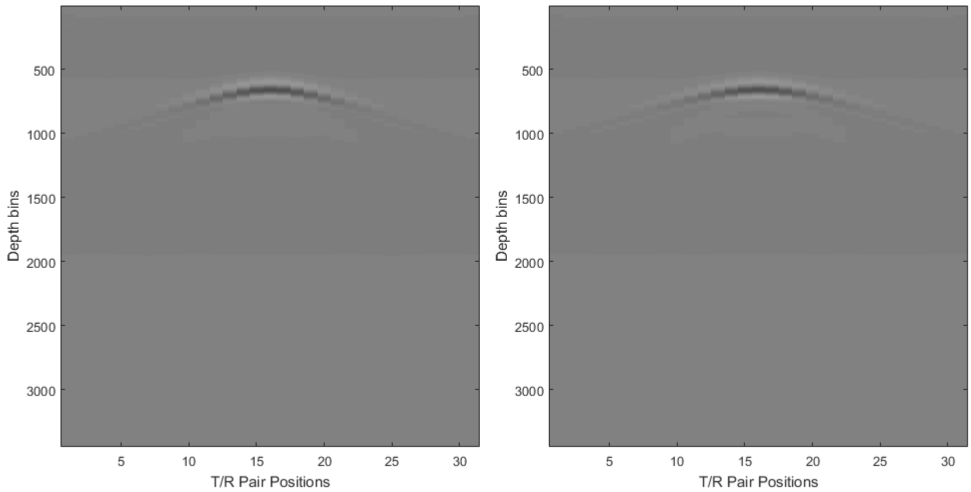

Figure 3.22: B-scans for wires with ϕ angle of 75^o (left) and 60^o (right)

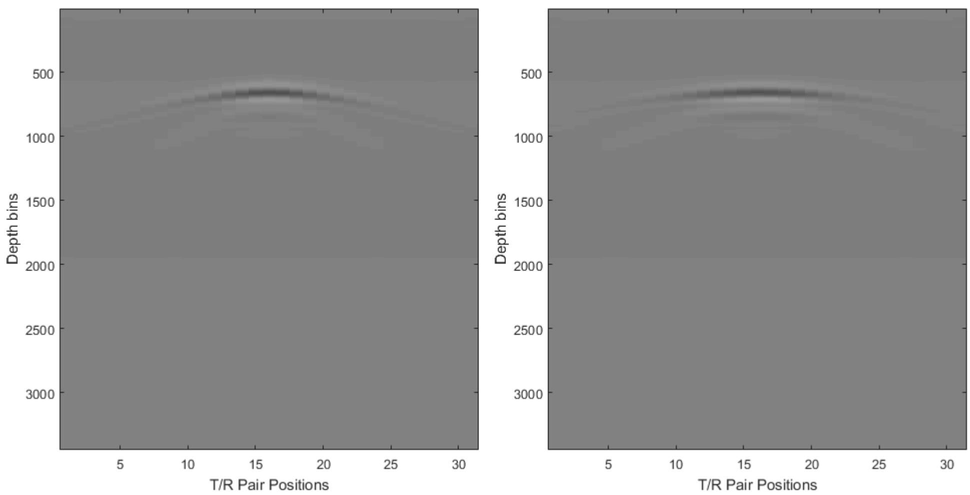

Figure 3.23: B-scans for wires with ϕ angle of 45^o (left) and 30^o (right)

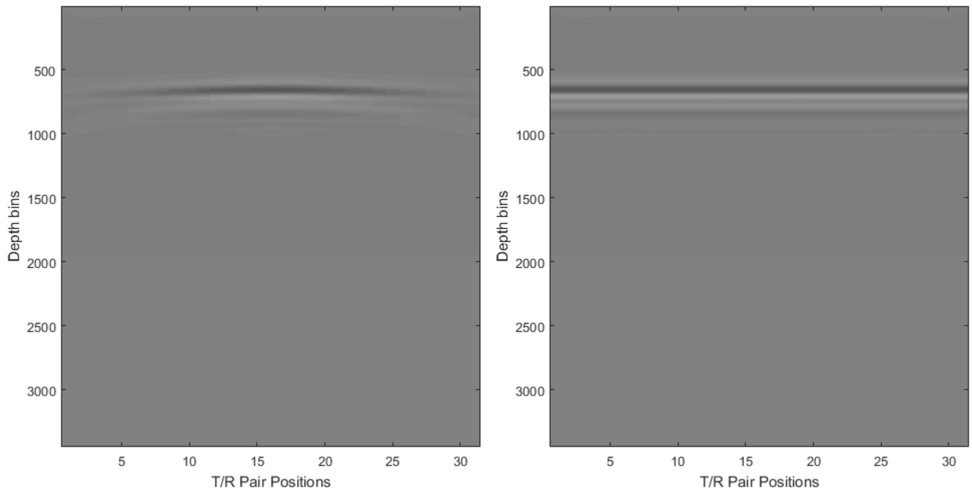

Figure 3.24: B-scans for wires with ϕ angle of 15^o (left) and 0^o (right)

The information that the analyses provided is very powerful; dependent of direction of the wire, the hyperbola pattern may widen. Moreover, when the wire is positioned in the along-track direction, the target response becomes flat in all A-scans; which may be confused as a constant subsurface reflection when looking in a single B-scan. Therefore, regular hyperbola recognition methods like [29] and [30] are not suitable for detecting the wires placed in along the along-track direction. This results leads to the fact that use of C-scan is compulsory for a functional wire detection and classification system. This result has also shaped the algorithms suggested in Chapter 5.

Angle of the wire is also highly related with the polarization of the antenna, which is investigated in the next analysis. Note that, the antenna polarization is in X direction, as given in Table 3.1.

3.1.8 Polarization of the Antenna

The TX and RX antenna polarization are defined as X direction in Table 3.1. X direction corresponds to the cross-track dimension in the simulation environment. The TX and RX antenna polarizations are changed to Y direction; which corresponds to the along-track dimension. The ground bounce and mutual coupling removed B-scans for x and y polarization are presented in Figure 3.25. The A-scans at the location where the T/R pair is closest to the wire are presented in Figure 3.26. The hyperbola signature of the wire is considerably lost in Y polarization configuration. However, surprisingly, in the A-scans at the location where the T/R pair is closest to the wire, the amplitude of Y polarization configuration is greater than the X polarization antenna. On the contrary, the expectations was to have a greater amplitude for the polarization in the same direction with the wire direction. In [14], the command wire scattering problem is analyzed in air medium and found out that when the wire is placed in the same direction with the antenna polarization, the wire scattering amplitude gets improved by 1 dB (which is not a very promising improvement), compared to the perpendicular case. The study, [14], concludes that the use of circular polarization is the best for command wire detection.

However, the simulation result presented in Figure 3.26 is dependent on various parameters, and could not be generalized. The significant observation made in this analysis is only that the hyperbola signature has been narrowed with the polarization that is perpendicular to the wire direction.

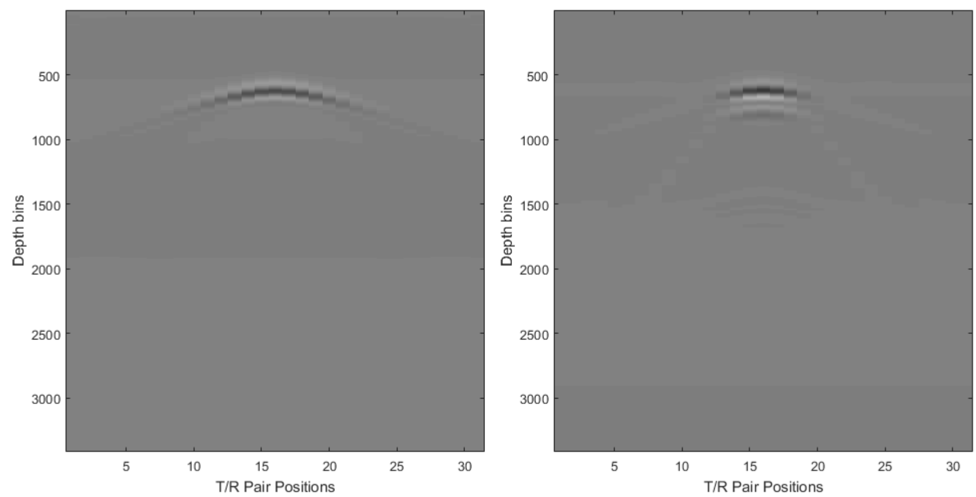

Figure 3.25: B-scans for TX and RX antenna polarizations of X (left) and Y (right)

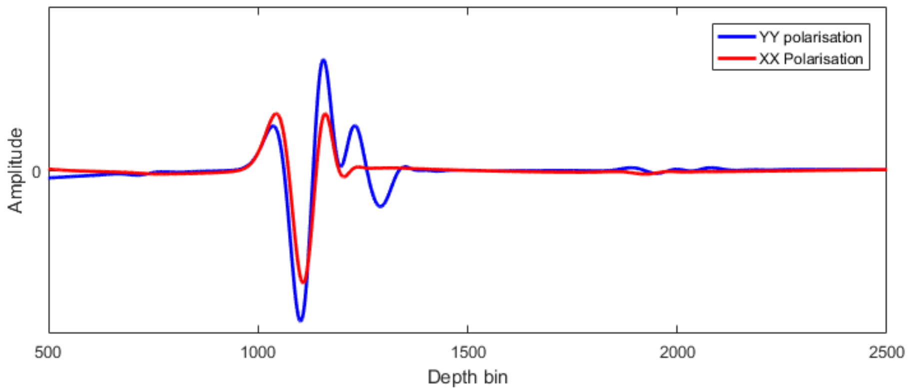

Figure 3.26: A-scan data of X and Y antenna polarizations

3.1.9 Inhomogeneity of Soil

The simulations so far are generated using the soil modelled as a homogeneous medium, whose electromagnetic properties are defined in Table 3.1. However, soil in reality is highly inhomogeneous. The contents of soil varies much; even distinct layers can be formed underground. Also the moisture in the soil varies in reality. Therefore, a set of simulations are generated using the inhomogeneous soil option of gprMax software [24]. gprMax software allows users to define an inhomogeneous soil, with a water fraction range. Then, it generates a number of materials within the defined water fraction range, using the result of real measurements of various soils conducted on [26].

In Figure 3.27 and 3.28, B-scans obtained from a soils with sand fraction of 0.5, clay fraction of 0.5, bulk density of $2g/cm^3$, sand density of $2.66g/cm^3$ and changing volumetric water fraction ranges are presented.

As the water concentration of the soil increases, the resulting ϵ_r value of the soil increases since ϵ_r of water is 81; that is quite large compared to the soil's. As a result, increase in ϵ_r affects the time index that signal is observed. The inhomogeneities, however, played very little role in the hyperbola structure of the received signal.

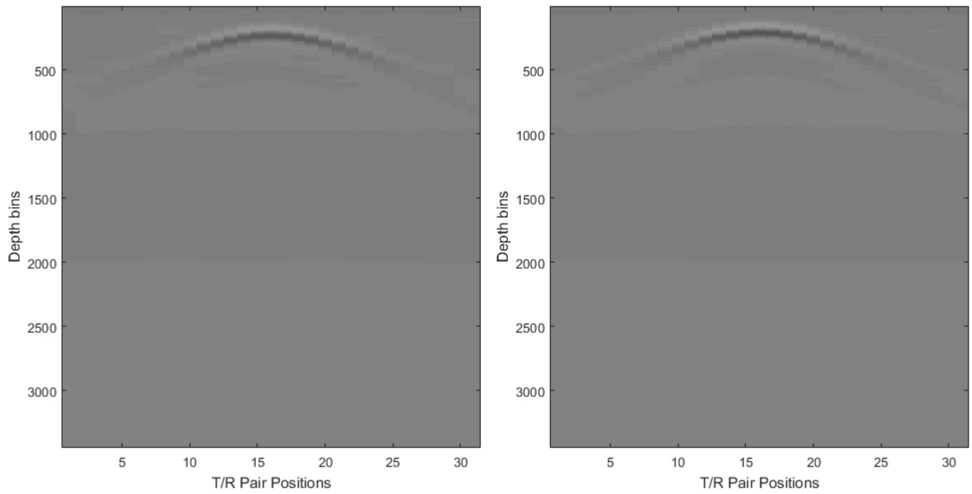

Figure 3.27: B-scan data with inhomogeneous soil, with volumetric water fraction ranging from 0.001 to 0.05 (left) and 0.01 to 0.05 (right)

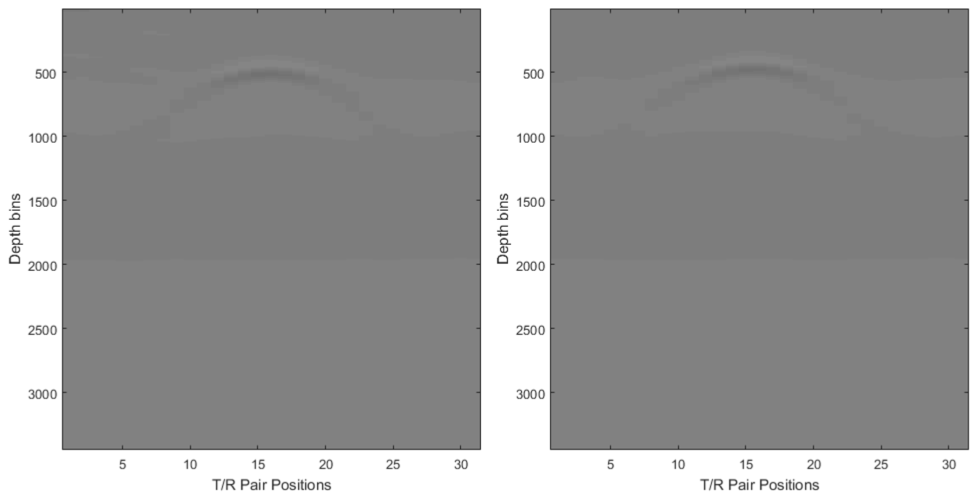

Figure 3.28: B-scan data with inhomogeneous soil, with volumetric water fraction ranging from 0.001 to 0.25 (left) and 0.05 to 0.25 (right)

3.1.10 Surface Roughness

Same as inhomogeneities, the simulations so far are generated with flat ground surface. However, in reality the soil surface would be considerably rough. This will directly affect the ground bounce removal performance of the system. Therefore, some simulations are generated using the roughness option provided in gprMax software [24]. The roughness levels are changed for $\pm 2mm$, $\pm 5mm$, $\pm 10mm$ and $\pm 15mm$ values; as the environment is presented in Figure 3.29 and 3.30.

The B-scan outputs of the soils with changing roughness levels are presented in Figure 3.31 and 3.32. As the roughness increases, the hyperbola signature gets distorted, which can be especially seen in 1.5 cm roughness case; which is a relatively small value for roughness in real scenarios.

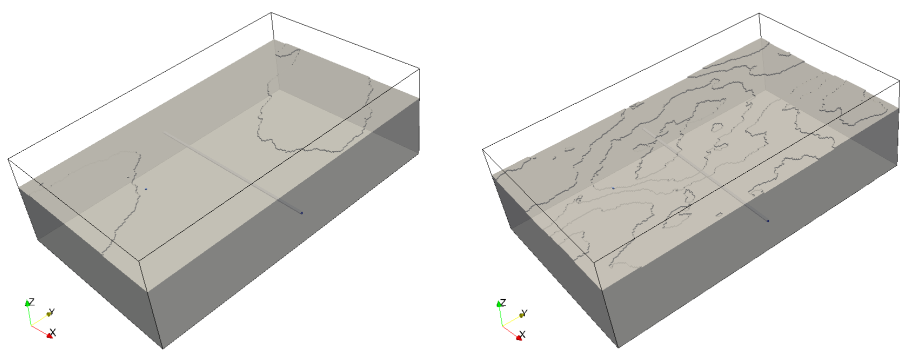

Figure 3.29: The simulation environments with surface roughness of $\pm 2mm$ (left) and $\pm 5mm$ (right)

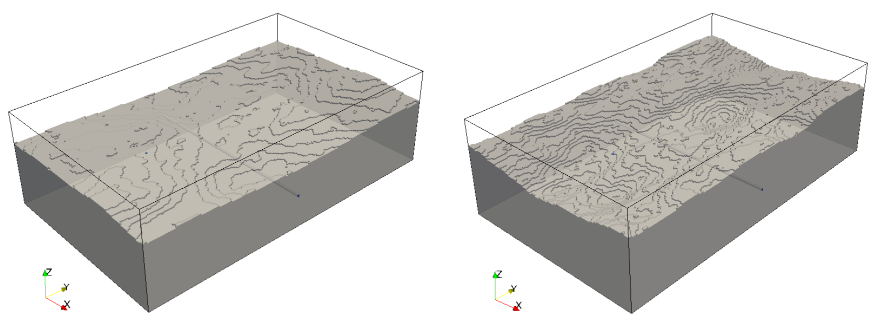

Figure 3.30: The simulation environments with surface roughness of $\pm 10mm$ (left) and $\pm 15mm$ (right)

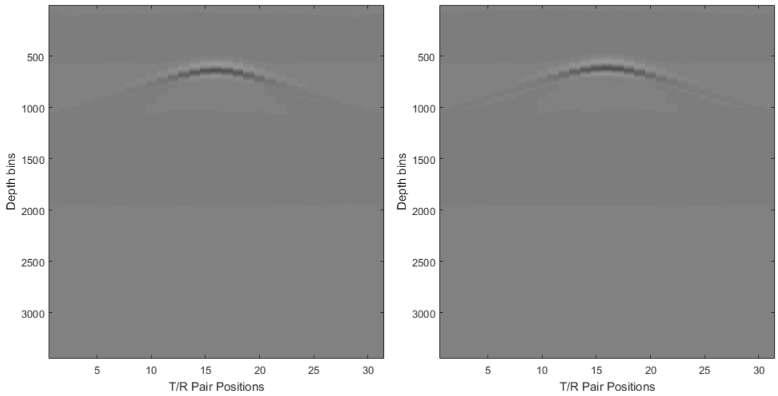

Figure 3.31: B-scan data with roughness of $\pm 2mm$ (left) and $\pm 5mm$ (right)

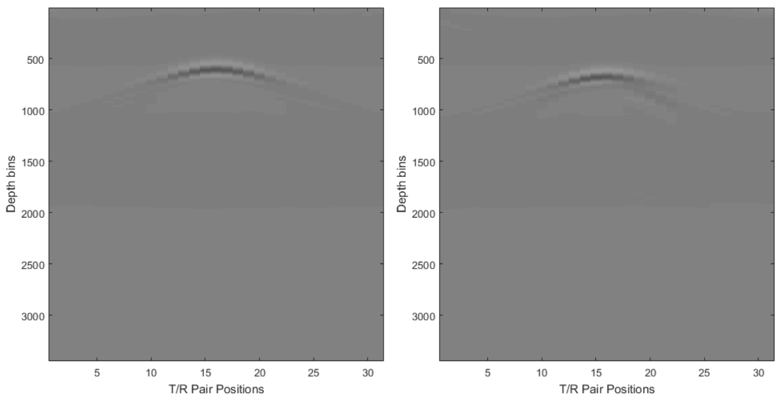

Figure 3.32: B-scan data with roughness of $\pm 10mm$ (left) and $\pm 15mm$ (right)

3.1.11 Presence of Another Wire

The default simulation environment described in Table 3.1 has only a single wire inside the soil. Hence, the presence of another target in the B-scan outputs are investigated. The default simulation environment in Figure 3.1 is widened along Y axis in order to investigate targets with the distance of 40, 30, 20 and 10 cm between. The wires are positioned with $\phi = 90^o$ at the depth of 5 cm. The B-scan outputs are shown in Figure 3.33 and 3.34.

When the distance between two wires are enough large, like in 40 cm separation case, the target reflection can be distinguished very easily. However, as the wires are positioned too close to each other, like in 10 cm separation case, the reflections begin to collide. Moreover, the secondary reflections gets considerably higher when as seen in 10 cm case; which may be confused with another target.

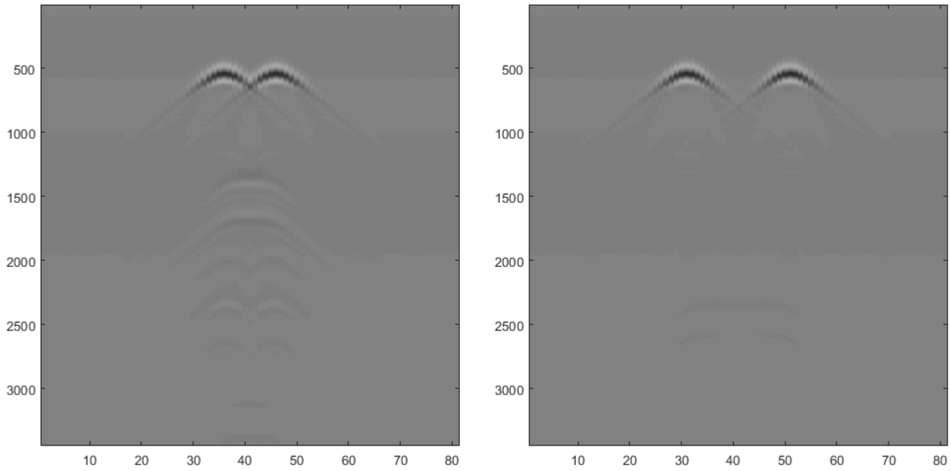

Figure 3.33: B-scan data of two wires with separation of 10 cm (left) and 20 cm (right)

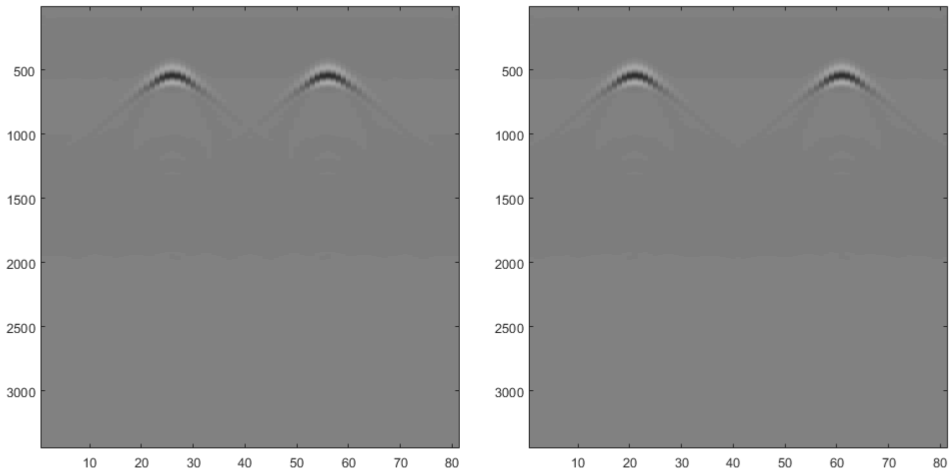

Figure 3.34: B-scan data of two wires with separation of 30 cm (left) and 40 cm (right)

3.1.12 Looping Wire

The wires used as command wire for IED detonation can be two core cables in order to form a closed circuit loop. Therefore, a looping wire case is analyzed. The simulation set-up is presented in Figure 3.35.

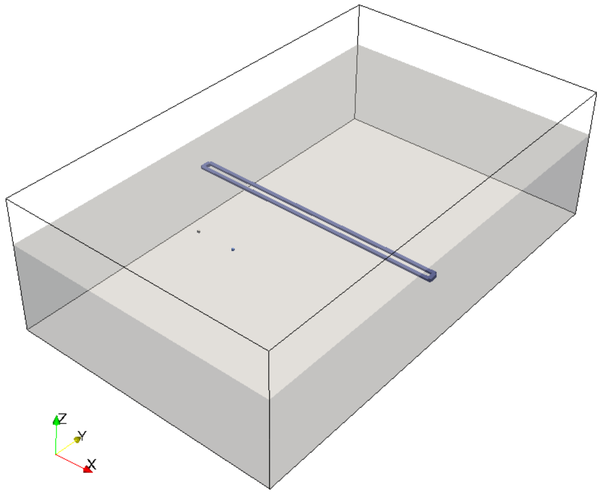

Figure 3.35: Geometrical view of the simulation environment with looping wire

The B-scan outputs after ground bounce and mutual coupling removal, obtained from the simulation environments with looping wire at depth of 3 cm and 7 cm are presented in Figure 3.36. The simulation results highly resembles with single wire case, but the amplitude of the target reflection is improved slightly.

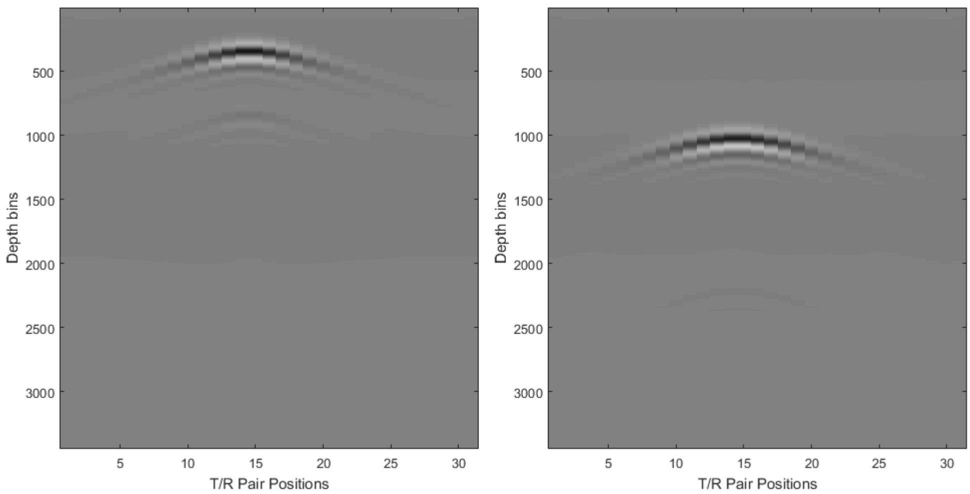

Figure 3.36: B-scan data of looping wires at depth of 3 cm (left) and 7 cm (right)

3.1.13 Presence of Rocks with Different Electrical Properties

Homogeneous soils and inhomogeneous soils with different material concentrations are studied so far in the simulations. However, clutter objects like rocks may cause false alarms in GPR systems.

Therefore, presence of rocks in the soil is investigated. The rocks are modelled as spherical objects with 2 cm radius and electromagnetic properties, scattered around the soil. The simulation environment is presented in Figure 3.37.

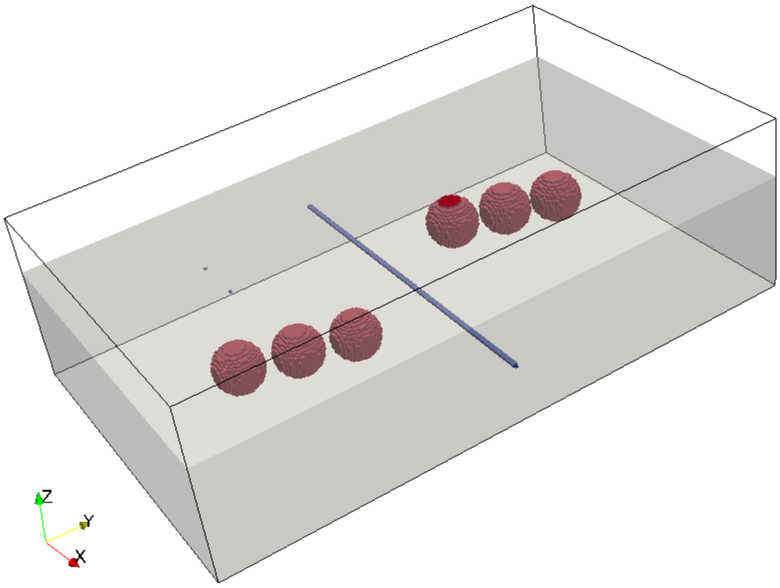

Figure 3.37: Geometrical view of the simulation environment with multiple rocks

The electromagnetic properties of the rocks should be different than the soil in order to create a discontinuity in the electromagnetic profile of the soil. The default soil parameters was $\epsilon_r = 6$ and $\mu_r = 4$ as given in Table 3.1. The electromagnetic properties, (ϵ_r, μ_r) pairs, of rocks are changed to (4,2), (2,4), (4,4), (2,7), (6,7) and the last one is modelled as a perfect electric conductor. The B-scans with the rocks having electromagnetic properties listed, are shown in Figure 3.38, 3.39 and 3.40.

These simulations are also gave valuable information about command wire detection problem. Dependent on the electromagnetic properties of the rocks, the reflections caused by rocks may be observed at the upper boundary of the rock as seen in right side of Figure 3.40, or at the lower boundary of the rock as seen in left side of Figure 3.40. Moreover, the wire reflection cannot be discriminated from the rock reflections; they share the very common reflection characteristics. It leads to the following strong and important conclusion; that command wire detection problem should be studied on C-scan data and B-scan data is insufficient for proper discrimination.

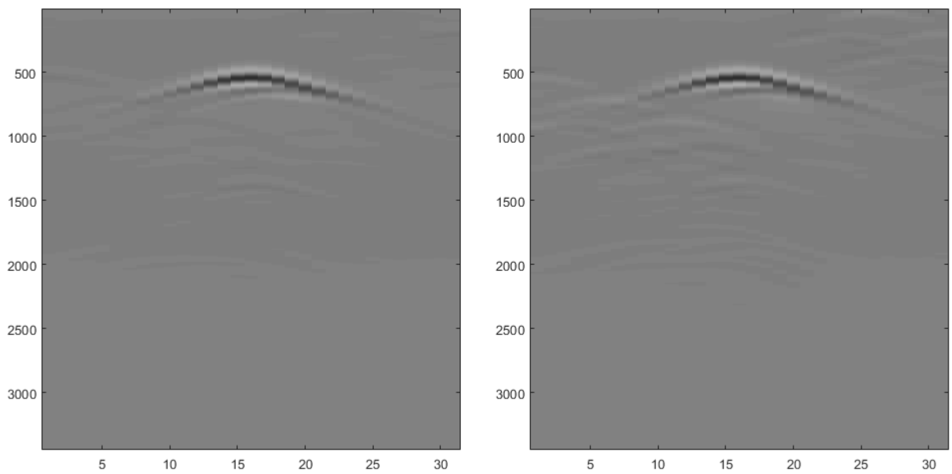

Figure 3.38: B-scan outputs of rocks with (ϵ_r, μ_r) of (4,2) (left) and (2,4) (right)

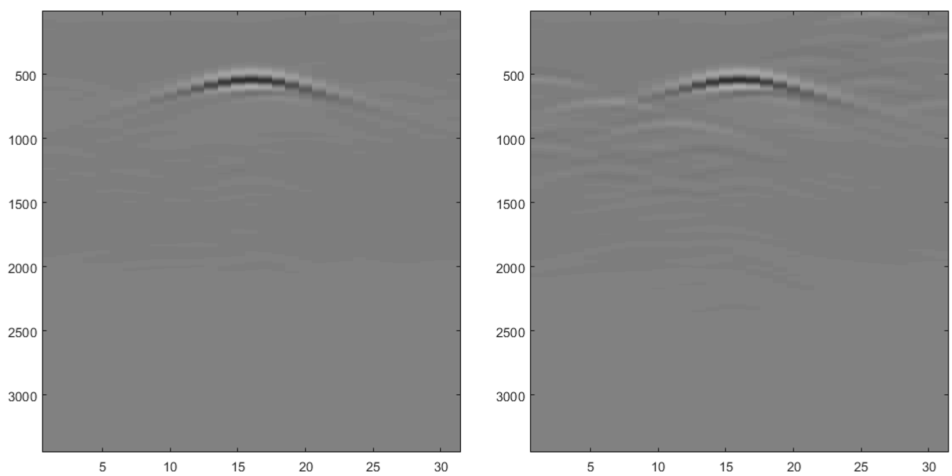

Figure 3.39: B-scan outputs of rocks with (ϵ_r, μ_r) of (4,4) (left) and (2,7) (right)

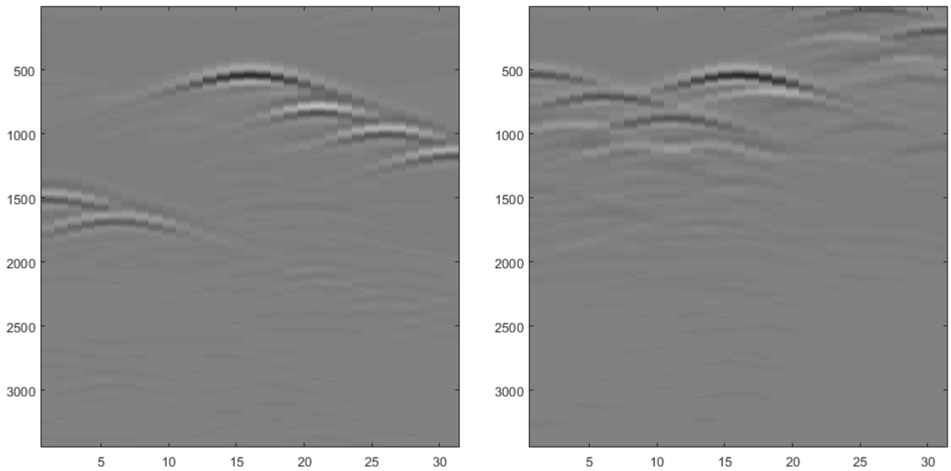

Figure 3.40: B-scan outputs of rocks with (ϵ_r, μ_r) of (6,7) (left) and perfect conductor (right)

3.2 C-scan Simulations

C-scan environment is modelled as 1 x 1 x 0.20 meters in cross-track, along-track and depth dimensions. T/R pairs are placed along X direction, starting from 10 cm and goes to 90 cm with 5 cm steps; which results in 17 T/R pairs in total. The transmit and receive elements in a pair is separated by 2 cm. The antenna array moves along track direction with 1 cm steps, starting from 10 cm and goes to 90 cm; which results in 81 along track positions. The scanning geometry is presented in Figure 3.41. The soil depth is 15 centimetres and T/R pairs are placed 3 centimetres above the surface.

The Yee cell size was selected as 1 mm in the B-scan simulations section. However, with 1mm Yee cell size, FDTD simulation of one A-scan position takes approximately takes 4 hours using 8 CPU cores in parallel with 2 GHz clock in the HPC system. All along track simulations for each T/R pair run in parallel. In total 136 CPU cores (8 CPU cores for each T/R pair) are used in parallel to generate a single C-scan data, which finishes in 2 weeks in real-time.

Since, 2 weeks of simulation time is not feasible for generating enough simula-

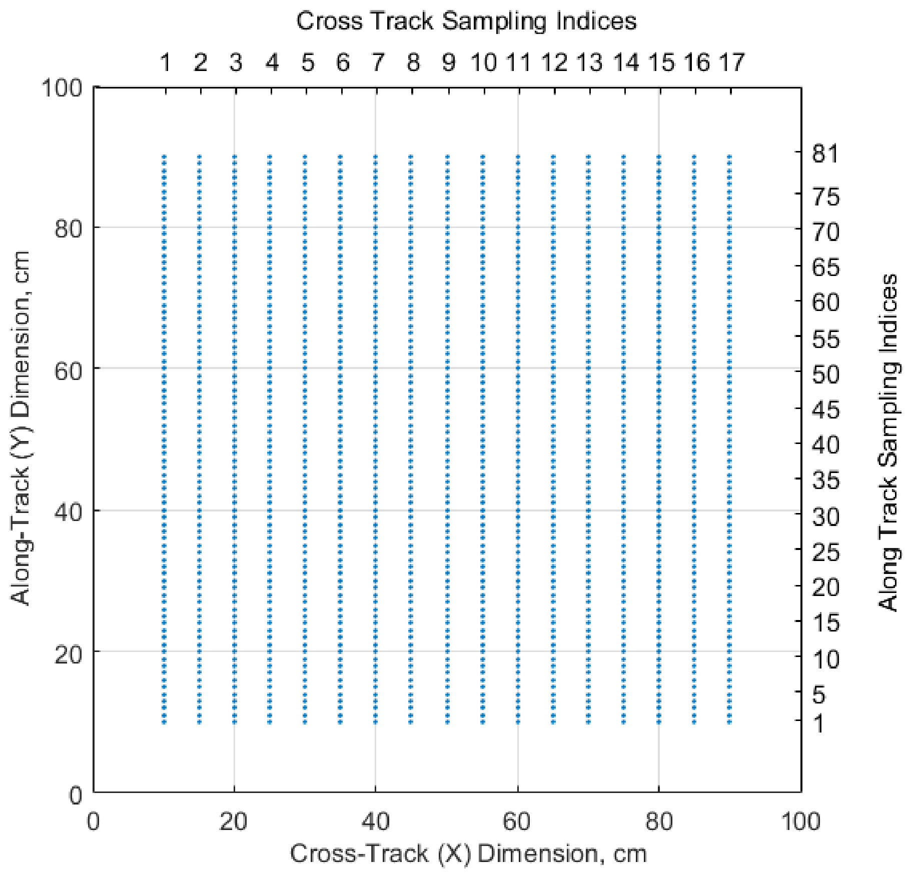

Figure 3.41: Positions of T/R elements in XY (Cross/Along Track) dimension.

tions to test the performance of algorithms, the Yee cell size is increased to 2 mm for C-scan simulations. With this change, the simulation time decreased by 16 which can be roughly obtained with 2^4 relation, where 2 is the scaling amount and 4 is the number of dimensions; x, y, z and t. As a result, a single C-scan simulation takes roughly one day to complete.

Note that, in any FDTD simulation, the wire cross section should be modelled with at least 2 Yee cells in each dimension. When the wire cross section is modelled with a single Yee cell, angles in each dimension leads to discontinuities in the wire model. Therefore, the minimum radius for a wire that can be successfully modelled is 2 mm for C-scan simulations. All of the C-scan simulations are performed with 2 mm of wire radius. There was a trade-off between simulation time and minimum wire radius in the C-scans. It should be noted that, since the wires are electrically very thin, the problem is linearly scalable; such that wires with smaller radii will have the same characteristics, except the amplitude will gets smaller. However, as expected, after some value, the extremely thin wire should be indistinguishable from the clutter environment.

The Gaussian derivative waveform at center frequency of 2.5 GHz is used in C-scan simulations. The TX and RX antenna polarizations are in the X direction; that is the cross-track direction.

In the C-scan simulations, the soil is modelled as inhomogeneous soil with sand fraction of 0.5, clay fraction of 0.5, bulk density of $2g/cm^3$, sand density of $2.66g/cm^3$ and water fraction ranging from 0.01 to 0.25. In total, 50 different materials are generated and the inhomogeneous soil is generated randomly in each simulation, using the features provided by gprMax software [24].

The simulations also generated with surface roughness. The majority of the simulations are generated using $\pm 5mm$ surface roughness option. In a few simulations, the roughness level is increased to $\pm 10mm$. Again, the roughness is applied randomly on each data, by using the surface roughness feature of gprMax software [24].

The wires in the C-scan simulations are buried between 1 and 14 cm depth. Besides the wire object, there also exist plastic objects, rocks and landmines and IEDs that are connected to the wire.

The complete list of C-scan simulations are presented in Appendix A. The top-down looking geometries of simulations are listed. The output of preprocessing algorithms of Chapter 4 and the curve reconstruction algorithm of Chapter 5 are presented in Appendix A.

3.3 Validity of Simulation Parameters in Reality

The antenna array is consisting of 17 T/R pair in C-scan simulations, each one is separated with 5 centimetres, while the separation of transmitting and receiving elements in a pair is 2 cm. The dimensions of antenna array is realizable with the use of Vivaldi antennas. There are several systems in the industry using 5 cm spacing in the antenna array [31].

The array collects data at each 1 centimetre displacement in the along-track dimension. In the industry, GPRs are commonly sampling with 5 cm spacing in along-track dimension [31]. Collecting data with 1 centimetre steps could be too time consuming in reality, especially in time critical operations in humanitarian demining. However, this value should not be too large; otherwise some important signals may have been missed. In [32], the effect of spatial sampling is investigated for landmine and IED detection. The effect of spatial sampling would be more critical for wire detection problem, considering its thin structure. There exist prototype systems sampling with 1 cm steps [13] as well. Moreover, it has been observed in the analysis on antenna polarization that the hyperbola signature gets narrowed when the antenna polarization is perpendicular to the wire direction. Using larger spatial sampling steps may result in loss of the target reflection.

T/R pairs are located 3 centimetres above the ground in simulations. Height of the antenna is small for real off-road applications; especially surface can harm the antenna array. However, in the industry, there exist some systems with 4 cm antenna height [8] and the experimental systems working with antenna height of 3 cm above the ground [13]. Moreover, there exist some systems whose radoms directly touches the soil surface [33].

The Yee cell size is used for determining the time step in the simulations. In the C-scan simulations, Yee cell size is chosen as 2 mm. The time step is calculated as 3.85 picoseconds with using the formula in Equation 3.2. In the literature, the sampling intervals of the radars are commonly not stated explicitly, yet there are some studies stating their sampling interval. In [32], sampling interval of the radar was roughly 91 picoseconds. In [33], the sampling interval was 62.5 picoseconds. The one of the best values of sampling interval in the industry was 8 picoseconds as stated in [31]. The sampling interval used in simulations is smaller than the industry standards; however, such a fine value can be reached in few years as the new technologies emerge.

$$\Delta t = \frac{1}{c\sqrt{\left(\frac{1}{\Delta x}\right)^2 + \left(\frac{1}{\Delta y}\right)^2 + \left(\frac{1}{\Delta z}\right)^2}} \tag{3.2}$$

The simulation model is an impulse radar, using Gaussian derivative waveform at the center frequency of 2.5 GHz. The frequency spectrum of the Gaussian Derivative waveform has been presented previously in Figure 3.4. The -10 dB band of the waveform starts from 489 MHz and goes up to 5.528 GHz. The -20dB band of the waveform 151 MHz and goes up to 6.909 GHz. These bands are realizable since utilizing the 200 MHz - 7 GHz band has already achieved in the industry [28]. Although, in reality, the antenna design would be critical for realization of the desired impulsive waveform, especially in time domain. In some cases, it may not be possible to realize the desired waveform using an impulse radar. Therefore, stepped frequency continuous wave ground penetrating radars (SFCW GPR) are being utilized to overcome this problem. In these radars, the frequency domain information are collected from continuous waves at stepped frequencies and there are transformed into time domain data. The equivalent time domain sampling interval is the critical parameter in wire detection problem. In [34], behaviour of SFCW GPRs such as data collection mode and time-frequency transformation method are explained in detail.

Radius of the wire is chosen as 2 mm in the simulations. In [13], the wires with diameter of 3 mm buried 15 cm deep are detected using a dual polarization hybrid system. The radius of command wires can be thin as 0.5 mm in reality. For instance, in [16], unburied command wires with diameter of 0.98 mm are detected using MIMO SAR. However, modelling a wire with 0.5 mm radius required Yee cell size of at most 0.5 mm. Decreasing Yee cell size to 0.5 mm from 2 mm results in increase in the simulation time of 4^4 (the forth power of the scaling factor). In the current configuration, the C-scan simulations take 1 day to complete with 2 mm Yee cell size. However it would take 8 months with 0.5 mm resolution. There exist a trade-off between simulation time and minimum wire radius. The current configuration with 2 mm of Yee cell size is preferred, in order to generate enough number of simulations for evaluation of detection and classification algorithms. However, note that in the previous section with title "Analysis on Simulation Parameters", the radius of wire is investigated. For smaller radii, the amplitude of the signal decreases. Signal may still be detectable with 0.5 mm radius.

The depth of wire changes from 1 cm to 14 cm in the simulations. This is a valid range for real applications. In [14], it's stated that the command wires are generally buried several inches below the ground surface.

Electromagnetic properties of the soil are modelled using the real measurements of various soil types studied by Peplinski in [26]. The inhomogeneous soil modelling is fractally generated using a seeding for randomization inside the gprMax software as explained in [22] and [24].

Surface roughness has been selected as 1 cm deviation for majority of the C-scan simulations, and 2 cm for the rest of the simulations. However, it can be more severe in reality. But again, in order not to increase the size of simulation environment, the roughness level is not increased any further.

CHAPTER 4

GPR SIGNAL PREPROCESSING METHODS

In the literature, there are many studies focusing on the GPR Signal Preprocessing Algorithms such as [35], [31] and [28]. The scope of this thesis to suggest methods to process the raw GPR data and to detect and discriminate the command wires with a high probability of detection and low false alarm rate.

All of the signal preprocessing methods explained in this chapter is applied on a sample C-scan data. The data is obtained from the simulation environment presented in Figure 4.1; which is also the 4^{th} simulation given in Appendix A.

The GPR signal preprocessing methods are divided into 3 sections below, that are ground bounce and mutual coupling removal, depth weighing and pre-screening. In the ground bounce and mutual coupling step, the unwanted high amplitude signals, which are ground bounce and mutual coupling signals, are eliminated and the subsurface reflections are minimized as well. In the depth weighing step, the attenuation effect, which occurs because of the propagation inside a lossy medium, seen in depth axis is reversed. In the prescreening step, the foreground of the signal is amplified and the background is suppressed and unwanted small detections are cleared. At the end of this chapter, the performance of signal preprocessing algorithms are evaluated.

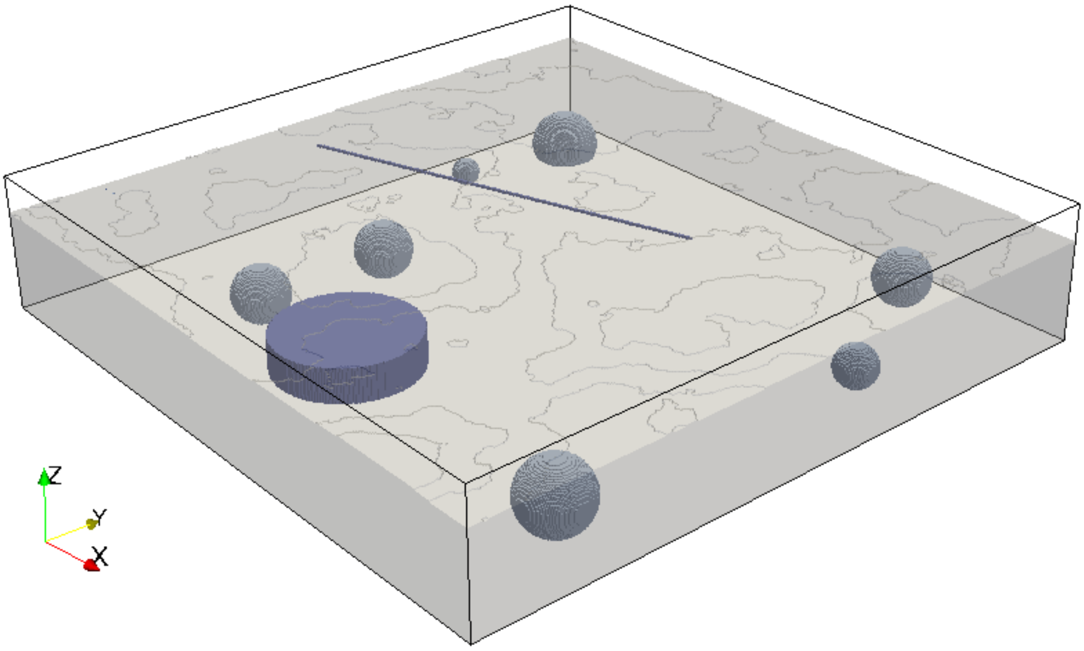

Figure 4.1: The sample C-scan environment used for visualization of the outputs of signal preprocessing methods

4.1 Ground Bounce and Mutual Coupling Removal

GPR data is mostly dominated with the mutual coupling and ground bounce signals. In each transmit/receive pair, a mutual coupling signal will be observed. The time index of this signal is equal to the one-way propagation time of the electromagnetic waves, propagating from the transmitting antenna to the receiving antenna in the air medium. The ground bounce signal is the main reflection from the ground surface. Therefore the total distance that electromagnetic wave propagates is equal to the distance from transmitting antenna to the ground and from ground to the receiving antenna. As a consequence, the signal will be observed at the time value equal to the one-way electromagnetic propagation time of this distance in the air medium. In almost every case, these two signals will be quite larger than the target signal. Without eliminating these signals, it would be impossible to make reliable detections. Therefore, a ground bounce and mutual coupling removal process should be applied to the raw data. The ground bounce and mutual coupling removal process is also known as clutter reduction in the literature. There are some methods used for ground bounce removal; including time gating, mean subtraction, median subtraction and PCA [36]. These methods are explained in following sections. There exists also some sophisticated ground bounce removal algorithms such as ICA in [36], DILBERT in [37], and adaptive ground bounce removal algorithm [38]. In [39], a novel method that estimates the parametric damped exponentials adaptively for clutter reduction is proposed. In [40], a subspace decomposition method is used for removing ground bounce and stationary clutter. Yet, the performance of these algorithms are debatable compared to the processing power needs; especially when the simple algorithms can achieve the same performance [41].

4.1.1 Time gating

The easiest yet effective ground bounce and mutual coupling removal method is time gating. In this method, the raw data is clipped after some known index. The process is described in Algorithm 1. For each cross-track and along-track positions, first L samples in A-scan is gated out.

$\mathbf{X}$ is the raw GPR data, in the dimensions of I x J x K, where I is the number of cross-track positions, J is the number of along-track positions and K is the number of depth bins. $L*$ is a predefined clipping length. $\mathbf{Y}$ is the output of ground bounce and mutual coupling removal algorithms, whose size is I x J x $K - L*$. Throughout the thesis, I is 17, J is 81 as defined previously and K is 1040, since time windows of the simulation was 4 ns, while the sampling time was 3.849 picoseconds. $L*$ is determined as 220 empirically. Use of smaller $L*$ resulted in worse ground bounce removal, while use of higher $L*$ resulted in minimum detectable depth. 220 value is chosen since it eliminates ground bounce and mutual coupling signals effectively, and minimum detectable depth is found to be smaller than 1 cm.

The output of this algorithm is shown in Figure 4.2. Note that, due to the high amount of subsurface reflections, the contrast is selected different for this method than the rest of ground bounce and mutual coupling removal methods.

Algorithm 1 Ground Bounce and Mutual Coupling Removal: Time gating

for $i = 1, \quad i <= I, \quad i++$ **do**

  for $j = 1, \quad j <= J, \quad j++$ **do**

    $\mathbf{Y}(i, j, k) \leftarrow \mathbf{X}(i, j, k + L*)$

  end for

end for

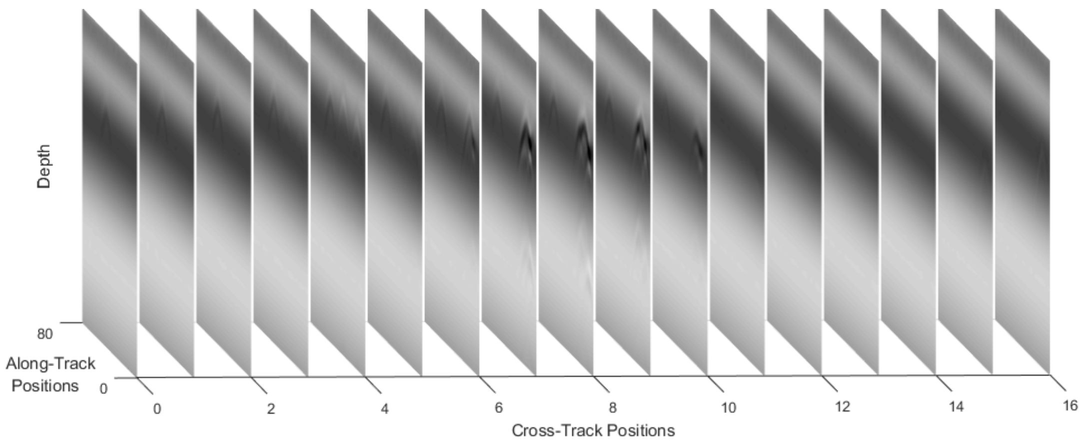

Figure 4.2: Ground bounce and mutual coupling removed C-scan data using time clipping method

This method lacks the capability of eliminating the subsurface reflections. It also lacks the capability of adapting the change in the time indices of ground bounce signal. Mutual coupling signal mostly stays at the same time index, since it may only change when the distance between transmitting and receiving antennas change. However, the time index of ground bounce signal may change especially when the GPR is mounted on a vehicle; since distance between antenna pair and the soil surface changes as it moves. Therefore, an algorithm should track the ground bounce peak location and apply time gating according to the calculated point [41]. The approach is described in Algorithm 2. For each along-track and cross-track positions, the index of the highest amplitude is found and data is clipped L samples after the peak location.

$\mathbf{X}$ is the raw GPR data, in the dimensions of I x J x K. L is the length of additional clipping in time axis, which is applied after the peaks of A-scan signals. $k*$ is the time index, where the A-scan signal has the highest amplitude. $\mathbf{Y}$ is the output of ground bounce and mutual coupling removal algorithms, whose size is I x J x K_2, where K_2 is adjusted previously, guaranteeing that the length of clipped A-scan data in depth axis is larger or equal than K_2. Throughout the thesis, K_2 is determined as 800, since for all of the simulations in Appendix A, the lengths of clipped data are always bigger than 800. Moreover, L is determined as 110 empirically, since smaller values of L leads to decreased removal performance, while larger values affect minimum detectable depth.

Algorithm 2 Ground Bounce and Mutual Coupling Removal: Peak finding and time gating

for $i = 1, \quad i <= I, \quad i++$ **do**
    for $j = 1, \quad j <= J, \quad j++$ **do**
        $k* \leftarrow \underset{k}{\operatorname{argmax}} |X(i,j,k)|$
        $\mathbf{Y}(i,j,k) \leftarrow \mathbf{X}(i,j,k+k*+L)$
    end for
end for

Note that the peak location may be adaptively updated and tracked for more complex off-road conditions. It's reported that when the receiving antenna touches vegetation physically; the distortions may be even greater than the ground bounce signal, resulting in incorrect peak estimations. Therefore, at these instants, the adaptive peak tracking method is a necessity in order to eliminate the peak miscalculation [42].

Note that, mutual coupling signal should also be considered; the amplitude of mutual coupling may be greater than ground bounce signal, depending on the design of the GPR system. The sample C-scan data has roughly same peak location for each scan point; although it had considerable roughness. This leads visibly no difference in the output. Therefore, the output of this improvement is not presented. However, this improvement is a must for real time applications, where the distance between antenna array and the soil can vary significantly.

4.1.2 Mean and Median subtraction

This method simply calculates the mean or the median of the all values in the C-scan data for a specific depth bin, and creates a median/mean vector for all depth bins. This vector is subtracted from each A-scan vector in the C-scan data. The pseudo-code is given in Algorithm 3. $\mathbf{X}$ is the raw GPR data with the size of I x J x K, $\mathbf{Y}$ is the output of ground bounce and mutual coupling removal algorithm having same size as $\mathbf{X}$. $\underline{m}_{median}$ and$\underline{m}_{mean}$ are median and mean subtractions vectors of length K. In Figure 4.3 and 4.4, the mean and median subtractions applied on C-scans are presented.

Algorithm 3 Ground Bounce and Mutual Coupling Removal: Mean & Median Subtraction

for $k = 1, \quad k <= K, \quad k++$ **do**
    $\underline{m}_{median}(k) \leftarrow median(\mathbf{X}(:,:,k)$
    $\underline{m}_{mean}(k) \leftarrow mean(\mathbf{X}(:,:,k)$
end for

for $i = 1, \quad i <= I, \quad i++$ **do**
    for $j = 1, \quad j <= J, \quad j++$ **do**
        $\mathbf{Y}(i,j,k) = \mathbf{X}(i,j,k) - \underline{m}(k)$
    end for
end for

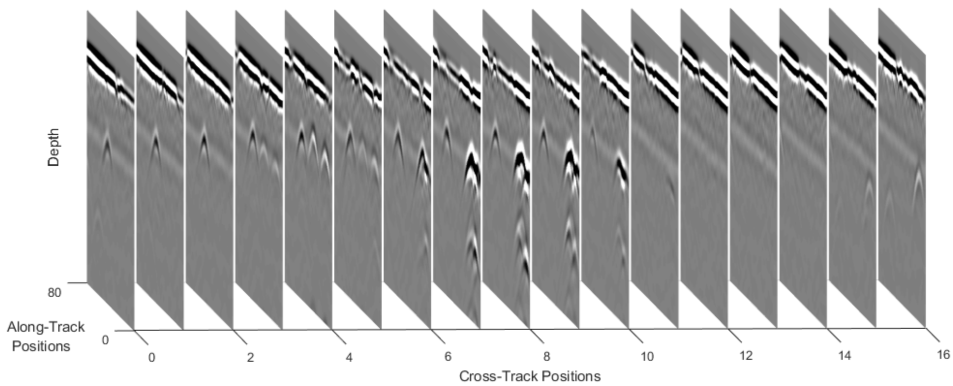

Figure 4.3: Ground bounce and mutual coupling removed C-scan data using mean subtraction method

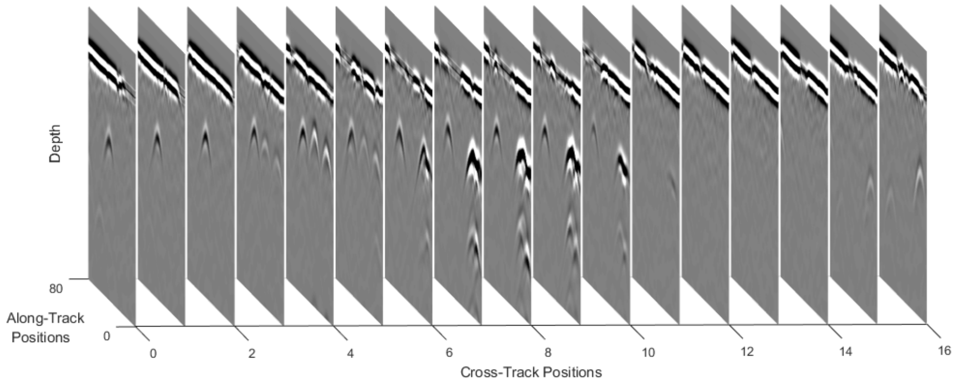

Figure 4.4: Ground bounce and mutual coupling removed C-scan data using median subtraction method

Note that result obtained from mean subtraction has some visible bands with high amplitude at the same depth bins that targets are observed, due to incorrect subtraction caused by biased estimation. On the other hand, median subtraction is not affected from the existence of an high amplitude target, because of its nature.

It should also be noted that, the ground bounce and mutual coupling signals are still considerably dominant; therefore a time clipping algorithm should be applied in order to completely eliminate the ground bounce and mutual coupling signals. Since, only buried wires are investigated in this thesis, use of time clipping is appropriate. Combined solution is explained in Algorithm 4.

4.1.3 Principal Component Analysis

The principal component analysis (PCA) is another ground bounce and mutual coupling removal method that can be applied [43], [33]. It assumes that the ground bounce and mutual coupling signals are the major signal returns, and the rest of the signal parts are very small compared to this part. In this method, first the 2-D data, single B-scan, is decomposed using Singular Value Decomposition (SVD). The rank of the B-scan can be at most equal to the number of along track positions. SVD of a two dimensional matrix $\mathbf{X}$ of size K x J ($K \gg J$) can be expressed as Equation 4.1.

$$\mathbf{X} = \mathbf{U}\mathbf{D}\mathbf{V}^T \tag{4.1}$$

Where $\mathbf{U} = [\underline{u}_1, ..., \underline{u}_J]$ is a matrix of size K x K and $\mathbf{V} = [\underline{v}_1, ..., \underline{v}_J]$ is a J x J matrix of orthonormal basis vectors and $\mathbf{D}$ is a KxJ matrix, whose diagonal entries are the singular values in the decreasing order. The principal component analysis assumes that the clutter is spanning the first p singular vectors. Therefore, signal is projected onto the orthogonal subspace to reduce the clutter. The projection onto the orthogonal subspace can be expressed as Equation 4.2. $\mathbf{Y}$ is the same size of $\mathbf{X}$. SVD is applied on the B-scans of each T/R pair separately. The result is presented in Figure 4.5. It has been seen that first 3 singular values are related with clutter, by looking the time index of the signal. The data is projected on the subspace orthogonal to the first 3 singular vectors.

$$\mathbf{Y} = \sum_{j=p+1}^{J} \mathbf{D}(j, j)\underline{u}_j\underline{v}_j^T \tag{4.2}$$

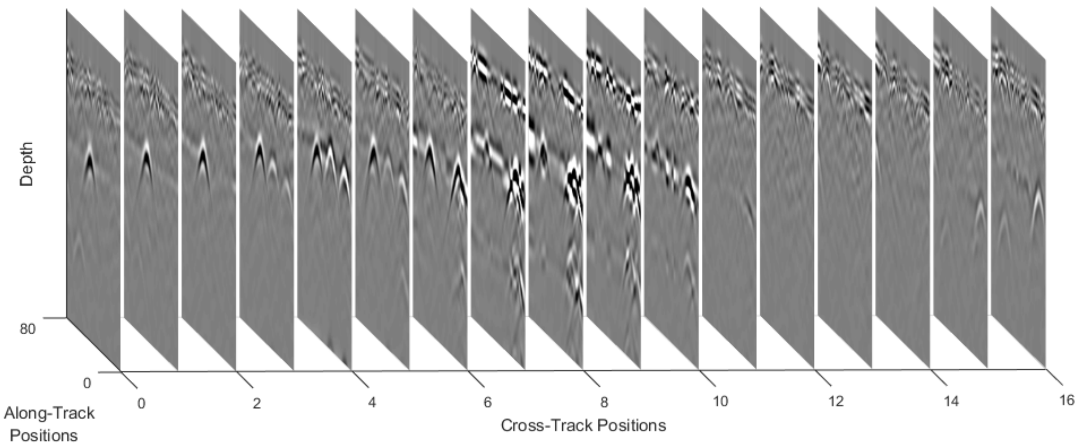

Figure 4.5: Ground bounce and mutual coupling removed C-scan data using PCA method applied on each B-scans separately

PCA algorithm shows promising results at especially eliminating the ground bounce signal for extremely shallow and above surface points. However, this study mainly focuses on buried wires. Moreover, PCA is a computationally costly algorithm.

4.1.4 Utilized Ground Bounce and Mutual Coupling Removal Method

There exist many solutions for ground bounce and mutual coupling removal as stated in previous subsections. In this study, peak tracking, time clipping and median subtraction is utilized as the ground bounce and mutual coupling removal algorithm because of two reasons.

The first reason is that the computational requirements of this method is realizable compared to more complex algorithms such as PCA, ICA [36] or damped exponential [39] methods.

The second reason is that median filtering has shown the best performance for minimizing the subsurface reflections as seen in Figure 4.4, compared to mean subtraction given in Figure 4.3. Mean subtraction reflections especially in case of a strong target reflection, such as the reflections of a landmine, since these high amplitude reflections act like a dominant component in GPR data. PCA has shown promising results, but the computational cost of PCA is a serious concern.

For each cross-track and along-track position, peak alignment and time gating is applied. After this, the median vector is obtained for each depth bins and the median subtraction is applied to the gated signal. The utilized approach is described in Algorithm 4.

L is the length of additional time clipping applied after ground bounce peak, $k*$ is the time index of the peak signal in each A-scan, $\underline{m}$ is the median subtraction vector, $\mathbf{X}$ is the raw input data of size I x J x K and $\mathbf{Y}$ is the output of utilized ground bounce and mutual coupling removal algorithm, in the size of I x J x K_2, where K_2 is predefined such that it guarantees that the length of clipped A-scan data is larger or equal than K_2 for each along-track and cross-track position.

The result of this method is presented in Figure 4.6. The next signal preprocessing steps (depth weighing and prescreening) will be studied using this algorithm applied on the data in prior.

Algorithm 4 Ground Bounce and Mutual Coupling Removal: Utilized Method

for $i = 1, \quad i <= I, \quad i++$ **do**
  for $j = 1, \quad j <= J, \quad j++$ **do**
    $k* \leftarrow \underset{k}{\operatorname{argmax}} \mathbf{X}(i, j, k)$
    $\mathbf{Y}(i, j, k) \leftarrow \mathbf{X}(i, j, k + k * + L)$
  end for
end for
for $k = 1, \quad k <= K, \quad k++$ **do**
  $\underline{m}(k) \leftarrow median(\mathbf{Y}(:, :, k)$
end for
for $i = 1, \quad i <= I, \quad i++$ **do**
  for $j = 1, \quad j <= J, \quad j++$ **do**
    $\mathbf{Y}(i, j, k) = \mathbf{Y}(i, j, k) - \underline{m}(k)$
  end for
end for

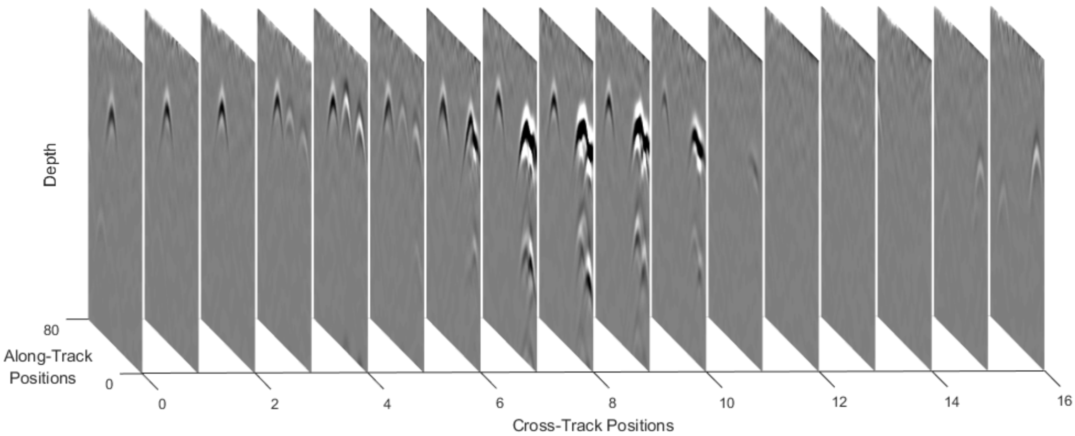

Figure 4.6: Ground bounce and mutual coupling removed C-scan data using peak tracking, time clipping and median subtraction method

4.2 Depth Weighing

The electromagnetic waves get attenuated as they propagate in a lossy medium. Therefore, a whitening process should be applied to the data along depth axis in order to eliminate the depth dependent attenuation effects. An ideal whitener would bring the powers of target reflections from different depths to the same level. Hence, depth whitening can be considered as an equalization process. There are few methods in the literature, one of them is covered in this study; which is depth dependent whitening. Moreover, another method, logarithmic weighing, is proposed for the depth weighing as well. These methods are explained below.

4.2.1 Depth Dependent Whitening

In this method, the C-scan data is divided into several overlapping depth segments. For each depth segment, the mean (μ) and variance (σ) of all voxels are estimated. The main assumption in this method is that the mean and variance of the signal does not vary much in the chosen depth segment. The algorithm can be made adaptive as done in [31]; the mean and variance values can be adaptively calculated as the vehicle and GPR system moves. Then, using these mean and variance values, the signal can be whitened along depth axis. The algorithm is explained in Algorithm 5.

Algorithm 5 Depth Weighing: Depth dependent whitening

for $k = 1, \quad k <= K, \quad k++$ **do**

    $\underline{y} \leftarrow \mathbf{Y}(:,:,k)$

    $\mu \leftarrow \sum \underline{y}$

    $\sigma \leftarrow (\underline{y} - \mu)^T(\underline{y} - \mu)$

    $\mathbf{Z}(:,:,k) \leftarrow \frac{\underline{y}-\mu}{\sigma}$

end for

$\mathbf{Y}$ is the input of depth weighing block in the size of I x J x K_2. $\underline{y}$ is the vectorized form of C-scan data at the k^{th} depth index, which has the length of I times J. μ is the calculated mean value of the depth bin. σ is the calculated standard deviation of the depth bin. $\mathbf{Z}$ is the output of depth weighing block in the the same size of $\mathbf{Y}$. The C-scan output of this algorithm is presented in Figure 4.7.

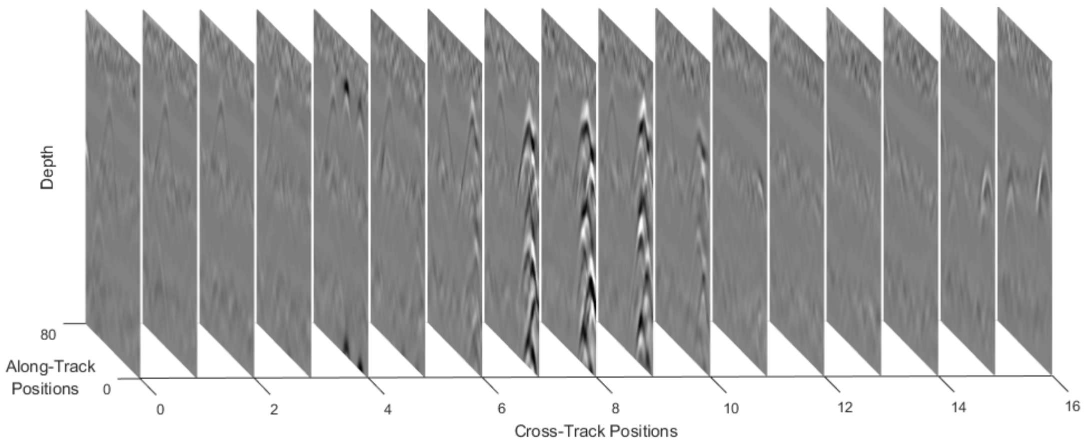

Figure 4.7: Whitening applied on C-scan data

This method yet lacks a very fundamental property required for an ideal depth whitener; it should equalize the strength of the signals coming from different depths. However, this approach equalizes the signal, without any concern of target existence. Hence, at some regions of the soil; where the signal amplitude varies very little, the amplitude of the whitening output increases drastically due to the low standard deviation. Therefore, this algorithm is not very suitable for weighing.

4.2.2 Proposed Weighing Method

Since depth dependent adaptive whitening is not suitable for all kinds of GPR data, especially when the subsurface reflections does not vary much, another method should be investigated. Logarithmic weighing is proposed in this study for depth weighing, since it does not create an unbalance between the depth bins which is clearly seen in Figure 4.7.

Once the logarithmic weighing vector is generated, for each cross-track and along-track positions, the A-scans are multiplied with the weighing vector element wise; in other words, Hadamard product is applied on A-scans with logarithmic weighing vector. The procedure is described in Algorithm 6. $\underline{w}$ is the weighing vector of length K_2, k is the depth index number, and A_w is the predefined positive amplification value, which is determined as 10 dB, empirically. Use of very high A_w will result in decreased signal strength for the shallow points of the soil, whereas use of small A_w will result in decreased performance of the depth weighing. For instance, when A_w is set to zero, the depth weighing step has no effect on the data. The result of proposed method is presented in Figure 4.8. $\mathbf{Y}$ is the input of depth weighing block in the size of I x J x K_2. $\mathbf{Z}$ is the output of depth weighing block, having same size as $\mathbf{Y}$.

Algorithm 6 Depth Weighing: Proposed method - Logarithmic weighing

$\underline{w}(k) \leftarrow 10^{A_w k/K_2}$
for $i = 1, \quad i <= I, \quad i++$ **do**
  for $j = 1, \quad j <= J, \quad j++$ **do**
    $\mathbf{Z}(i,j,:) \leftarrow \mathbf{Y}(i,j,:) \circ \underline{w}$ Hadamard product
  end for
end for

A future study can be suggested here for adaptive calculation of the A_w value, in order to adept the changes in the soil; since attenuation of the soil highly completely dependent on the electromagnetic properties of the soil.

The logarithmic weighing along depth has shown considerably better results compared to whitening operation. Therefore, it's been chosen as the suitable method for depth weighing. The next algorithm steps are studied on the data processed with this algorithm in prior.

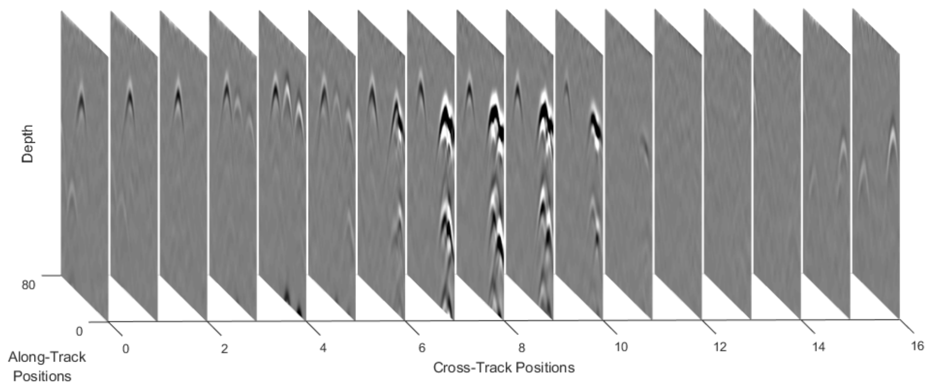

Figure 4.8: Weighing along depth axis applied on C-scan data

4.3 Pre-screening

After the weighing, the data would be almost ready for detection. Yet, still the target signal wouldn't be enough strong to be detected easily. The prescreening process is applied as a remedy; which is used for separating the background and foreground. The foreground is defined as the anomaly on the data, which shows an abnormal pattern, different than the regularly occurring patterns in the background. There are some prescreening algorithms in the literature. In this study two methods are investigated; namely, least mean squares (LMS) [28] and robust principal component analysis (RPCA) [44] algorithms. The methods are explained in the following subsections.

4.3.1 Least Mean Squares Pre-screener

Least Mean Squares algorithm is well studied in the literature. Especially 2-D LMS has many examples in the literature such as [45]. Yet, there are few studies focusing on 3-D LMS, [46]. The high computational power required for the algorithm leaded researches to study faster and alternative ways to perform LMS [47]. For instance, KLMS can also be applied to GPR data as a prescreener as studied in [48] and [49], which requires less computational power.

2-D LMS requires less computational power than 3-D one, as expected as explained in [28]. The algorithm will run in parallel for each transmit/receive pair and each depth segment separately. The LMS weigh vector and LMS output is updated every time the GPR system moves along-track. Firstly, for each depth segment, a cell is constructed. The middle point of the cell is the point of interest, and it is guarded by a few guard bins. The LMS filter, $\underline{s}$, is initialized as a constant vector having unity energy. Then, for each cross-track and along-track positions, LMS filtering is applied on the depth segment. In the LMS filtering, first the product of LMS filter with samples of depth weighing output inside the cell is computed. The error value, e is calculated as the difference of the middle value from the calculated value. The LMS filter is updated using the updating coefficient, μ, the error value and the normalized samples of depth weighing output inside the cell. If the absolute of calculated error value is greater than the detection threshold, it is written inside **T** matrix, which is the output of prescreener in the size of I x J x NC. Otherwise, the corresponding value in **T** matrix is set to zero.

The algorithm is described in Algorithm 7. cl is the length of the LMS cells along depth axis which should be odd number, gl is the length of guard bins, cs is the step size of cells in depth axis. NC is the number of cells to be processed, mp is the middle point of the LMS cells; which corresponds to the point of interest. K_2 is the number of depth bins, $\underline{ind}$ is a vector of indices of depth axis to be processed. The LMS filter coefficient vector is $\underline{s}$, $\underline{u}$ is the input vector for a given cross-track, along-track and depth segment.

The output of the algorithm is presented in Figure 4.9. The top-down looking energy map of the processed data is presented in Figure 4.10. In this presentation method, the power along each A-scan is summed and plotted in the along-track axis and cross-track axis. The contrast is adjusted to enhance the visibility of small clutter-like objects. The calculation of energy map is described by Equation 4.3. **E** is the energy map, presented in Figure 4.10. **T** is the output of prescreener.

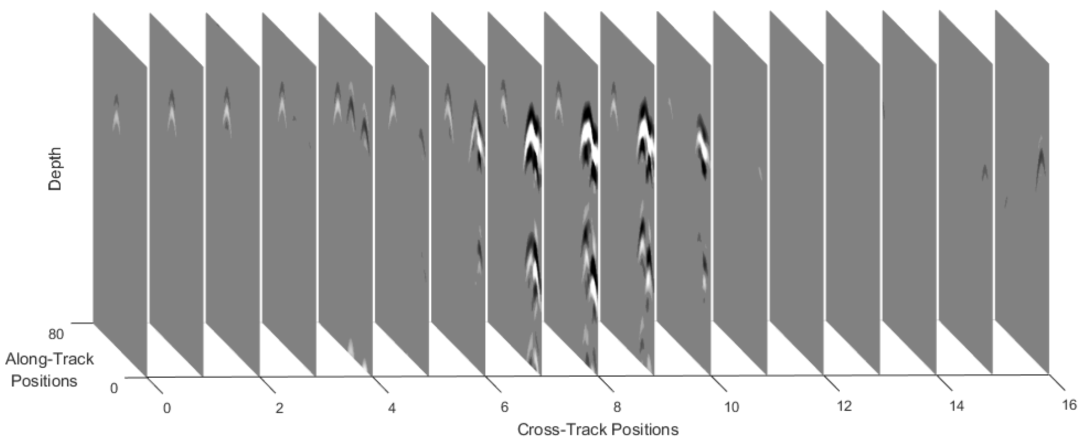

Figure 4.9: 2-D LMS pre-screener applied on C-scan data

Algorithm 7 Prescreener: 2-D LMS

$mp \leftarrow (cl-1)/2+1$, the mid point

$NC \leftarrow \left\lfloor \frac{K_2}{cl} - 1 \right\rfloor * \frac{cl}{cs}$, the number of cells

for $d = 0, \quad d < NC, \quad d++$ **do**

  $\underline{ind} \leftarrow [d*cs+1 : d*cs+c]$

  $\underline{ind}(mp-gl : mp+gl) \leftarrow [\,]$

  $\underline{s} \leftarrow \underline{1}_{(1,\, cl-2*gl+1)}$

  $\underline{s} \leftarrow \frac{\underline{s}}{\|\underline{s}\|}$

  for $i = 1, \quad i <= I, \quad i++$ **do**

    for $j = 1, \quad j <= J, \quad j++$ **do**

      $\underline{u} \leftarrow \mathbf{Z}(i, j, \underline{ind})$

      $e \leftarrow \mathbf{Z}(i, j, d*cs+mp+1) - \underline{u}^T \underline{s}$

      $\underline{s} \leftarrow \underline{s} + \mu * e * \frac{\underline{u}}{\|\underline{u}\|}$

      $\underline{s} \leftarrow \frac{\underline{s}}{\|\underline{s}\|}$

      if $|e| > Threshold$ **then**

        $\mathbf{T}(i, j, d+1) \leftarrow e$

      else

        $\mathbf{T}(i, j, d+1) \leftarrow 0$

      end if

    end for

  end for

end for

3-D LMS is the expansion of 2-D LMS into the third dimension as suggested in [46]. Due to the increase in the dimensionality, the computational power required for this algorithm is quite large; which makes it hard to implement in real-time systems. 3-D LMS algorithm works as following as described in [46]. Firt, there processing planes are obtained; which are the depth slice, B-scan slice along-track and B-scan slice cross-track. Then the data is taken out using a guard band. Then, the points in a predefined neighbourhood of the point of interest is taken and vectorized. From this point on, LMS algorithm works same and the prediction errors in these three planes are summed using a weighing for each plane. In [46], weighing vectors are determined empirically.

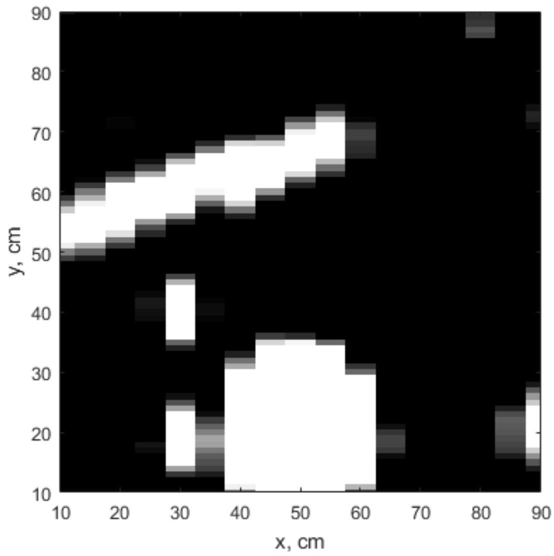

Figure 4.10: The energy map of the C-scan data after 2-D LMS pre-screener

$$\mathbf{E}(i,j) = \sum_{k=1}^{NC} \mathbf{T}(i,j,k)^2 \tag{4.3}$$

4.3.2 Robust Principal Component Analysis Pre-screener

Robust principal component analysis is rather a recent method [44] applied as a GPR prescreening algorithm. RPCA is a decomposition method, which separates the sparse foreground information from the background. RPCA algorithm decomposes the preprocessed 2-D GPR input signal, such as cross track B-scans, which are represented as X matrices in this subsection, into L and S matrices, where L is low rank and S is sparse matrices as in Equation 4.4. S is considered as the prescreening output. It is applied on each B-scans separately, since RPCA does not support 3-D computations yet.

$$X = L + S \tag{4.4}$$

The estimation of S and L matrices can be done by complex optimization of Equation 4.5. There are several numerical solutions in the literature for the complex optimization problem of RPCA [50].

$$\left(\hat{\mathbf{L}}, \hat{\mathbf{S}}\right) = \underset{\mathbf{L},\mathbf{S}}{\operatorname{argmin}} \|\mathbf{L}\|_* + \lambda \|\mathbf{S}\|_1 \tag{4.5}$$

In [44], RPCA is applied to the frequency domain GPR data. The sparse output of the RPCA is transformed back to time domain. However, performance of RPCA on time domain was also promising for the simulated data given in Appendix A. Figure 4.11 shows the sparse output of RPCA applied on the B-scan simulation provided. The energy map of the processed C-scan data is presented in Figure 4.12. Energy map is obtained with Equation 4.3.

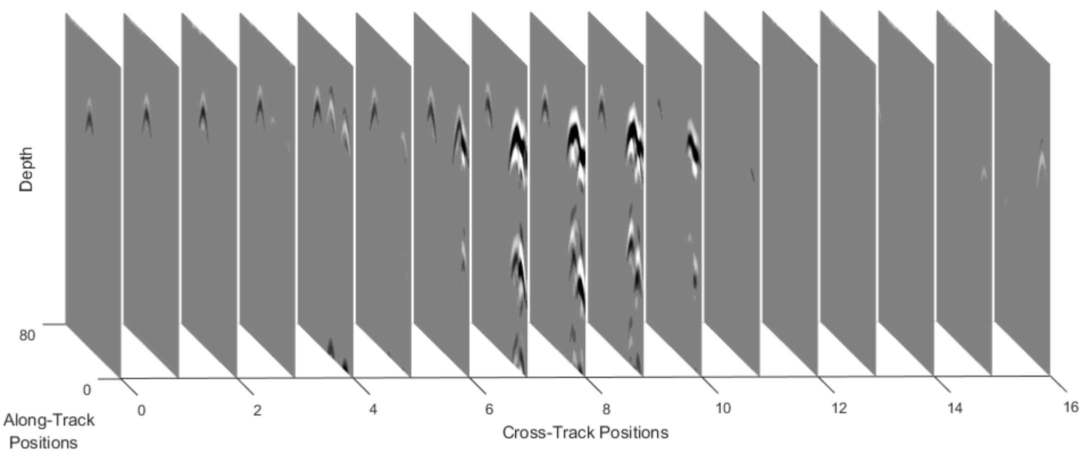

Figure 4.11: 2-D RPCA pre-screener applied on C-scan data

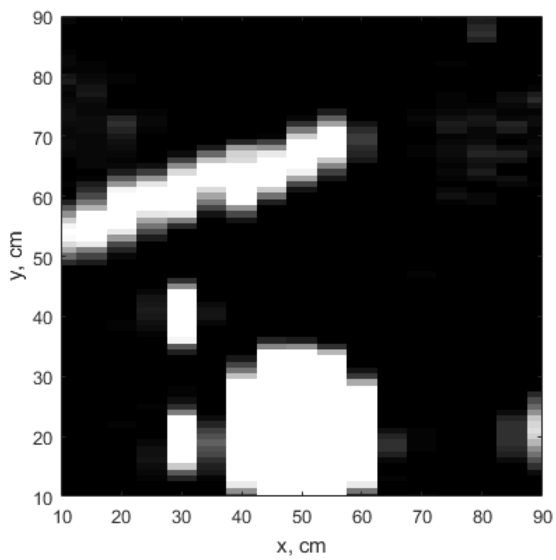

Figure 4.12: The energy map of the C-scan data after 2-D RPCA pre-screener

4.3.3 Proposed Prescreening Algorithm

As described earlier, 3-D LMS needs great computational power, hence it's not very suitable for real-time systems. RPCA is a very promising prescreening algorithm; yet the complex optimization problem in RPCA is a great concern for computational power in real time systems. On the other hand, 2-D LMS is a reliable and well studied algorithm. Hence, in this study, 2-D LMS is chosen as a prescreening algorithm. Mathematical morphologies and connected component analysis is conducted on the pre-screener output in order to enhance the detection performance and eliminate false detections. The connected component analysis and the mathematical morphologies that are used and are explained in Appendix C1 and C2 respectively.

The proposed pre-screener, the morphologically improved 2-D LMS filtering, is explained in Algorithm 8. The structure of the algorithm until the 21^{th} line is identical with the Algorithm 7 except **B** matrix, which is the binary detection matrix having same size with **T** and values of 0 and 1. After this point, first the 3-D structuring element, **se**, used in mathematical morphologies is defined. The element is defined as a 3-D matrix of ones in the dimensions of 2 x 2 x 40. Then, using **se**, the **B** matrix is dilated and **D** is obtained, which is in the same size of **B**. Then, connected component analysis is performed. For each connected component, the volume, v, of the groups are calculated. If the volume is smaller than the predefined volume threshold, $Threshold_{vol}$, then the connected component group in the dilated image is cleared. After this, **D** image is eroded back using **se**, and **E** matrix is obtained. As the final step, the **T** matrix is multiplied with binary **E** matrix element-wise, in order to clear the detections that are cleared with binary mathematical morphologies. $\circ$ symbol is used for Hadamard product.

The result of Morphologically Improved 2D LMS algorithm is presented in Figure 4.13. The energy map of the Morphologically Improved 2-D LMS method is presented in Figure 4.14.Energy map is obtained with Equation 4.3.

Algorithm 8 Proposed Prescreener: Morphologically Improved 2-D LMS

for $d = 0, \quad d < NC, \quad d++$ **do**
  $\underline{ind} \leftarrow [d * cs + 1 : d * cs + cl]$
  $\underline{ind}(mp - gl : mp + gl) \leftarrow [\,]$
  $\underline{s} \leftarrow \underline{1}_{(1,\, cl-2*gl+1)}$
  $\underline{s} \leftarrow \frac{\underline{s}}{\|\underline{s}\|}$
  for $i = 1, \quad i <= I, \quad i++$ **do**
    for $j = 1, \quad j <= J, \quad j++$ **do**
      $\underline{u} \leftarrow \mathbf{Z}(i, j, \underline{ind})$
      $e \leftarrow \mathbf{Z}(i, j, d * cs + mp + 1) - \underline{u}^T \underline{s}$
      $\underline{s} \leftarrow \underline{s} + \mu * e * \frac{\underline{u}}{\|\underline{u}\|}$
      $\underline{s} \leftarrow \frac{\underline{s}}{\|\underline{s}\|}$
      if $|e| > Threshold$ **then**
        $\mathbf{T}(i, j, d + 1) \leftarrow e$
        $\mathbf{B}(i, j, k) \leftarrow 1$, Binary detections
      else
        $\mathbf{T}(i, j, d + 1) \leftarrow 0$
        $\mathbf{B}(i, j, k) \leftarrow 0$,
      end if
    end for
  end for
end for
$\mathbf{se} \leftarrow \mathbf{1}_{(2,2,40)}$, the Structuring element
$\mathbf{D} \leftarrow \mathbf{B} \oplus \mathbf{se}$, the Dilated 3-D image
$ConnectedComponentAnalysis(\mathbf{D})$
for $\forall$ Connected Components **do**
  $v \leftarrow volume$(Connected Component $_i$)
  if $v < Threshold_{vol}$ **then**
    $\mathbf{D}$(Connected Component $_i$) $\leftarrow 0$
  end if
end for
$\mathbf{E} \leftarrow \mathbf{D} \ominus \mathbf{se}$, the Eroded 3-D image
$\mathbf{T} \leftarrow \mathbf{T} \circ \mathbf{E}$, Hadamard product

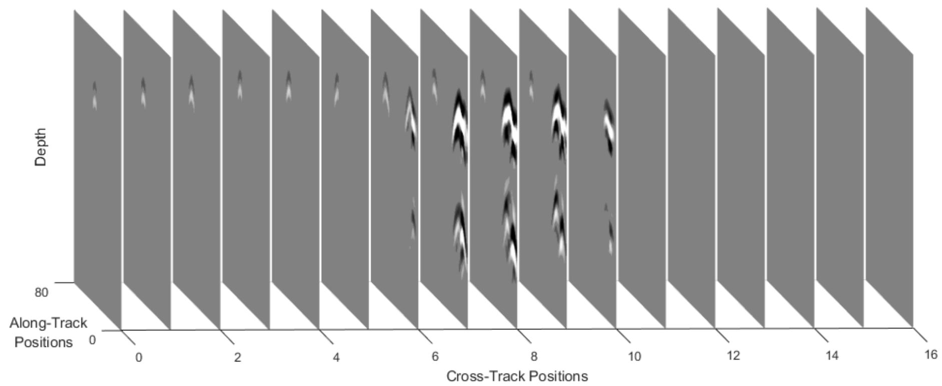

Figure 4.13: Morphologically Improved 2-D LMS prescreener applied on C-scan data

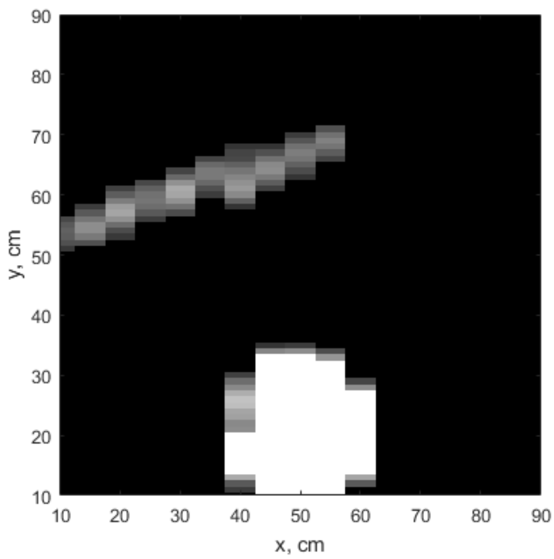

Figure 4.14: The energy map of the C-scan data after Morphologically Improved 2-D LMS prescreener

Note that, the use of mathematical morphologies and connected component analysis, all of the clutter like objects in the sample C-scan data is cleaned. These tools are presented in Appendix C1 and C2. Since, all of the small and irrelevant points are cleaned out in the image, the contrast is adjusted to enhance the visibility of energy difference between the landmine object and wire object.

4.4 Analysis on the Performance of Utilized Preprocessing Methods

First, ground bounce and mutual coupling removal is applied on raw GPR data, using time clipping and median filtering. The equalization along depth axis is achieved with logarithmic weighing. The possible wire locations are detected using the morphologically improved version of 2-D LMS filtering.

There are few parameters in the algorithms. In the ground bounce and mutual coupling removal section, time clipping length in Algorithm 4 was adjusted to a predefined value. In depth weighing section, the amplification value in Algorithm 6 was adjusted to a predefined value as well. In the prescreening section, LMS cell size, guard cell size, LMS updating coefficient, size of structuring element of mathematical morphologies, neighbourhood definition of connected component analysis, volume threshold was the fixed parameters in Algorithm 8. The detection threshold in Algorithm 8, is however, is the real threshold value of the overall system. Therefore, the performance is investigated for changing values of the detection threshold.

4.4.1 Definition of Detection and False Alarm for Performance Analysis

The detections and false alarms are evaluated on XY plane, using the energy map described by Equation 4.3 and seen in Figure 4.14.

Real wire locations in XY plane is trimmed at the boundaries of scanning grid. For instance, if a wire exceeds 90 cm in X direction, the real wire location is clipped after this point. If there is a detection in the prescreener output, not farther than 5 cm to the real wire position, then it is called detection.

Detection length ratio is the ratio of detected length to the total length of the wire. It can be said that, when the wire is partially detected, the detection ratio will be bigger than zero but smaller than one for an existing wire and it is called a detection.

False alarm rate is the ratio of the total number of detections in the energy map, farther than 10 cm to any existing wire location to the total number of scanning positions in the C-scan, which is equal to I times J.

4.4.2 Results of Performance Analysis of Preprocessing Algorithms

The results are presented with four graphs. Threshold value is swept from 0.03 to 0.4 level. Note that, these values are all related with the signal amplitudes of the original collected data; therefore they are only meaningful when they are compared with each other.

The probability of detection versus the detection threshold graph is presented in Figure 4.15. The probability of false alarm versus the detection threshold graph is presented in Figure 4.16. Combining probability of detection with probability of false alarm measurements, the receiver operating characteristics, also known as ROC curve is obtained as in Figure 4.17. The detection length ratio; which is based on how long the wire is detected is presented in Figure 4.18.

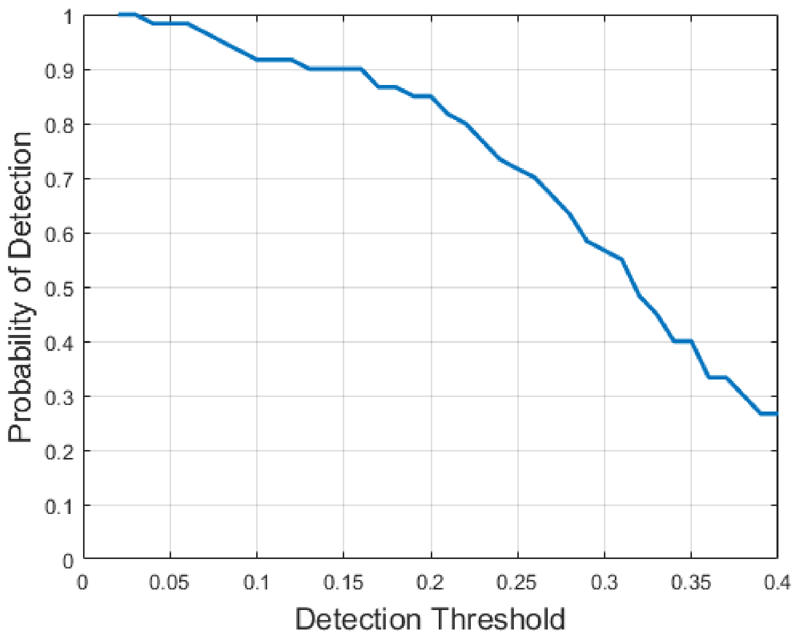

Figure 4.15: The probability of detection versus detection threshold graph of utilized preprocessing methods

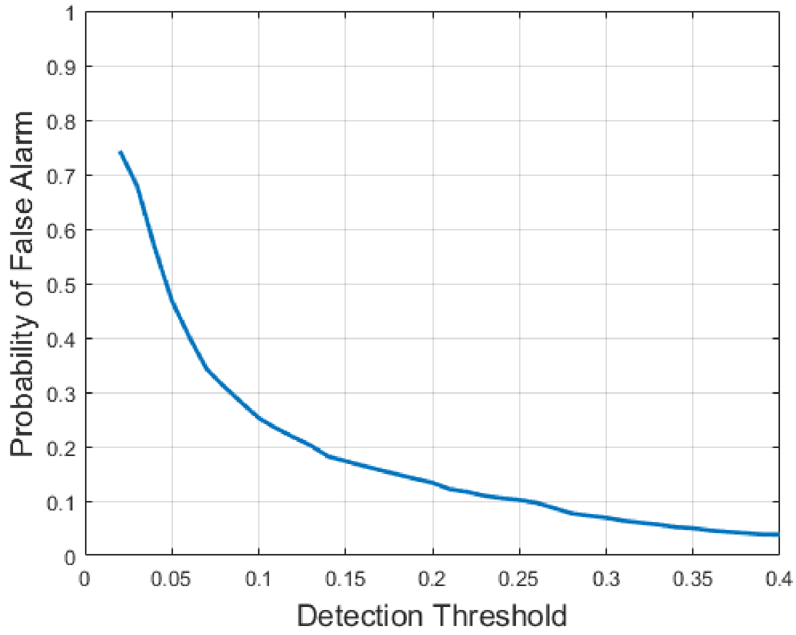

Figure 4.16: The probability of false alarm versus detection threshold graph of utilized preprocessing methods

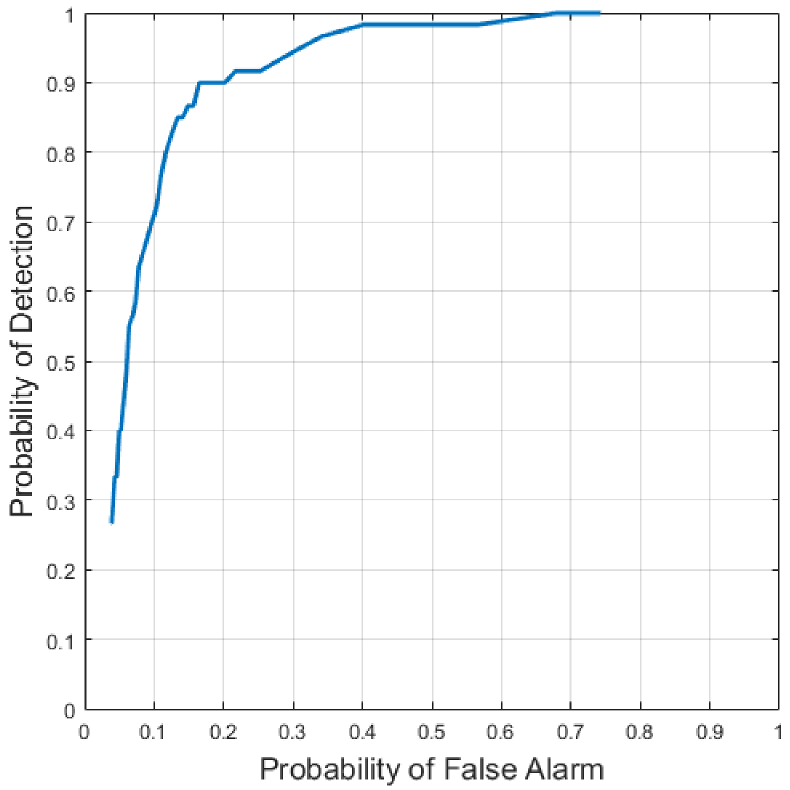

Figure 4.17: The ROC curve of the utilized preprocessing methods, Area under ROC curve: 0.9086

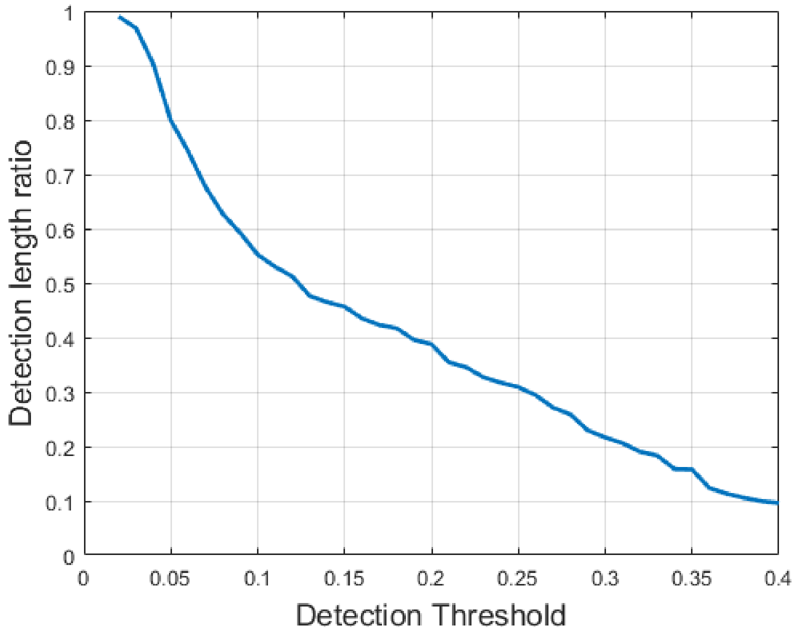

Figure 4.18: The detection length ratio versus detection threshold graph of utilized preprocessing methods

It has been observed from the Figure 4.17, proposed prescreening algorithms can achieve 90% probability of detection, with 16% false alarm rate. It should be noted that, all types of objects other than wires, including landmines, are considered as false alarm in this analysis. The area under ROC curve is calculated as 0.9086.

CHAPTER 5

WIRE FEATURE EXTRACTION AND CLASSIFICATION

The Morphologically Improved 2-D LMS prescreener has grouped the detections that are connected to each other and spanning a volume bigger than a predefined value. In order to determine whether these detections groups are related with wires or not, a classification problem of two classes should be studied.

There are few studies focusing on wire detection problem in the literature, which are investigated in Chapter 1, and there is not a study focusing on detection and classification of wires. The closest matching well-studied detection problem is pipe detection in the literature. In [18], neural networks are used for pipe detection using B-scans. However, study has only focused on hyperbola recognition and assumed a single type of target.

In [51], the length and width features of linear objects are extracted iteratively in GPR images using Radon transform. However, the algorithm works with back-projected GPR images, where depth information has been lost. Moreover, it only works with linear objects; which would fail when the wire is placed in free form. Nevertheless, the study has shown that the width and length features are useful to classify long and thin objects. However in this thesis, another method should be used to extract these features for free form wires.

In [52], some possible features for landmine detection are listed as area, depth, position, energy and their spatial variations. These features has given some insight about what features can be extracted for 3-D wire classification problem.

In Chapter 3, it has been observed that the reflections obtained from a wire is generally weak in terms of signal strength. Moreover, it is not practically possible to distinguish a wire from a stone in a single B-scan. Therefore, it can be said that use of C-scans is compulsory for wire classification. In Chapter 3, the B-scan responses for different wire angles are also investigated. It is observed that, dependent on the angle the hyperbola signature widens and finally becomes a constant line when the wire is placed along-track direction. This phenomenon has also shown in [13]. Moreover, the spatial sampling steps and the polarization of the antenna also played role in the hyperbola signature in wire classification problem. Therefore 2-D hyperbola estimation algorithms such as [29] and [30], are definitely not suitable for wire classification problem.

Another possible feature extraction could have been achieved with convex or concave hull, which can also be implemented on 3-D. However, convex hull will definitely fail at some curvy wire orientations, such as the 13th simulation given in Appendix A. Concave hull, on the other hand, seems more applicable. However, this algorithm only cares the outer boundary of the point cloud. Therefore, concave hull would have problems when the wire reflections collide with the reflections of unwanted clutter objects.

In this study, feature based classification is used in order to classify wires from clutter objects. Target reflections are considered as a point cloud scattered around the wire position, rather than the hyperbolas in B-scans. The curve of the wire in 3-D space should be reconstructed using the point cloud first in order to compute the features and to examine the fitness of the point cloud to the curve in 3-D.

5.1 Curve Reconstruction

There are some 3-D curve reconstruction algorithms in the literature [53], [54] and [55]. Two methods are studied in this section. The first one is the singular value decomposition, which assumes existence of a straight line, although it is impracticable in real applications. The second algorithm is a 3-D curve reconstruction with moving least squares algorithm [53]. 3-D curve reconstruction using MLS algorithm has shown promising results. These methods are explained below.

5.1.1 3-D Line Fitting with Singular Value Decomposition

Singular value decomposition is a powerful tool and it has many applications, including PCA mentioned earlier. It can also be used for estimating the principal direction of the point cloud in 3-D. The indices of the m^{th} connected point cloud in cross-track, along-track and depth positions are listed as $\mathbf{X}_m = [i_m \quad j_m \quad k_m]$. Mean values of i, j, k is subtracted from the $\mathbf{X}$ matrix. Then, the covariance matrix is obtained by $\mathbf{C}_m = \mathbf{X}^T\mathbf{X}$ relation. The singular values of $\mathbf{C}_m = \mathbf{UDV}^T$ are decomposed. The orthonormal basis vector $\underline{u}_1$ in the $\mathbf{U}$ matrix corresponding to the largest singular value in the diagonal $\mathbf{D}$ matrix is the principal axis of the point cloud. The straight line can be represented with a parametric equation in 3-D, passes through the mean values of i, j, k and goes in the direction of $\underline{u}_1$. The pseudo code is given in Algorithm 9. t is the variable used for parametric representation.

Algorithm 9 Straight line estimation using Singular Value Decomposition

1: $[\mu_i \quad \mu_j \quad \mu_k] \leftarrow \left[\frac{1}{N}\sum_n \underline{i}_m(n) \quad \frac{1}{N}\sum_n \underline{j}_m(n) \quad \frac{1}{N}\sum_n \underline{k}_m(n)\right]$
2: $\mathbf{X}_m \leftarrow \left[\underline{i}_m - \mu_i \quad \underline{j}_m - \mu_j \quad \underline{k}_m - \mu_k\right]$
3: $\mathbf{C}_m \leftarrow \mathbf{X}^T\mathbf{X}$
4: $\mathbf{U}\ \mathbf{D}\ \mathbf{V}^T \leftarrow \mathbf{C}_m$: Singular Value Decomposition
5: $[\underline{u}_1 \quad \underline{u}_2 \quad \underline{u}_3] \leftarrow \mathbf{U}$
6: $x \leftarrow \mu_i + \underline{u}_1(1) * t$
7: $y \leftarrow \mu_j + \underline{u}_1(2) * t$
8: $z \leftarrow \mu_k + \underline{u}_1(3) * t$

Line fitting with SVM assumes the existence of a single straight wire. Therefore, this algorithm is not suitable for identifying free-form wires since in Appendix A, majority of the simulations are consisting of curved wires.

5.1.2 3-D Curve Reconstruction with Moving Least Squares

A sophisticated algorithm is required here to reconstruct free form 3-D curves using the point cloud in 3-D; since wires could be placed in any form. There are some studies in the computational geometry literature focusing on the curve and surface reconstruction using point clouds such as [53], [54] and [55].

The method suggested in [53] has initially applied on 2-D, but the author explained the how to expand the method to further dimensions. It is mainly based on moving least squares (MLS) method and author used minimum spanning tree in order to select associated points in 3-D. This method is powerful and promising and well fitting for the command wire detection problem; therefore this method has been utilized in this thesis.

The idea behind the utilized method is to find the linear direction of neighbouring points for each point in 2-D space and applying moving least squares to move the points closer to the regression curve. As the method iterates, the point cloud gets denser and form a curve. The direct application to 3-D is not easy as explained in [53]. Therefore, point cloud is projected on the 2 surfaces that are perpendicular to each other and parallel to the 3-D regression line. After projection, 2-D MLS is used to fit the points on regression curve. The result is projected back to 3-D.

In detail, first the i, j, k indices of a connected component group is mapped to the real dimensions as given in Equation 5.1. For instance, cross-track indices, i, are multiplied by 5 and added with 5 in order to map the indices in the range of 1 to 17 into the range of 10 to 90 centimetres. Along track indices, j are added with 9 in order to map the indices ranging from 1 to 81 into the range of 10 to 90 centimetres. Depth indices, k are divided by a constant, c, which is empirically found. The 3-D curve reconstruction algorithm using MLS is not really dependent on this constant value; a rough value is sufficient. As long as the product of c value in the Equation 5.1 and cs value in the Algorithm 8 is bigger than 40, the algorithm works fine. cs value in Algorithm 8 is selected 1 in order not to skip any depth segments. Hence, c value in the Equation 5.1 is selected as 50.

$$x = 5 + 5i, \qquad y = 9 + j, \qquad z = \frac{k}{c} \tag{5.1}$$

The algorithm contains several optimization problems, which are repeated for all points and the whole procedure is iterated few times to obtain better results. In order to decrease the computational cost of the algorithm, a decimation algorithm can be applied on z indices for each x and y positions since target reflections creates several detections in each A-scan. It can also be achieved by increasing the cell size, cs value, in Algorithm 8 as long as the cells in Algorithm 8 overlap more than 50%.

After this, the following computations are repeated for each point in the connected component group. When all of the points are processed, the algorithm can be repeated for a few iterations to get better results.

In the first step of iterative algorithm, the distances, $\underline{r}$, from the point of interest, $(x(k), y(k), z(k))$, to the all other points in 3-D is calculated with Equation 5.2.

$$\underline{r} = (\underline{x}, \underline{y}, \underline{z}) - (x(k), y(k), z(k)) \tag{5.2}$$

Then, the set of indices whose distances are smaller than a pre-selected value, H, is chosen as in Equation 5.3; whose can be expressed as the points inside a sphere with a radius of H and centred at the point of interest. The subsets of $\underline{x}$, $\underline{y}$ and $\underline{z}$ inside the sphere, which are presented as $\hat{\underline{x}}$, $\hat{\underline{y}}$ and $\hat{\underline{z}}$, are obtained as in Equation 5.4.

$$B = \{n \quad | \quad \underline{r}(k) < H\} \tag{5.3}$$

$$\hat{\underline{x}} = \underline{x}(i), \quad \hat{\underline{y}} = \underline{y}(i), \quad \hat{\underline{z}} = \underline{z}(i), \quad i \in B \tag{5.4}$$

Selection of H value is important since the points inside the sphere with radius H, centred at the point of interest should have a linear trend. In other words;

these points should be forming a point cloud distributed around the principal axis in 3-D. This is achieved with high correlation along the principal axis. If H value is selected too small; then the points would be highly uncorrelated; and the algorithm would fail to find a principal axis. On the other hand when H value is selected too large, the algorithm cannot adept to sharp corners and the curve gets too much smooth. H value is selected as 20 cm, which is found as applicable for wire detection problem empirically. The effect of selection of H is investigated in Figure 5.5 and 5.6, in the end of this section.

The procedure is presented in Figure 5.1. In Figure 5.1, red point indicates the current point of interest, blue points indicate the points inside the sphere with radius H, centred at the point of interest and gray points indicate the irrelevant points.

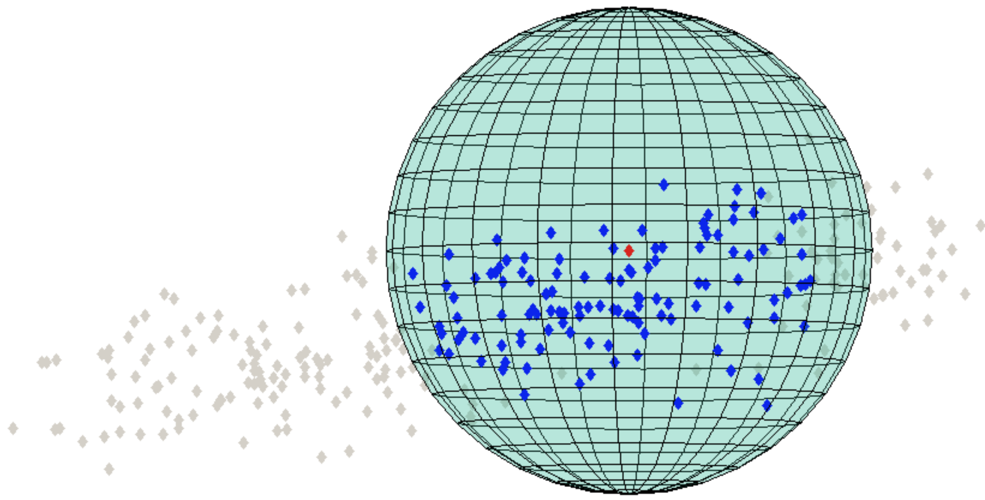

Figure 5.1: Selection of points in the neighbourhood of H. Red point is the point of interest, blue points are the selected points and cyan points are the remaining points in the point cloud.

On the second step of the iterative algorithm, a regression line is computed for the point of interest, using the points inside the sphere with radius H. Computation of 3-D regression line is explained in detail in the appendix of the [53] reference. Basically, mean values of the point indices are subtracted from the points such as given in Equation 5.5.

$$\tilde{x} = \underline{\hat{x}} - \sum \underline{x}, \qquad \tilde{y} = \underline{\hat{y}} - \sum \underline{y}, \qquad \tilde{z} = \underline{\hat{z}} - \sum \underline{z} \tag{5.5}$$

Then, the normalization condition matrix is expressed as Equation 5.6 is calculated.

$$\mathbf{N} = \begin{bmatrix} \sum \tilde{y}_i^2 + \tilde{z}_i^2 & -\sum \tilde{x}_i \tilde{y}_i & -\sum \tilde{x}_i \tilde{z}_i \\ -\sum \tilde{y}_i \tilde{x}_i & \sum \tilde{x}_i^2 + \tilde{z}_i^2 & -\sum \tilde{y}_i \tilde{z}_i \\ -\sum \tilde{z}_i \tilde{x}_i & -\sum \tilde{z}_i \tilde{y}_i & \sum \tilde{x}_i^2 + \tilde{y}_i^2 \end{bmatrix} \tag{5.6}$$

Then, eigenvalue decomposition is applied on the matrix. The eigenvectors are named as α_1, α_2 and α_3 in the increasing order to eigenvalues. The eigenvector corresponding to the smallest eigenvalue, α_1 is the regression line direction, whereas remaining two eigenvectors, α_2 and α_3, are the orthonormal vectors of the principal axis. Then, the points inside the sphere are projected on the plane defined with α_1 and α_2 vectors, using Equation 5.7.

$$A = [\alpha_1 \quad \alpha_2] \tag{5.7}$$

$$P = A^{-1} A^H A \tag{5.8}$$

$$[u \quad v] = P\,[\tilde{x} \quad \tilde{y} \quad \tilde{z}] \tag{5.9}$$

The projection procedure is presented in Figure 5.2. The red, blue and gray points indicates the point of interest, neighbours of the point of interest and irrelevant points respectively. The red, cyan and green arrows are the α_1, α_2 and α_3 vectors respectively. The point cloud is aligned along the red arrow.

Then, the algorithm will be identically repeated for $P1$ and $P2$ planes. In the first part of the algorithm, the points are projected on the $P1$ plane defined by red and cyan arrows. MLS algorithm will be applied to these projected points. In the second part of the algorithm, the points are projected on the $P2$ plane which is defined by red and green arrows. Again MLS algorithm will be applied to these projected points.

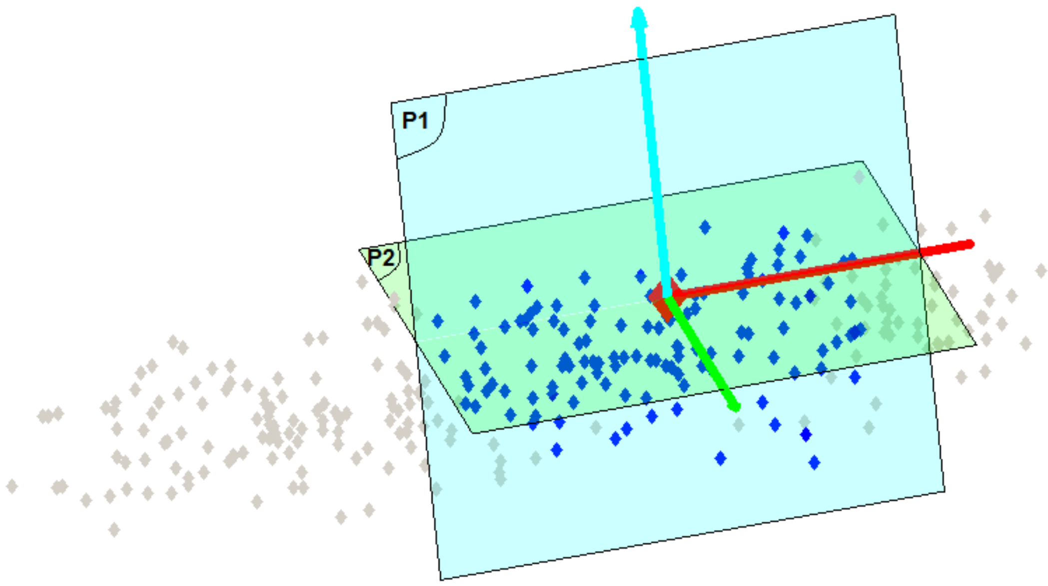

Figure 5.2: Projection of points onto the two orthogonal planes

After this projection, the dimension of the point cloud is reduced to 2. On the 2-D plane, the MLS algorithm is much easier to apply. On this plane, the local regression line is computed by minimizing the quadratic function in Equation 5.10. w is the weighing vector which is computed by Equation 5.11 inside the sphere, and has 0 values outside of the sphere. The weighing vector is presented in Figure 5.3, for H value of 20 cm.

$$[a,\ b] = \underset{a,b}{\operatorname{argmin}} \sum_{i}^{N} (au_i + b - v_i)^2\, w_i \tag{5.10}$$

$$w = 2\frac{r^3}{H^3} - 3\frac{r^2}{H^2} + 1, \quad r < H \tag{5.11}$$

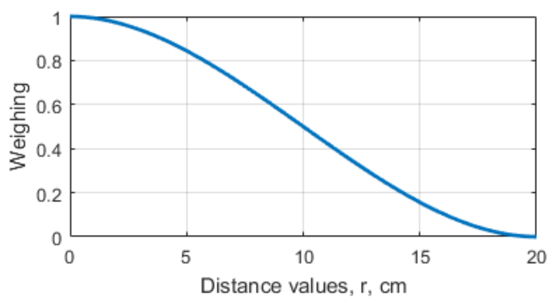

Figure 5.3: Weighing vector, w, for H value of 20

Using the quadratic minimization results of Equation 5.10, transformation matrix, $\mathbf{M}$ is generated as given in Equation 5.13; which is used to transform the points such that the regression line is parallel to the x axis. Also, the transformed value of the point of interest is subtracted from all points in order to make the point of interest is the new origin as given in Equation 5.15. The transformed point of interest is presented as $[\tilde{u}^* \quad \tilde{v}^*]$.

$$
\begin{aligned}
\theta &= -\tan^{-1}(a) && (5.12)\\
\mathbf{M} &= \begin{bmatrix} \cos(\theta) & \sin(\theta) \\ -\sin(\theta) & \cos(\theta) \end{bmatrix} && (5.13)\\
[\tilde{u} \quad \tilde{v}] &= [u \quad v]\ \mathbf{M} && (5.14)\\
[\tilde{u} \quad \tilde{v}] &= [\tilde{u} \quad \tilde{v}] - [\tilde{u}^* \quad \tilde{v}^*] && (5.15)
\end{aligned}
$$

After this transformation, the local quadratic regression curve is computed by minimizing the Equation 5.16. Projection of the transformed point onto the local quadratic regression curve is (0,c) point. Therefore this point is first inverse transformed and the origin shifting subtraction is reversed as Equation 5.17. Note that, MLS is applied on the plane defined by α_1, α_2 vectors. Therefore, the output of MLS algorithm, t vector does not have the required information along α_3 vector. The output of MLS algorithm is corrected with Equation 5.19. The point of interest is presented as t^* vector in Equation 5.18, in order to enhance the readability of the Equation 5.19. $\bullet$ operator is used for dot product.

$$
\begin{aligned}
[a,\ b,\ c] &= \operatorname*{argmin}_{a,b,c} \sum_{i}^{N} \left(a\tilde{u}^2 + b\tilde{u} + c - \tilde{v}\right)^2 w_i && (5.16)\\
t &= [\tilde{u}^* \quad c + \tilde{v}^*]\ \mathbf{M}^{-1}\ A^H && (5.17)\\
t^* &= [x(k)y(k)z(k)] && (5.18)\\
t^* &= t - \left((t^* A^{-1} A^H A A^H - t^*) \bullet \alpha_3\right)\alpha_3^T && (5.19)
\end{aligned}
$$

After this procedure, the original point of interest, $[x_k\ y_k\ z_k]$ is replaced with calculated MLS output, t^* with Equation 5.19. The MLS is applied on the plane defined by α_1, α_2. The whole procedure is repeated for the plane defined by α_1, α_3 by only replacing α_2 variable with α_3 in the expressions. The whole procedure is summarized in the flowchart in Figure 5.4.

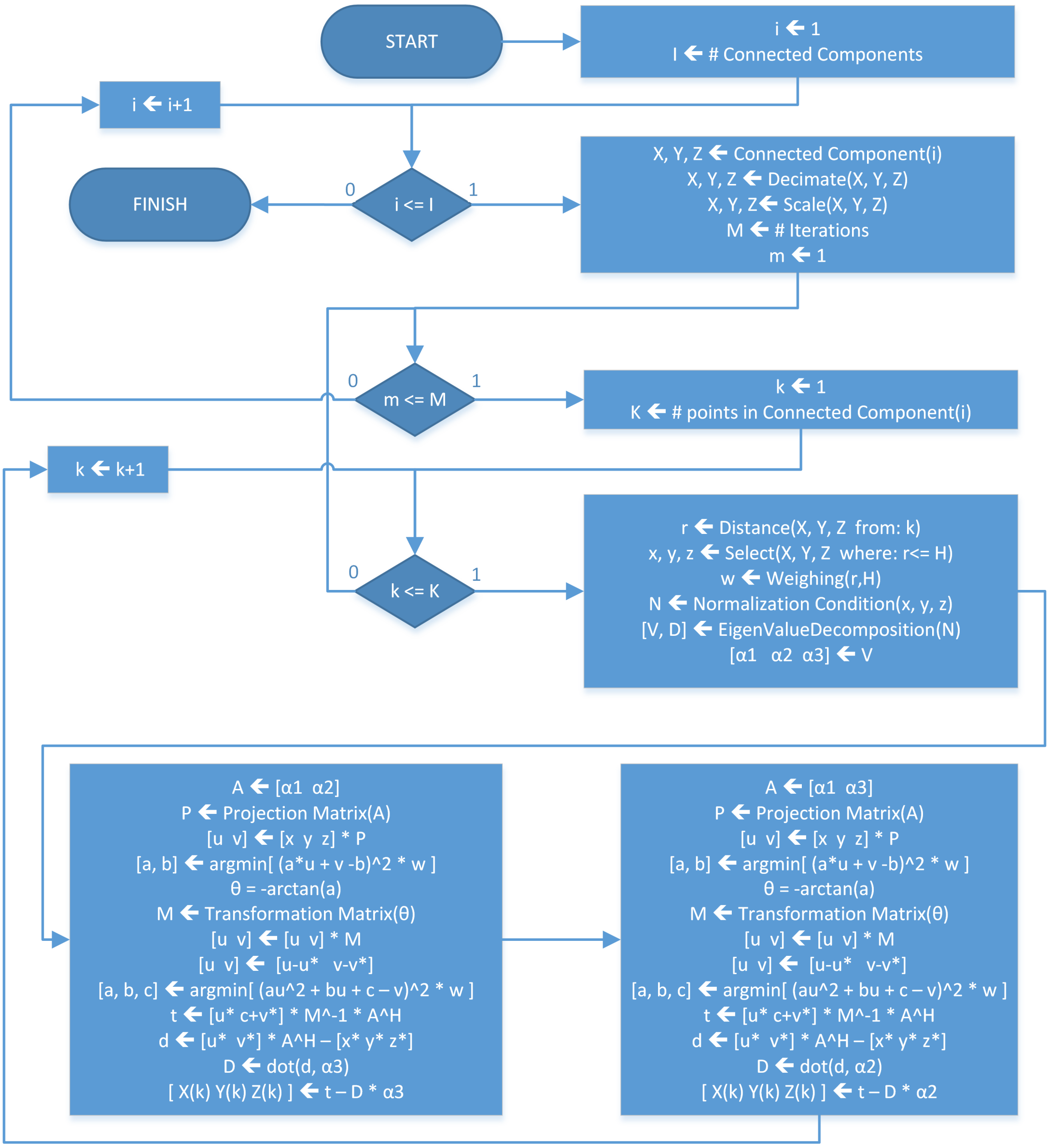

Figure 5.4: Flowchart of curve reconstruction algorithm

The results of curve reconstruction algorithm for two different H values are shown in Figure 5.5 and 5.6. Note that when H value is small, the curve reconstruction algorithm has failed and made multiple branches.

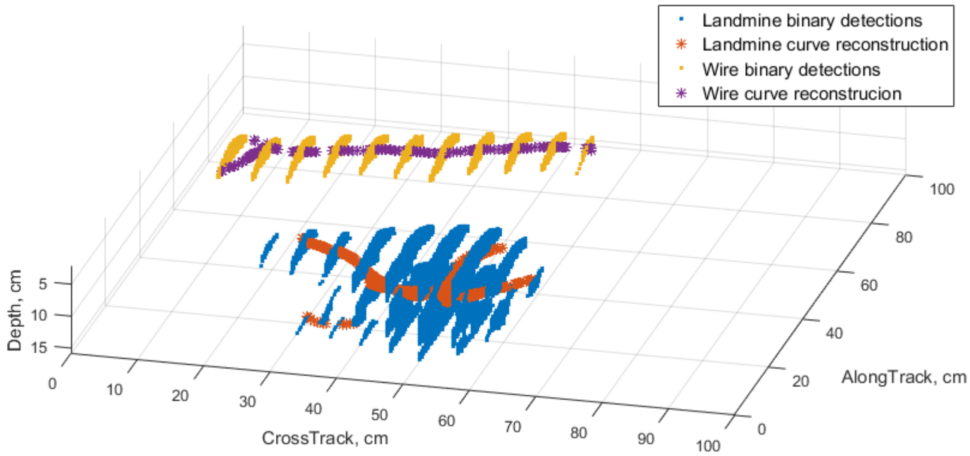

Figure 5.5: Output of the curve reconstruction algorithm with H = 10 cm.

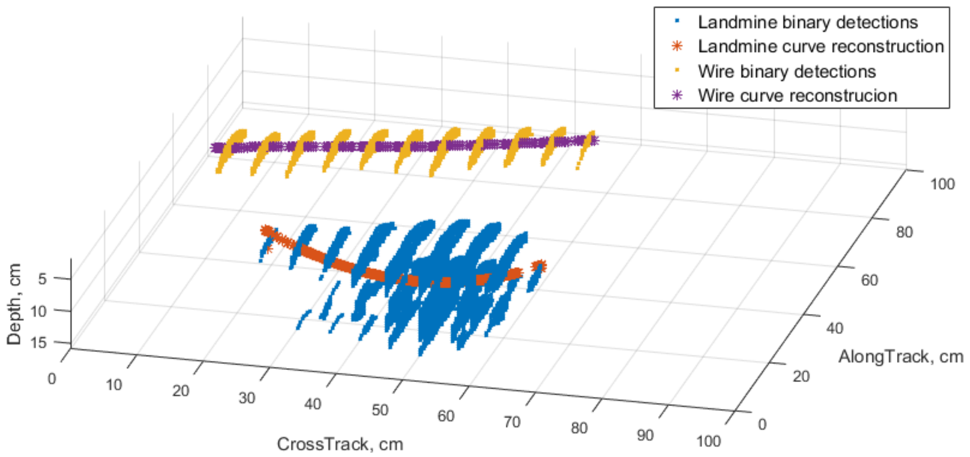

Figure 5.6: Output of the curve reconstruction algorithm with H = 30 cm.

5.2 Feature Extraction

The curve reconstruction algorithm is applied on all connected component groups. In order to classify these detection groups, some distinct features should be extracted. In [52], possible features that can be used for landmine classification are listed as area, energy and the spatial variations of these features. Since wire classification problem with GPR is not studied in the literature, there is not a baseline for feature selection methods. Therefore, selection of features are done intuitively. The possible features that would be useful to identify a wire from other clutter objects are determined as the mean and standard deviation of the distance from the reconstructed curve, mean prescreener strength, length of reconstructed curve and the total number of detections. The extraction methods of these features are explained below.

5.2.1 Mean and standard deviation of distance from curve

The 3-D curve of the wire is constructed previously using 3-D MLS curve reconstruction algorithm summarized in Figure 5.4. The detections can be considered as a point cloud scattered around the reconstructed curve. The minimum distance from each detection point to the reconstructed curve is calculated with Algorithm 10. x, y, z represents the indices of binary detections just obtained after Equation 5.1. X_n, Y_n, Z_n represents the output of 3-D curve reconstruction algorithm, as calculated in Equation 5.19.

Algorithm 10 Feature Extraction: Distance from the curve

for $\forall Connected\ Components$ **do**
  $K \leftarrow \text{length}(ConnectedComponent_i)$
  for $k = 1, \quad k <= K, \quad k++$ **do**
    $d(k) \leftarrow \underset{n}{\text{argmin}} \sqrt{(x(k) - X_n)^2 + (y(k) - Y_n)^2 + (z(k) - Z_n)^2}$
  end for
end for

The distance vector, d will have a distribution. The mean and variance of this distribution are valuable information that can be extracted from the vector. The distributions of the calculated dimension vectors for the landmine and the wire in the sample C-scan data (04th data on Appendix A) are presented in Figure 5.7.

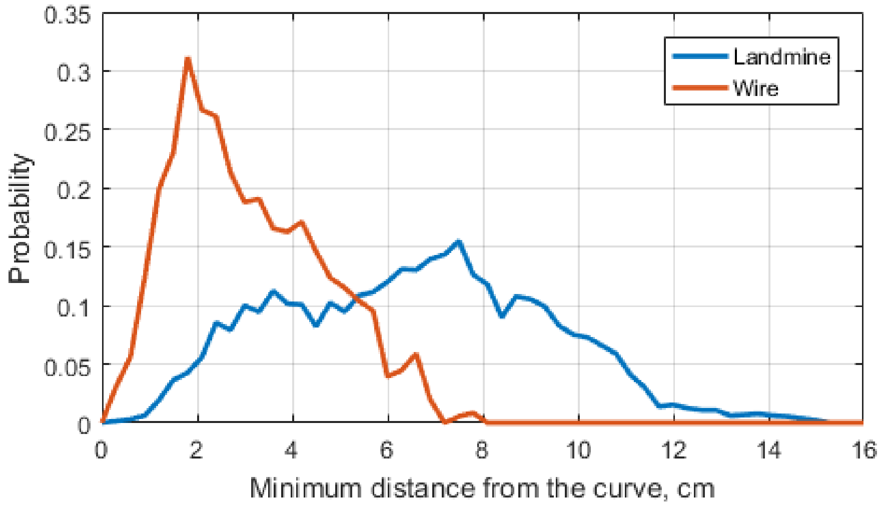

Figure 5.7: Histogram of the minimum distances from the curve for landmine object and wire object in the sample data (4th Data Appendix A)

Two features, mean (σ_1) and standard deviation (σ_2) are calculated as in Equation 5.20 and 5.21. d is the calculated distance vector, K ,s the length of distance vector.

$$\sigma_1 = \frac{1}{K}\sum_{i=1}^{K} d(i) \tag{5.20}$$

$$\sigma_2 = \sqrt{\frac{1}{K-1}\sum_{i=1}^{K} (d(i) - \sigma_1)^2} \tag{5.21}$$

5.2.2 Average Pre-screener Strength

So far, only the binary detections of pre-screener are used in curve reconstruction and feature extraction algorithm. However, the pre-screener strength also contains valuable information. For instance, wire reflections generally have small energy compared to massive metal objects, like landmines.

The average pre-screener strength is another feature that can be used in classification. The **T** matrix in Algorithm 8 is used for calculation. The feature is calculated for each connected component group as in Equation 5.22. Consider B is the set of indices for a given connected component group.

$$\sigma_3 = \sqrt{\sum_{i,j,k \in B} |\mathbf{T}(i,j,k)|^2} \tag{5.22}$$

5.2.3 Curve length

In order to calculate the length of the curve, first the line should be approximated with few samples as a spline curve. Otherwise, the points would be unorganized and the calculated length wouldn't result in the real length. The approximation is done as following;

First, a random point is selected as the starting point. Then, inside the neighbourhood of 1 cm distance the farthest point to the starting point is selected as the first point for one direction of the curve. The farthest point to the selected point inside the same neighbourhood will be the first point for the opposite direction. After the selection, the remaining points are cleared out. The procedure is repeated for both directions until all of the points for both directions are cleared out. The procedure is explained in Algorithm 11.

The points are organized by sequential process. Hence, calculation of length is very easy; it can be calculated by taking difference of the Q vector of length N, taking the norm to calculate the distance from differentiated X, Y and Z values. The sum of the norms will result in the total length of the curve as given in Equation 5.23. The length of the curve, σ_4, is the forth feature that will be used in classification.

$$\sigma_4 = \sum_{i=1}^{N-1} \|Q(i+1) - Q(i)\| \tag{5.23}$$

Algorithm 11 Approximation of curve with few samples

for $\forall Connected\ Components$ **do**
  $T(k) \leftarrow [X(k)\ Y(k)\ Z(k)]$: List of all points
  $t_s \leftarrow T(1)$: The starting point
  $r(k) \leftarrow \|T(k) - T(1)\|$: The distance vector from starting point
  $B \leftarrow r(k) < 5$: The set of indices inside 5 cm sphere
  $P \leftarrow T(k),\ k \in B$: The points inside 5 cm sphere
  $T \leftarrow T(k),\ k \notin B$: The points outside of 5 cm sphere
  $n \leftarrow \operatorname*{argmax}_{n \in B} r(n)$: The farthest point inside 5 cm sphere
  $t_1 \leftarrow P(n)$: The first point in one direction
  $r(k) \leftarrow \|P(k) - t_1\|$: The distance vector from first point
  $n \leftarrow \operatorname*{argmax}_{n} r(k)$: The farthest point inside 5 cm sphere to first point
  $t_2 \leftarrow P(n)$: The first point in opposite direction
  $Q \leftarrow \left[t_1^T\ t_s^T\ t_2^T\right]^T$: The queue vector
  do
    $r(k) \leftarrow \|T(k) - t_1\|$: Distance vector from first point
    $B \leftarrow r(k) < 1$: The set of indices inside 5 cm sphere
    $T \leftarrow T(k),\ k \notin B$: The points outside of 5 cm sphere
    $n \leftarrow \operatorname*{argmax}_{n \in B} r(n)$: The farthest point
    $t_1 \leftarrow P(n)$: The continuing point in the first direction
    $Q \leftarrow \left[t_1^T\ Q^T\right]^T$: Updated queue vector
  while $B \neq \varnothing$
  do
    $r(k) \leftarrow \|T(k) - t_2\|$: Distance vector from second point
    $B \leftarrow r(k) < 1$: The set of indices inside 5 cm sphere
    $T \leftarrow T(k),\ k \notin B$: The points outside of 5 cm sphere
    $n \leftarrow \operatorname*{argmax}_{n \in B} r(n)$: The farthest point
    $t_2 \leftarrow P(n)$: The continuing point in the opposite direction
    $Q \leftarrow \left[Q^T\ t_2^T\right]^T$: Updated queue vector
  while $B \neq \varnothing$
end for

5.2.4 Total Number of Binary Detections

The last feature that is covered in the thesis is the total number of binary detections for each connected component group, which can be basically expressed as $\sigma_5 = N$, where N is the total number of elements inside a connected component group.

5.3 Classification

Classification problem is well studied in the GPR literature. They commonly focus on landmine and UXO classification as studied in [56], [57], [3], [58], [31] and so on. However, wire classification is not studied well in the GPR literature.

There is a large number of classification methods in the literature. In this thesis, a simple two-class classifier is sufficient, since only wire objects will be classified using 5 features. SVM (support vector machine) is a well-known and well-studied method and it fits the wire classification problem with 2 classes. Therefore, SVM is selected as the classification method in the thesis.

5.3.1 Support Vector Machine

SVM is a supervised classification algorithm that tries to find a hyperplane separating two classes; while minimizing the risk. Support vectors are the most informative and hardest to classify points in the feature space. Support vectors are used to define the plane that separates two classes.

SVM classification is based on two steps; training and classifying. The dual problem is formulated as the optimization problem given in Equation 5.24. For the training set, total number of N features vectors, x_i, are extracted for each detection group. Then, the labels, y_i, are defined as +1 (wire class) and -1 (other class) for each x_i feature vectors.

$$
\begin{aligned}
&\underset{\alpha}{\text{maximize}} \quad \sum_i \alpha_i - \frac{1}{2}\sum_{j,k} \alpha_j \alpha_k y_j y_k \kappa(x_j, x_k) \\
&\text{subject to} \quad 0 \leq \alpha_i \leq C, \quad \sum_i \alpha_i y_i = 0
\end{aligned}
\tag{5.24}
$$

The α vector is learnt and C is a non-negative regularization parameter. $\kappa(x_j, x_k)$ is the kernel function. Gaussian Radial Basis Function (RBF) kernel is used in this thesis and it's expressed as in Equation 5.25, where σ is the sigma parameter of the Gaussian RBF kernel. The σ value can be optimized, when needed. However, in this thesis, it is not optimized since the sample size (the C-scan simulations in Appendix A) is small and optimization of σ may lead to false conclusions. Therefore, σ value is kept constant as 1.

$$
\kappa(x_j, x_k) = \exp\left(-\frac{\|x_j - x_k\|^2}{2\sigma^2}\right) \tag{5.25}
$$

A liner kernel could be used as well, instead of Gaussian RBF Kernel. Linear kernel is expressed as in Equation 5.26.

$$
\kappa(x_j, x_k) = x_j^T x_k \tag{5.26}
$$

After training, a test data, z is classified using the Equation 5.27. In this equation, α_i values can be zero for some i index. For the i indices such that α_i is non zero, the x_i vectors are called "support vectors" and b is the bias of the hyperplane.

$$
f(z) = \sum_i^N \alpha_i y_i \kappa(x_i, z) + b \tag{5.27}
$$

There exist also multi-class SVM methods; which actually consider multiple SVM classifiers, all of them classifies a class considering "one versus one" or "one versus all" strategies. At the end, the results of these classifiers are combined and multi class results are obtained. However, in wire detection problem, there only exist two classes; wire and others. Therefore, use of a multi-class method is not necessary in this concept.

The feature vectors, x_i, for each connected component group will be consisting of 5 features; mean and standard deviation of the distances from the constructed curve, average pre-screener strength, length of the curve and total number of binary detections. In order to train the SVM, first the feature vectors are labelled using the method which will be explained under "Evaluation of the Performance of Algorithm" section below. Using these labels, 70 percent of the feature vectors for both wire class and other class are used for training the SVM. Then, the remaining 30 percent wire and other classes are used for testing the trained classifier.

5.4 Evaluation of the Performance

The algorithm chain is explained in detail in the previous sections. The unprocessed raw GPR data at different along-track and cross-track positions are collected. Then, time clipping and median filtering is applied on the data to remove ground bounce and reduce the clutter level. Logarithmic depth weighing is applied along depth direction in order to equalize the signal levels coming from different depths. 2-D LMS filtering is applied for each depth bin separately to suppress the background and amplify the foreground. Mathematical morphologies are used for enhancing the performance of the prescreening algorithm. 3-D Curve reconstruction with MLS algorithm is applied to the detections before the feature extraction. Using this reconstructed curve, length of the curve is calculated and mean and standard deviation of the distances between curve and point cloud is derived. Also, volume of the point cloud is estimated using number of points in the cloud. The mean pre-screener strength is another feature that is derived from the detection group. Later, SVM classifier with Gaussian RBF kernel is used for classification problem.

5.4.1 Labelling method

The performance of the algorithm chain is evaluated with the classifier outputs. The curve reconstruction algorithm gives the down-sampled 3-D curve, and this data is stored. The true locations of the wires are also stored using the simulation input files. Then, the labelling of detections is performed by Algorithm 12. The TH_d is the distance threshold, set to 10 cm empirically. Use of too larger distance threshold results in false positive labelling. Use of too small distance threshold results in misses. The range of 5 cm to 15 cm was found suitable for wire detection problem. $TH_{\%}$ is the percentage threshold set to 0.70 empirically. It has been observed that in Appendix A, the IEDs connected to wires are detected as connected to the wire. Therefore, this threshold is decreased to 70%. When the single wire simulations are analysed, it has been seen that the $TH_{\%}$ value can be increased up to 95% levels, without any missing wires.

The labelling is done with top-down looking 2-D locations in XY plane, since the position in Z axis depends on local electromagnetic properties of the soil and cannot be trusted for labelling.

Algorithm 12 Automatic labelling of curves for supervised learning

for $k = \textit{All Detection Groups}$ **do**
    for $m = \textit{All Wires In Simulation}$ **do**
        $d \leftarrow$ distance($from$: Reconstructed Curve, to : Real Wire)
        if (number($d < TH_d$) / length(d)) $>$ $TH_{\%}$ **then**
            $Class(k) \leftarrow 1$
            $WireID(k) \leftarrow m$
        else
            $Class(k) \leftarrow -1$
            $WireID(k) \leftarrow 0$
        end if
    end for
end for

For instance, consider the C-scan data of number 13, given in Appendix A.

The real input geometry of the wire and the reconstructed curve locations in XY plane are presented in Figure 5.8. The reconstructed curve nearly perfectly matches with the input file geometry. The minimum distances from the reconstructed curve to the input file geometry is below 1.5 cm for 95 percent of the curve.

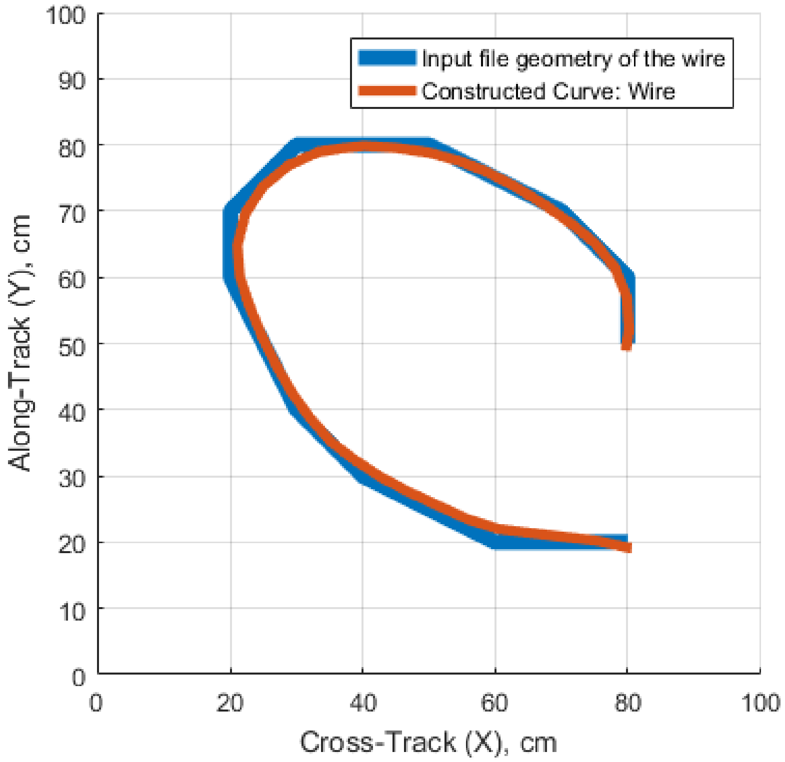

Figure 5.8: Real input geometry and curve reconstruction output of C-scan Data 13 (Appendix A)

Another case is investigated for the sample data used in Chapter 4 and Chapter 5, which is the Test number 04 in the Appendix A. The real input geometry of the wire and the reconstructed curve locations in XY plane are presented in Figure 5.9. In this case, there is a landmine and a wire, where wire starts from the boundary of the simulation environment and ends in the middle of the medium. The wire is detected starting from 10 cm in X direction; which corresponds to the location T/R pair 1. In this data, again, the majority of the reconstructed curve lays within the input file geometry, and therefore labelled as wire. The curve reconstructed from the landmine is considerable farther than the real location of the wire and therefore classified as not wire.

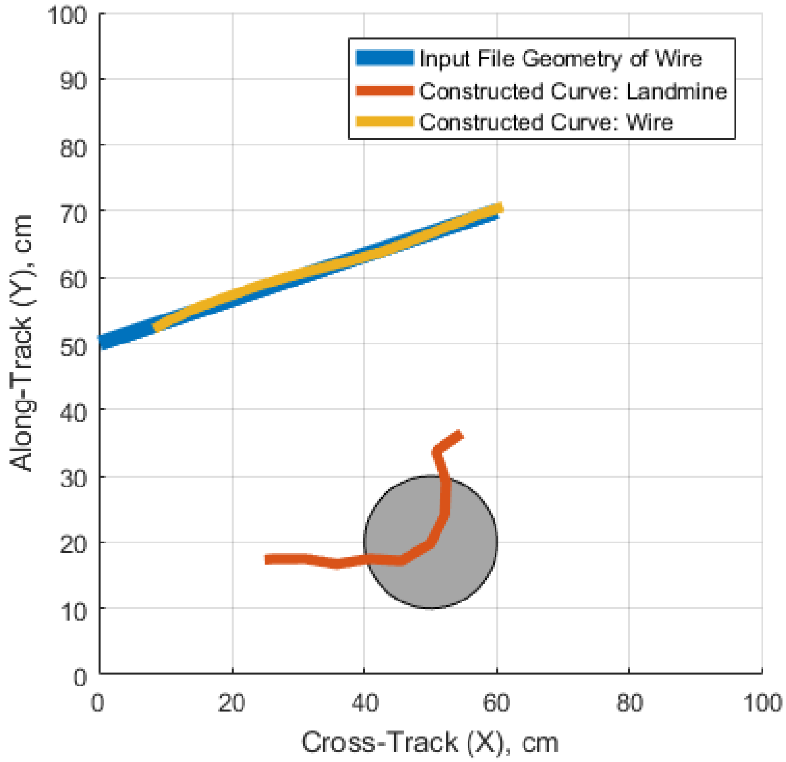

Figure 5.9: Real input geometry and curve reconstruction output of C-scan Data 04 (Appendix A)

The last case investigated is the C-scan Test Number 27 of the Appendix A. In this scenario, wire is in contact with a plastic object; which is modelled as a sample IED device. The detections coming from the plastic object also mixes with the wire detections, and therefore reconstructed curve goes farther than the actual point the wire ends. In this case, again, the curve should be labelled as a wire. Although reconstructed curve fits the input file geometry mostly, the minimum distances increase up to 20 cm at the farthest point of reconstructed curve at IED side. Therefore, a threshold to the percentage value is defined for labelling the curves, which is given as $TH_{\%}$ in Algorithm 12.

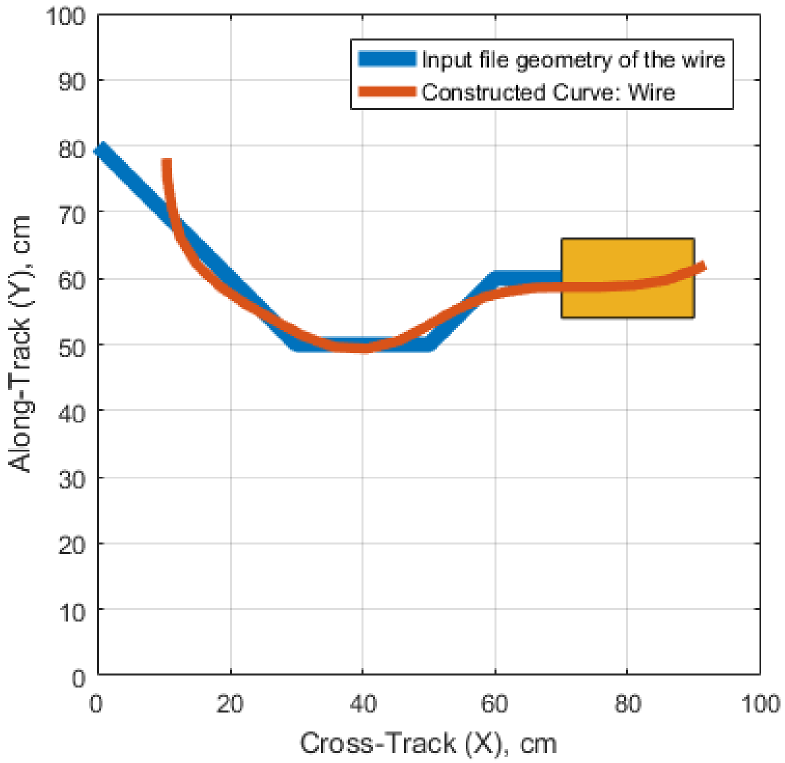

Figure 5.10: Real input geometry and curve reconstruction output of C-scan Data 27 (Appendix A)

5.4.2 Performance Metrics of Classifiers

The performance of the prescreening algorithms were evaluated for changing detection thresholds of the prescreener in Algorithm 8 and presented in Figure 4.15, 4.16, 4.17 and 4.18 previously. The performance of the classifier is evaluated at a single detection threshold, where the probability of detection is high and probability of false alarm is relatively smaller.

The reason behind this can be explained as following. For small values of detection threshold, the detections coming from clutter objects collide with wire detections. In this case, curve reconstruction algorithm falsely reconstructs curves. In some cases, the reconstructed curve is not labelled as wire, since it has considerably drifted away from the real wire position. Moreover, the clutter features merge with wire features. As a result, the classification become meaningless for small values of detection threshold. For high values of detection threshold, on the other hand, some wires are not detected. As a consequence, the overall detection and classification performance of the proposed system decreases.

Hence, the classification performance is evaluated at a single detection threshold, at the value of 0.11, which has resulted in best overall detection performance for the system empirically.

5.4.2.1 Confusion matrix

Confusion matrices are useful tables that are commonly used to measure the performance of decision algorithms. In confusion matrices, rows present the real case and columns present the result of decisions [59]. A sample matrix , $\mathbf{C}$, is presented in Table 5.1.

<table>
<tr><td></td><td></td><td colspan="2">Observation</td></tr>
<tr><td></td><td></td><td>Wire</td><td>Clutter</td></tr>
<tr><td rowspan="2">Real</td><td>Wire</td><td>A</td><td>B</td></tr>
<tr><td>Clutter</td><td>C</td><td>D</td></tr>
</table>

Table5.1: A sample confusion matrix

In the sample confusion matrix, Table 5.1, there is $A + B$ wire detections and $C + D$ clutter detections in reality. The classifier has classified A wires correctly; which yields to true positives. However, B wires are misclassified as clutter, these are false negatives. The classier has correctly classified D clutter objects; which are true negatives. However, C clutter objects are misclassified as wires, and these are false positives.

5.4.2.2 Precision

Precision of a class is the ratio of the true classifications to the total number of real points [59]. It can be formulated for two classes as Equation 5.28, where $\mathbf{C}$ is the confusion matrix and i is the class number. For instance, precision of wire class in Table 5.1 is $\frac{A}{A+B}$ and precision of clutter is $\frac{D}{D+C}$.

$$P(i) = \frac{\mathbf{C}(i,i)}{\mathbf{C}(1,i) + \mathbf{C}(2,i)} \tag{5.28}$$

5.4.2.3 Recall

Recall of a class if the ratio of true classifications to the total number of predictions for this class [59]. It can be formulated for two classes as Equation 5.29. For instance, recall of wire class in Table 5.1 is $\frac{A}{A+C}$ and recall of clutter is $\frac{D}{D+B}$.

$$R(i) = \frac{\mathbf{C}(i,i)}{\mathbf{C}(i,1) + \mathbf{C}(i,2)} \tag{5.29}$$

5.4.2.4 Accuracy

Accuracy is the total number of true classifications to the total number of instances for a classifier [59]. It can be formulated as Equation 5.30.

$$A = \frac{\mathbf{C}(1,1) + \mathbf{C}(2,2)}{\mathbf{C}(1,1) + \mathbf{C}(1,2) + \mathbf{C}(1,2) + \mathbf{C}(2,2)} \tag{5.30}$$

5.4.3 Performance of Utilized Algorithm Chain

The detection threshold of 0.11 is selected for evaluation of the classifier; where the prescreener achieved the detection rate of 91%, with the false alarm rate of 25%. For smaller values of detection threshold, false alarms collide with detections which distorts the performance of classification. For higher values of detection threshold, the number of detected wires decrease. Using the feature sets obtained from the analysis, 100000 Monte Carlo simulations are performed with the method described earlier. The classification performance of the simulation is presented in Table 5.2.

		Observation	
		Wire	Clutter
Real	Wire	50.67	4.33
	Clutter	3.98	52.02

Table5.2: Confusion matrix for Gaussian RBF Kernel SVM Classifier with prescreener detection threshold value of 0.11

The mean precision, recall and accuracy and their standard deviations for the threshold value of 0.11 are calculated and presented in Table 5.3. The same metrics are obtained for linear kernel SVM classifier as well. The metrics are presented in Table 5.4.

	Wire	Clutter
Precision	92.13%	92.90%
σ_p	5.24%	2.55%
Recall	92.82%	92.53%
σ_r	2.28%	3.51%
Accuracy	92.52%	
σ_a	2.40%	

Table5.3: Precision, Recall and Accuracy of Gaussian RBF kernel SVM Classifier with prescreener detection threshold value of 0.11

	Wire	Clutter
Precision	92.43%	91.38%
σ_p	11.62%	3.36%
Recall	91.64%	93.37%
σ_r	2.98%	6.59%
Accuracy	91.90%	
σ_a	4.94%	

Table5.4: Precision, Recall and Accuracy of linear kernel SVM Classifier with prescreener detection threshold value of 0.11

The performance metrics given in Table 5.3 provide valuable information. It has been seen that, for Gaussian RBF Kernel SVM, precision and accuracy of both classes and the accuracy of the classifier is all around the 92% levels. The standard deviation of wire precision is considerably high compared to standard deviations. Since the sample size, the number of C-scans in Appendix A, is considerably small for evaluating the performance of classification algorithm, the standard deviations are expected to be large.

Use of linear kernel has resulted in increased standard deviations; especially for wire precision. Yet, the results have shown that the wire and clutter classes can be considered linearly separable. A simple linear hyperplane can separate two classes with overall accuracy of 91.9%.

There are 64 wires in total. The 30th and 35th simulations are having two wires connected to an IED, and they are generally detected as connected to each other. In Figure 4.15, it has been seen that the 59 wires of 64 in total are detected successfully after prescreening step at threshold value of 0.11. If the wires connected to the same IED device is counted as one, it can be said that 57 wires are successfully detected after prescreening, out of 62 wires in total.

For the threshold value of 0.11, after curve reconstruction algorithm, 55 wires are successfully labelled as wire. However, the reconstructed curves for remaining 2 wires are not matching with the real wire positions, due to the collisions of wire detections with clutter objects. Therefore, they are labelled as clutter, but did not used for training of classifier in order to avoid false training. For Gaussian RBF Kernel SVM, the true classification rate of the classifier, in other words the precision of wire class, for the given threshold is calculated as 92.13%. The overall true positive detection rate of the proposed system is found as 81.73%, which is calculated by the dividing the true positive rate to the number of real wires. Moreover, the overall false alarm rate is found as 0.0663 false alarms per meter square. It is calculated by dividing false positive rate to the total searching area.

CHAPTER 6

CONCLUSION AND FUTURE WORK

6.1 Summary

In this thesis, detection of buried command wires that are used for IED detonation is investigated using ground penetrating radars. Ground penetrating radars are used extensively for explosive detection buried underground; yet there was a few studies focusing on wire detection problem using ground penetrating radars. The existing studies were focusing on the antenna and hardware design of GPRs, and there was not a study focusing on the preprocessing and classification part of the GPRs for wire detection problem. Moreover, most of these studies were investigating unburied wires. There was a lack in detection of the buried wires; and hence, detection of buried wires is studied in this thesis.

In Chapter 1, the concept of humanitarian demining is explained in detail. Then, the sensor types and methods used for buried explosive detection is explained. After this, the studies focusing on or related with wire detection problem is investigated. Then, the scope and outline of the thesis are presented.

In Chapter 2, the problem definition is given. Moreover, the basics of ground penetrating radars are briefly explained.

In Chapter 3, the simulation environment is described. A set of simulations is generated by changing few simulation parameters to see the effects of these specific changes. It has been observed identification of wires is not possible by looking at a single B-scan. Therefore, a set of C-scan simulations are prepared to test and evaluate the 3-D GPR signal processing and classification methods that are explained in Chapter 4 and 5.

In Chapter 4, the signal preprocessing methods are discussed under three sections. In the first section, time clipping, mean subtraction, median subtraction, principal component analysis are investigated for ground bounce and mutual coupling removal. In second section, depth whitening and logarithmic weighing are investigated for depth weighing. In the last section, LMS, RPCA and morphologically improved LMS are investigated for prescreening. Performance of the algorithms is presented afterwards.

It has been observed that, median filtering and time clipping is a simple yet very effective method for ground bounce and mutual coupling removal for the simulated data. A logarithmic scaling vector is proposed for depth weighing, which have resulted in better equalization along depth compared to method in the literature. The proposed prescreener, the morphologically improved 2-D LMS, has shown improvements compared to the methods in the literature. Although, detections coming from landmines, IEDs and rocks are labelled as false alarm, the proposed prescreener has achieved 90% of probability of wire detection with 16% false alarm rate. The area under the ROC curve of the preprocessing algorithms is measured as 0.9086.

In Chapter 5, the feature extraction and classification concept is investigated under three sections. In the first section, SVD line constructor and 3-D MLS curve reconstruction algorithms are investigated for curve reconstruction algorithms. In the second section, feature vectors are extracted. In the last section, SVM classifier is studied for classification. Performance of the algorithms is presented afterwards.

The 3-D curve reconstruction with MLS algorithm is utilized before feature extraction. It has been seen that, it can reconstruct 3-D curves of wires placed free form in the space. However, the algorithm cannot be considered as robust against the clutter collisions. It has been seen that the curve reconstruction algorithm has incorrectly reconstructed curves for small values of detection threshold, due to the clutter collisions; which results in decreased classification performance. Using the free-form 3-D curve, novel 3-D feature sets are extracted. SVM classifier with Gaussian Kernel is used for the feature based classification. SVM is trained and tested using different samples obtained from the simulations; and this process is repeated for several Monte Carlo runs to evaluate the performance of classifier. For an empirically found best resulting threshold value, the precision and recall of both wires and clutter and the total accuracy of the classifier was found roughly 92%. Combining with the detection performance of preprocessing methods, it has been observed that the true detection and classification rate of the real wires was 81%.

6.2 Conclusion

The aim of this thesis is to detect and identify the buried wires with ground penetrating radars which is a challenging problem because of its nature.

It has been seen that identification of wires using B-scan is nearly impossible; since the wire reflections have small amplitudes and the hyperbola signature highly depends on the orientation of the wire and the polarization of the antenna.

Therefore, C-scan data is utilized for wire detection problem. The continuity of detections in 3-D, forming a thin and long point cloud is the distinctive characteristics of wires, different than any other type of clutter.

3-D signal processing algorithms are proposed for the preprocessing of GPR data. Morphologically improved 2-D LMS filtering is proposed to decrease the number of false alarms. Preprocessing algorithms have achieved the area under the ROC curve of 0.9086. Using the 3-D curve reconstruction algorithm, the features that are useful to describe the thin and long structure of the wire are extracted. Gaussian RBF Kernel SVM has been utilized for the problem; however use of linear kernel in SVM classifier has also resulted in a good performance. Therefore, wire and clutter classification problem with described feature set can be considered as linearly separable.

In the end, the overall algorithm chain has achieved 81% wire detection and classification rate while having false alarm rate of 0.067 false alarms per meter square. It has shown that detection and identification of wires of 2 mm radius, buried 1 to 14 cm deep into the ground is possible with high probability of detection and low false alarm rate.

However, the performance of the proposed algorithms highly depends on the hardware design of the GPR. Detection performance of the wires placed perpendicular to the antenna polarization was considerably low; therefore dual polarization or circular polarization systems should be developed for buried wire detection. Gaussian derivative waveform at 2.5 GHz center frequency is used in the simulations; which occupies -20dB bandwidth starting from 150 MHz and goes until 7 GHz. Use of smaller center frequencies resulted in decreased amplitudes. The spatial resolution of the C-scan data was 1 cm in along-track dimension and 5 cm in cross-track dimension. The temporal resolution was about 4 picoseconds. Use of worse temporal and spatial resolutions may result in decreased performance.

6.3 Future Work

There are few future works related with this study. Real measurements from a high resolution GPR that is capable of utilizing different polarizations (x, y, dual, circular) should be collected and the performance of the proposed methods should be investigated with real data. The computational power needs of algorithms was a concern in the whole thesis. However, curve reconstruction algorithm for instance, can be improved to match with computational capabilities of real systems. The improvements proposed on 2D LMS requires the whole C-scan block. It should be improved such that the algorithm can run each time the vehicle moves. The curve reconstruction algorithm should be improved with a protection mechanism regarding the collided hyperbolas from different targets. Moreover, ground bounce peak tracking algorithm and calculation of logarithmic depth weighing value can be made adaptive. Lastly, multi-class SVM classifier can be studied for classification of command wires together with other objects such as land mines, UXOs and IEDs.

REFERENCES

[1] B. Scheers, "Ultra-wideband ground penetrating radar with application to the detection of anti personnel landmines," Ph.D. dissertation, Royal Military Academy, 2001.

[2] D. Daniels, *Unexploded Ordnance Detection and Mitigation.* Springer Netherlands, 2009, ch. Ground Penetrating Radar for Buried Landmine and IED Detection, pp. 89–111.

[3] X. Nunez-Nieto, M. Solla, P. Gomez-Perez, and H. Lorenzo, "Gpr signal characterization for automated landmine and uxo detection based on machine learning techniques," *Remote Sens*, vol. 6, no. 10, pp. 9729–9748, 2014.

[4] M. O'Hara, "Detection of ied enhancement in urban environments," Ph.D. dissertation, Naval Postgraduate School, Monterey, California, 2009.

[5] UNIDIR, "Addressing improvised explosive devices, options and opportunities to better utilize un processes and actors," UNIDIR, United Nations Institute for Disarmament Research, Tech. Rep., 2015. [Online]. Available: http://www.unidir.org/files/publications/pdfs/-en-641.pdf

[6] K. Furuta and J. Ishikawa, Eds., *Anti-personnel Landmine Detection for Humanitarian Demining.* Springer, 2009.

[7] *Guidebook on Detection Technologies and Systems for Humanitarian Demining*, Geneva International Centre for Humanitarian Demining (GICHD), 2006.

[8] S. E. Yuksel, G. Bozdagi Akar, and S. Ozturk, "Fusion of forward-looking infrared camera and down-looking ground penetrating radar for buried target detection," in *Detection and Sensing of Mines Explosive Objects and Obscured Targets XX*, vol. 9454. SPIE, 2015.

[9] M. Bold, "Mine detection rats, efficiency and effectiveness study using mdr capability," Geneva International Centre for Humanitarian Demining (GICHD), Tech. Rep., August 2016.

[10] M. P. Masarik, J. Burns, B. T. Thelen, J. Kelly, and T. C. Havens, "Enhanced buried uxo detection via gpr/emi data fusion," in *Proceedings of*

Detection and Sensing of Mines, Explosive Objects, and Obscured Targets XXI, vol. 9823. SPIE, 2016.

[11] H. Frigui, L. Zhang, and P. Gader, "Context dependent multi-sensor fusion for landmine detection," in *Geoscience and Remote Sensing Symposium 2008*, 2008.

[12] E. V. McDonald and T. Bullard, Eds., *Military Geosciences and Desert Warfare: Past lessons and Modern Challenges.* Springer, 2016.

[13] H. Liu, J. Zhao, and M. Sato, "A hybrid dual-polarization gpr system for detection of linear objects," *IEEE Antennas and Wireless Propagation Letters*, vol. 14, pp. 317–320, 2015.

[14] C. L. Yeo, "Command wire sensor measurements," Master's thesis, Naval Postgraduate School, Monterey, California, 2012.

[15] J. T. Apostolos and R. J. Millard, "Method and apparatus for detecting command wire utilized to detonate an improvised explosive device (ied)," Jun. 2 2011, uS Patent App. 12/628,359. [Online]. Available: https://www.google.com/patents/US20110128149

[16] A. Heinzel, M. Peichl, E. Schreiber, S. Dill, and F. Bischeltsrieder, "Investigations on the detection of thin wires using mimo sar," in *Proceedings of Detection and Sensing of Mines, Explosive Objects, and Obscured Targets XXII.* SPIE, April 2017.

[17] S. H. Ni, Y. H. Huang, K. F. Lo, and D. C. Lin, "Buried pipe detection by ground penetrating radar using the discrete wavelet transform," *Computer and Geotechnics*, vol. 37, no. 4, pp. 440–448, June 2010.

[18] P. Gamba and S. Lossani, "Neural detection of pipe signatures in ground penetrating radar images," *IEEE Transactions on Geoscience and Remote Sensing*, vol. 38, no. 2, pp. 790–797, March 2000.

[19] H. G. Poley, "Gpr antennas design and experimental evaluation," Master's thesis, Delft University of Technology, 2010.

[20] M. Sato, *Anti-personnel Landmine Detection for Humanitarian Demining: The Current Situation and Future Direction for Japanese Research and Development.* Springer Science and Business Media, 2009, ch. Principles of Mine Detection by Ground-penetrating Radar.

[21] D. J. Daniels, *Ground Penetrating Radar*, ser. Electromagnetics and Radar Series. Institution of Engineering and Technology, 2004.

[22] C. Warren, A. Giannopoulos, and I. Giannakis, "gprmax: Open source software to simulate electromagnetic wave propagation for ground penetrating radar," *Computer Physics Communications*, vol. 209, pp. 163–170, 2016.

[23] [Online]. Available: http://www.gprmax.com/publications.shtml

[24] I. Giannakis, A. Giannopoulos, and C. Warren, "A realistic fdtd numerical modeling framework of ground penetrating radar for landmine detection," *IEEE Journal of Selected Topics in Applied Earth Observations and Remote Sensing*, vol. 9, no. 1, pp. 37–51, 2016.

[25] K. Yee, "Numerical solution of initial boundary value problems involving maxwell's equations in isotropic media," *IEEE Transactions on Antennas and Propagation*, vol. 14, no. 3, pp. 302–307, 1966.

[26] N. R. Peplinski, F. T. Ulaby, and D. M. C, "Dielectric properties of soils in the 0.3 - 1.3 ghz range," *IEEE Transactions on Geoscience and Remote Sensing*, vol. 33, no. 3, pp. 803–807, May 1995.

[27] M. I. Skolnik, *Introduction to Radar Systems.* Tata McGraw Hill, 2001.

[28] P. A. Torrione, C. S. Throckmorton, and L. M. Collins, "Performance of an adaptive feature based processor for a wideband ground penetrating radar system," *IEEE Transactions on Aerospace and Electronic Systems*, vol. 42, no. 2, p. 644, April 2006.

[29] L. Mertens, R. Persico, L. Matera, and S. Lambot, "Automated detection of reflection hyperbolas in complex gpr images with no a priori knowledge on the medium," *IEEE Transactions on Geoscience and Remote Sensing*, vol. 54, no. 1, pp. 580–596, Jan 2016.

[30] Q. Dou, L. Wei, D. R. Magee, and A. G. Cohn, "Real-time hyperbola recognition and fitting in gpr data," *IEEE Transactions on Geoscience and Remote Sensing*, vol. 55, no. 1, pp. 51–62, Jan 2017.

[31] P. Gader, W. H. Lee, and J. N. Wilson, "Detecting landmines with ground-penetrating radar using feature-based rules, order statistics, and adaptive whitening," *IEEE Transactions on Geoscience and Remote Sensing*, vol. 42, no. 11, p. 2522, November 2004.

[32] F. Lombardi, H. D. Griffiths, and M. Lualdi, "The influence of spatial sampling in gpr surveys for the detection of landmines and ieds," in *Proceedings of the 13th European Radar Conferance (EuRAD)*, October 2016, pp. 322–325.

[33] R. Solimene, A. Cuccaro, A. Dell'Aversano, I. Catapano, and F. Soldovieri, "Ground clutter removal in gpr surveys," *IEEE Journal of Selected Topics in Applied Earth Observations and Remote Sensing*, vol. 7, no. 3, pp. 792–798, March 20014.

[34] P. T. W. Wong, W. W. L. Lai, and M. Sato, "Time-frequency spectral analysis of stepped frequency continuous wave and impulse ground penetrating radar," in *Proceedings of 16th International Conference on Ground Penetrating Radar*, June 2016.

[35] F. Abujarad, "Ground penetrating radar signal processing for landmine detection," Ph.D. dissertation, Otto-von-Guericke Universitat, Madgeburg, 2007.

[36] S. Tjora, E. Eide, and L. Lundheim, "Evaluation of methods for ground bounce removal in gpr utility mapping," in *Proceedings of 10th International Conference on Ground Penetrating Radar*, 2004, pp. 379–382.

[37] R. Abrahamsson, E. G. Larssonaf, J. Li, J. Habersatb, G. Maksymonkob, and M. Bradley, "Elimination of leakage and ground bounce effects in ground penetrating radar data," in *IEEE Signal Processing Workshop on Statistical Signal Processing*, 2001.

[38] R. Wu, A. Clement, J. Li, E. G. Larsson, M. Bradley, J. Habersat, and G. Maksymonko, "Adaptive ground bounce removal," *IEEE Electronic Letters*, vol. 37, no. 20, p. 2000, February 2001.

[39] A. van der Merwe and I. J. Gupta, "A novel signal processing technique for clutter reduction in gpr measurements of small, shallow land mines," *IEEE Transactions on Geoscience and Remote Sensing*, vol. 38, no. 6, November 2000.

[40] A. H. Gunatilaka and B. A. Baertlein, "A subspace decomposition technique to improve gpr imaging of anti-personnel mines," in *Proceedings of SPIE 4038, Detection and Remediation Technologies for Mines and Minelike Targets V*, 2000.

[41] W. H. Lee, P. Gader, J. N. Wilson, R. Weaver, S. Bishop, P. Gugino, and P. Howard, "Ground-tracking for on and off-road detection of landmines with ground penetrating radar," in *24th Army Science Conference*, 2004.

[42] P. Torrione and L. Collins, "Ground response tracking for improved landmine detection in ground penetrating radar data," in *Proceedings of IEEE International Conference on Geoscience and Remote Sensing Symposium*, 2006, pp. 153–156.

[43] B. Karlsen, J. Larsen, H. B. D. Sorensen, and K. B. Jakobsen, "Comparison of pca and ica based clutter reduction in gpr systems for anti-personal landmine detection," in *Proceedings ofthe 11th IEEE Signal Processing Workshop on Statistical Signal Processing*, 2001, pp. 146–149.

[44] M. P. Masarik, J. Burns, B. T. Thelen, J. Kelly, and T. C. Havens, "Gpr anomaly detection with robust principal component analysis," in *Proceedings of Detection and Sensing of Mines, Explosive Objects, and Obscured Targets XX*, vol. 9454. SPIE, 2015.

[45] M. Ohki and S. Hashiguchi, "Two dimensional lms adaptive filters," *IEEE Transactions on Consumer Electronics*, vol. 37, no. 1, p. 66, February 1991.

[46] A. Dyana, C. H. Srinvinas Rao, and R. Kuloor, "Segmentation of ground penetrating radar data for landmine detection," in *Proceedings of 14th International Conference on Ground Penetrating Radar*, 2012.

[47] P. A. Fferench, J. R. Zeidler, and W. H. Ku, "Enhanced detectability of small objects in correlated clutter using an improved 2-d adaptive lattice algorithm," *IEEE Transactions on Image Processing*, vol. 6, no. 3, p. 383, March 1997.

[48] B. Baydar, G. Bozdagi Akar, S. E. Yuksel, and S. Ozturk, "Fusion of klms and blob based pre-screener for buried landmine detection using ground penetrating radar," in *Proceedings of SPIE 9823, Detection and Sensing of Mines, Explosive Objects, and Obscured Targets XXI*, 2016.

[49] B. Baydar and G. Bozdagi Akar, "A novel adaptive pre screener for ground penetrating radar," in *Proceedings of 24th Signal Processing and Communication Application Conference (SIU)*, 2016.

[50] A. Ganesh, Z. Lin, J. Wright, L. Wu, M. Chen, and Y. Ma, ""fast algorithms for recovering a corrupted low-rank matrix," in *3rd IEEE International Workshop on Computational Advances in Multi-Sensor Adaptive Processing (CAMSAP)*, 2009, pp. 213–216.

[51] A. C. Gurbuz and J. H. McClellan, "Iterative detection of linear objects in gpr and seismic images," in *4th IEEE Workshop on Sensor Array and Multichannel Processing*, 2006, pp. 118–121.

[52] F. Cremet, W. D. Jong, and K. Schutte, "Fusion of polarimetric infrared features and gpr features for landmine detection," in *2nd International Workshop on Advanced GPR*, May 2003, pp. 222–227.

[53] I. K. Lee, "Curve reconstruction from unorganized points," Institute of Geometry, Vienna University of Technology, Tech. Rep., 1998.

[54] S. W. Cheng, S. Funke, M. Golin, P. Kumar, S. H. Poon, and E. Ramos, "Curve reconstruction from noisy samples," *Computational Geometry*, vol. 31, pp. 63–100, 2005.

[55] G. S. Kumar, P. K. Kalra, and S. G. Dhande, "Curve and surface reconstruction from points: and approach based on self-organizing maps," *Applied Soft Computing*, vol. 5, pp. 55–66, 2004.

[56] L. Van Kempen, H. Sahli, and J. Cornelis, "Signal processing and pattern recognition methods for radar ap mine detection and identification," in *Proceedings of 2nd International Conference on Detection of Abandoned Land Mines.* IEE, 1998, pp. 81–85.

[57] J. N. Wilson, P. Gader, W. H. Lee, H. Frigui, and K. C. Ho, "A large scale systematic evaluation of algorithms using ground penetrating radar for landmine detection and discrimination," *IEEE Transactions on Geoscience and Remote Sensing*, vol. 45, no. 8, pp. 2560–2572, August 2007.

[58] P. Gader, W. H. Lee, and J. N. Wilson, "Landmine detection with ground penetrating radar using hidden markov models," *IEEE Transactions on Geoscience and Remote Sensing*, vol. 39, no. 6, p. 1231, June 2001.

[59] S. Theodoridis and K. Koutroumbas, *Pattern Recognition*, 4th ed. Academic Press, Elsevier Inc., 2008.

[60] R. C. Gonzalez and R. E. Woods, *Digital Image Processing.* Prentice Hall Inc., 2002.

APPENDIX A

LIST OF C-SCAN SIMULATIONS

The table below presents the C-scan simulations generated to measure the performance of utilized algorithms in Chapter 4 and 5. There are 60 C-scan simulations in total. In the geometry column, the top-down looking geometries of the 3-D environment are presented. In the pre-screener and reconstructed curves column, the energy maps of the utilized pre-screener outputs are presented in gray scale; using the method described in Equation 4.3 given in Chapter 4. The contrast is deliberately adjusted such that the zero energy locations have gray color rather than black; considering the printing quality. The reconstructed curves are also presented in these figures. The blue curves represent the detections labelled as wire and red curves represent the detections labelled as clutter. Note that, in case of a collision of wire with a clutter object, the curve is labelled as wire again.

In the geometries, the thin dark blue lines represent the wires, light blue circles represent the rocks, dark blue big circles are modelled as landmine and red objects are plastics, modelled as clutter and wire commanded IED simultaneously.

The detection threshold of prescreener is adjusted differently for each simulations intentionally in order to make all wires detected and in order to minimize the clutter collisions. These simulations are used for evaluating the performance of preprocessing and classification algorithms. The results are presented at the ends of Chapter 4 and 5.

TableA.1: List of C-scan simulations

Number	Geometry	Pre-screener output and Reconstructed curves
01	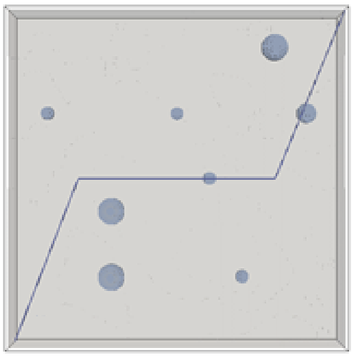	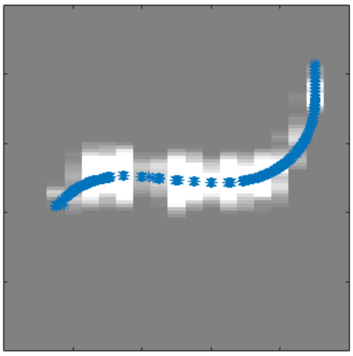
02	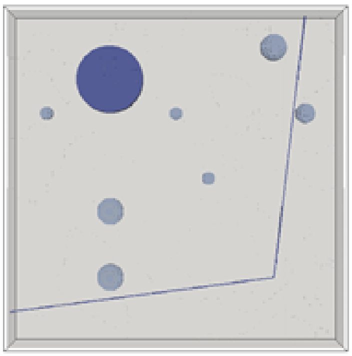	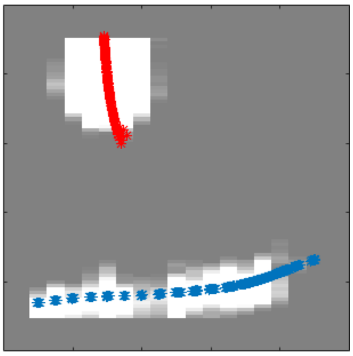
03	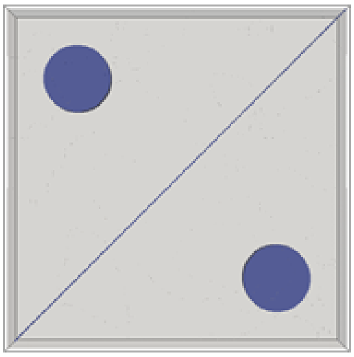	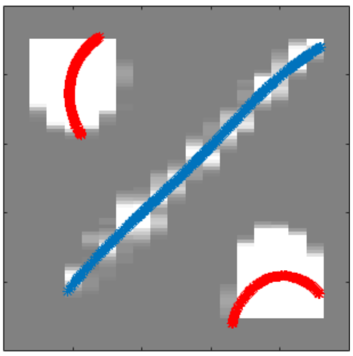
04	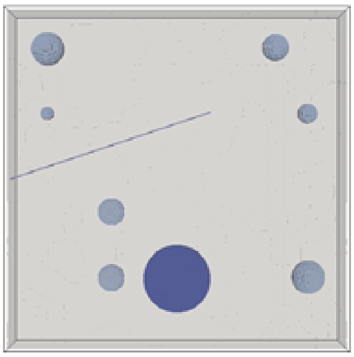	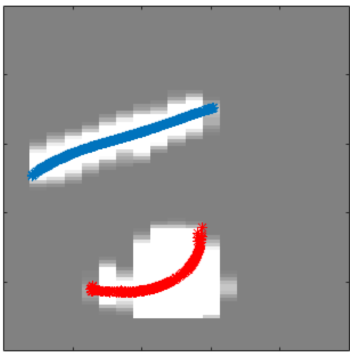

TableA.1: List of C-scan simulations - Continued

Number	Geometry	Pre-screener output and Reconstructed curves
05	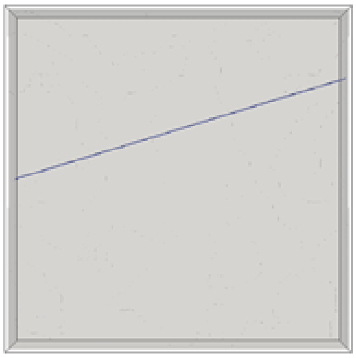	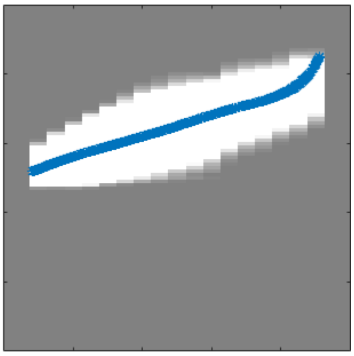
06	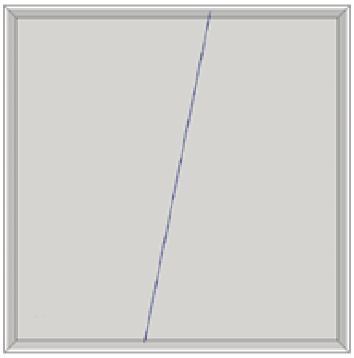	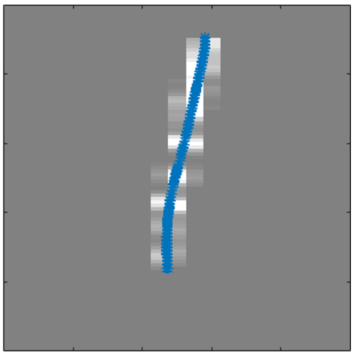
07	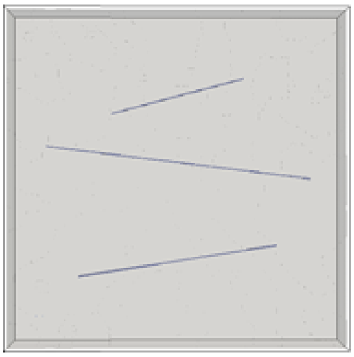	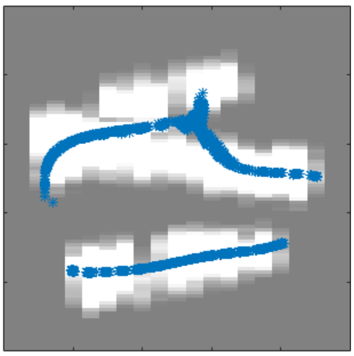
08	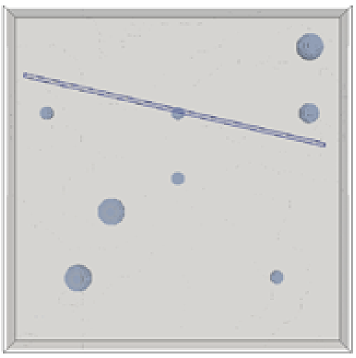	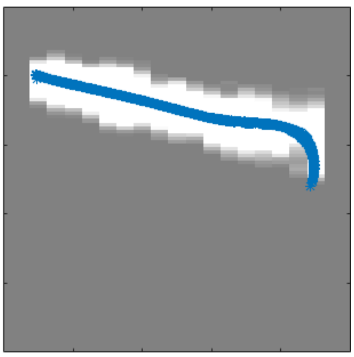

TableA.1: List of C-scan simulations - Continued

Number	Geometry	Pre-screener output and Reconstructed curves
09	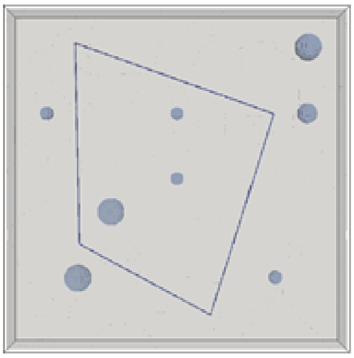	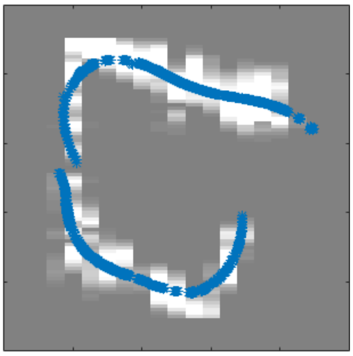
10	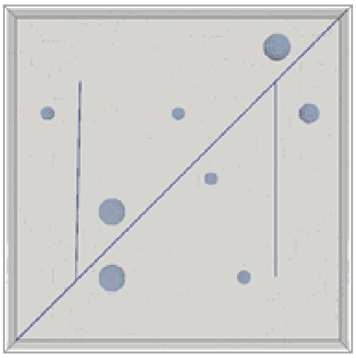	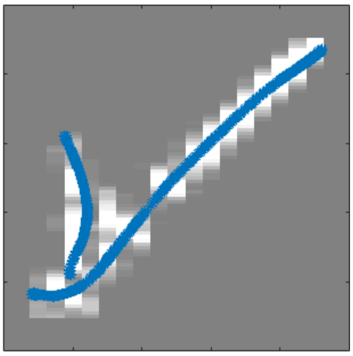
11	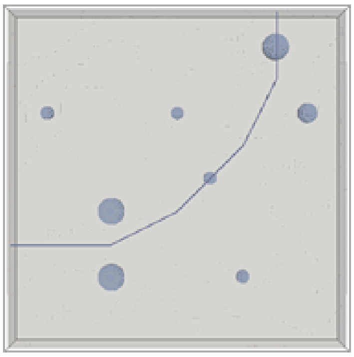	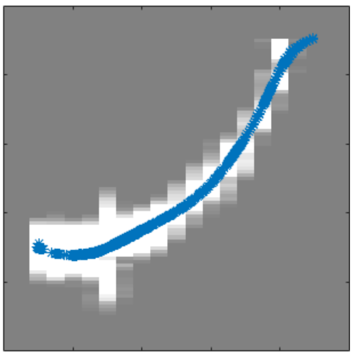
12	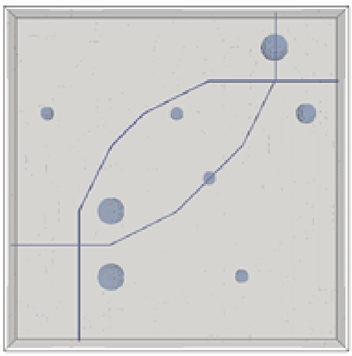	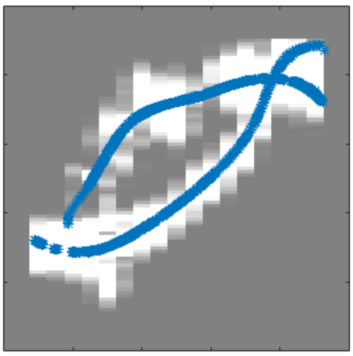

TableA.1: List of C-scan simulations - Continued

Number	Geometry	Pre-screener output and Reconstructed curves
13	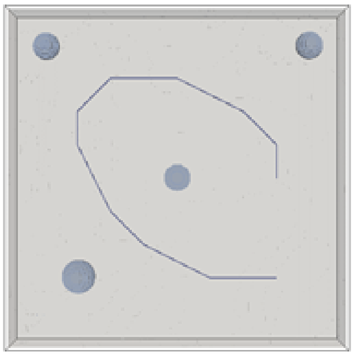	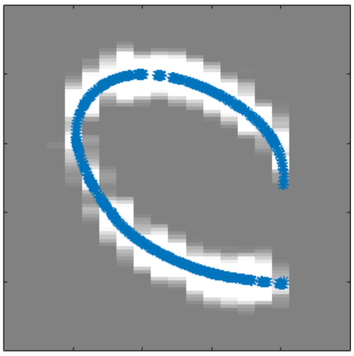
14	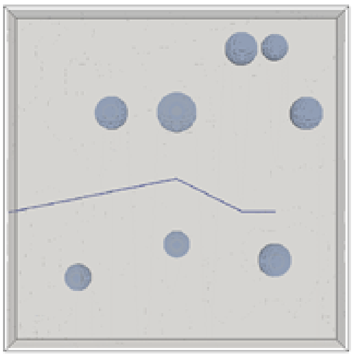	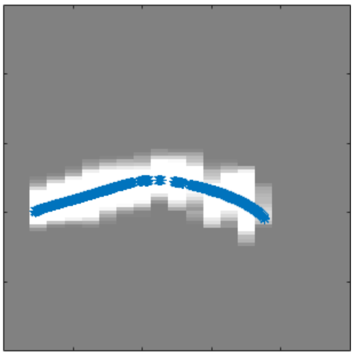
15	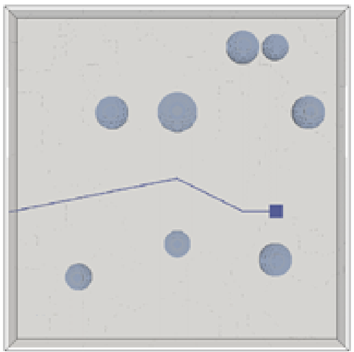	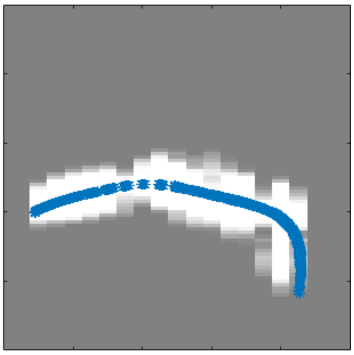
16	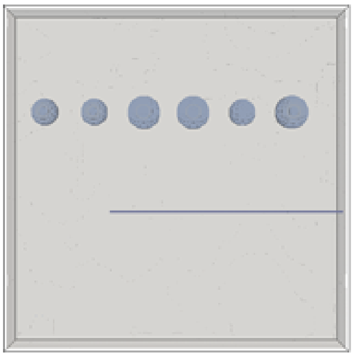	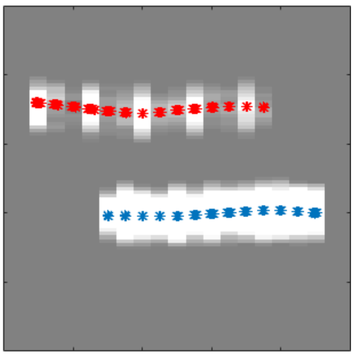

TableA.1: List of C-scan simulations - Continued

Number	Geometry	Pre-screener output and Reconstructed curves
17	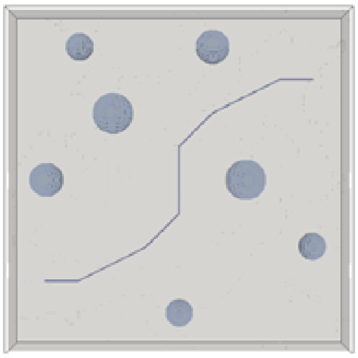	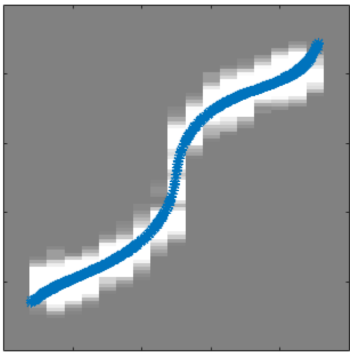
18	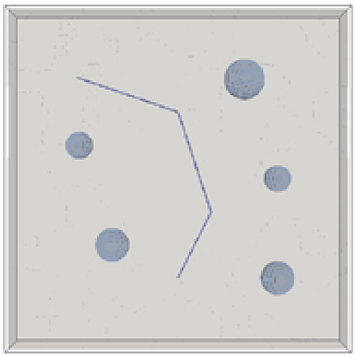	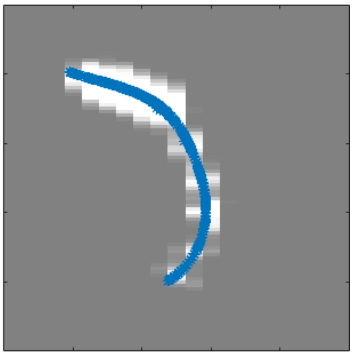
19	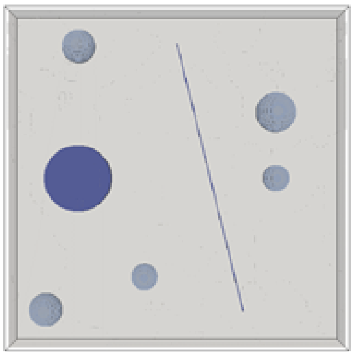	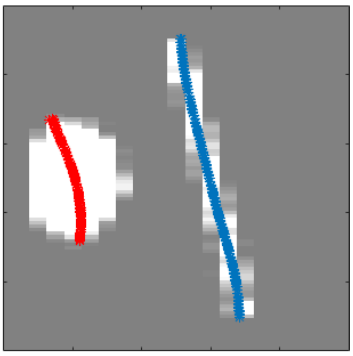
20	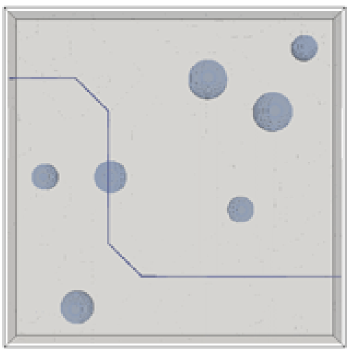	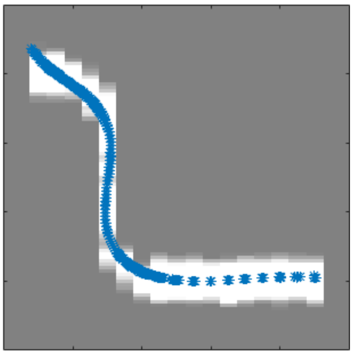

TableA.1: List of C-scan simulations - Continued

Number	Geometry	Pre-screener output and Reconstructed curves
21	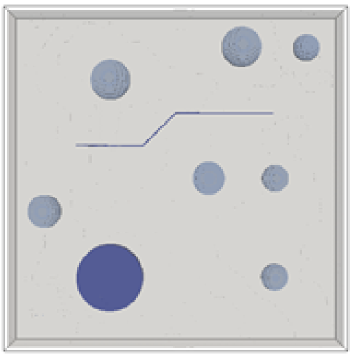	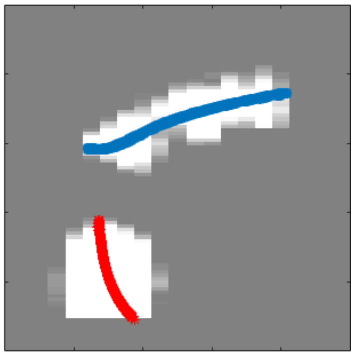
22	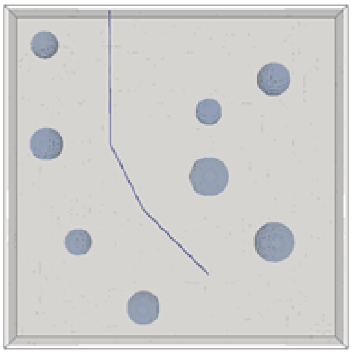	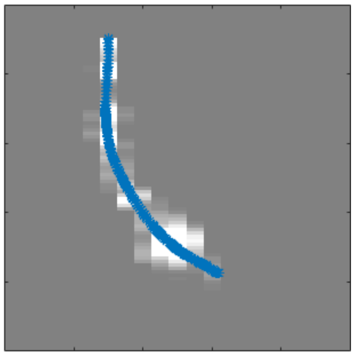
23	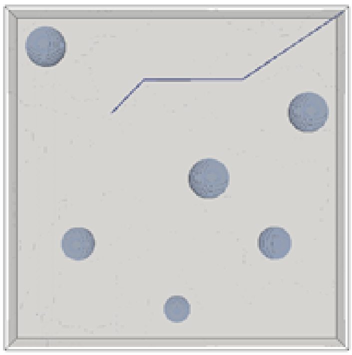	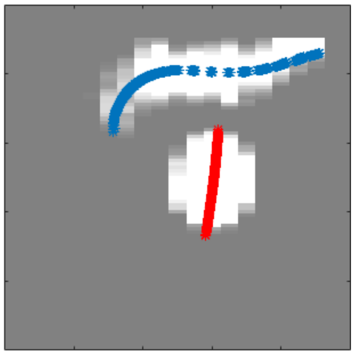
24	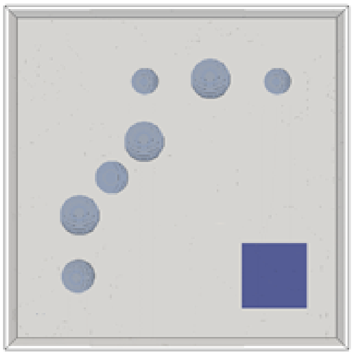	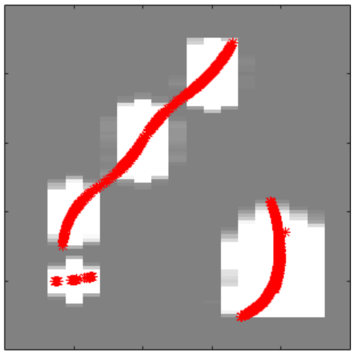

TableA.1: List of C-scan simulations - Continued

Number	Geometry	Pre-screener output and Reconstructed curves
25	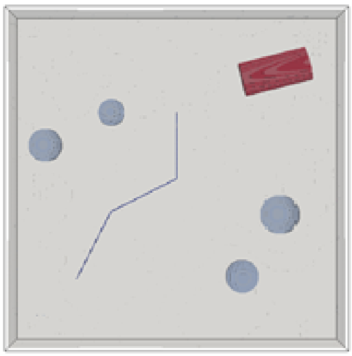	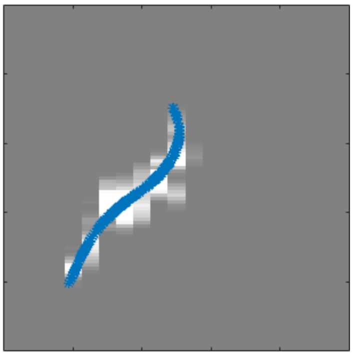
26	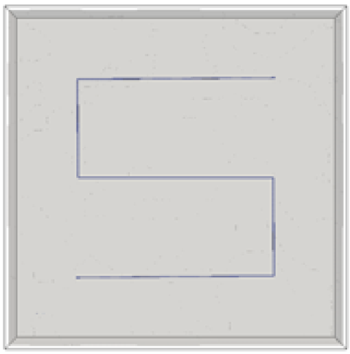	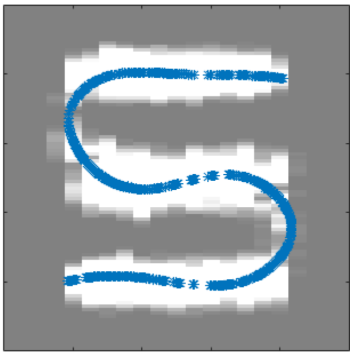
27	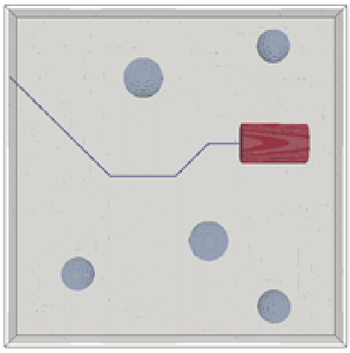	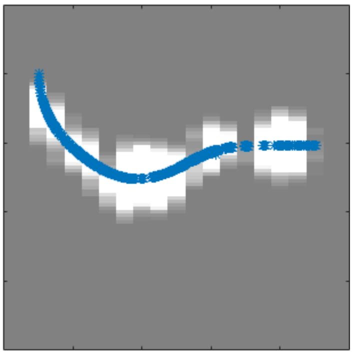
28	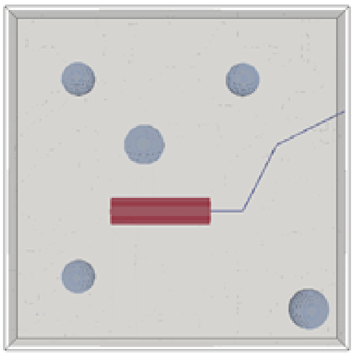	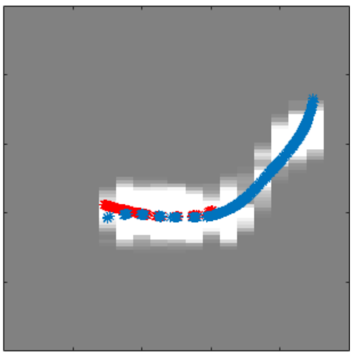

TableA.1: List of C-scan simulations - Continued

Number	Geometry	Pre-screener output and Reconstructed curves
29	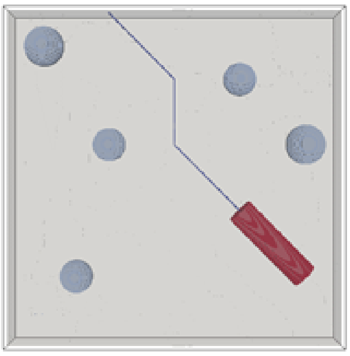	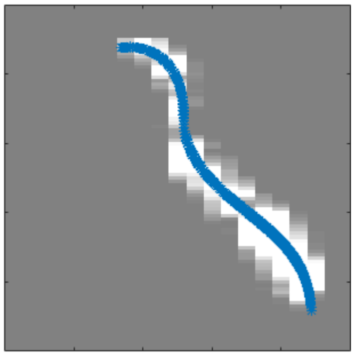
30	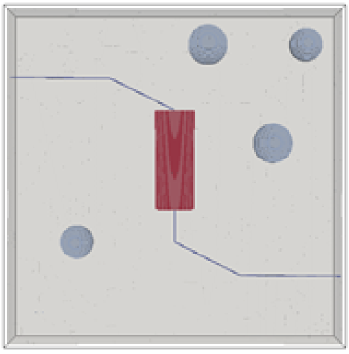	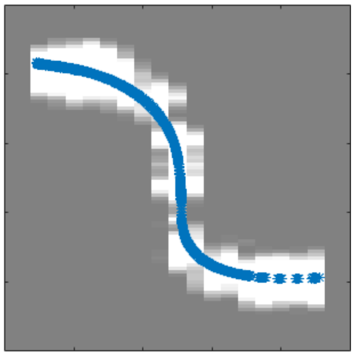
31	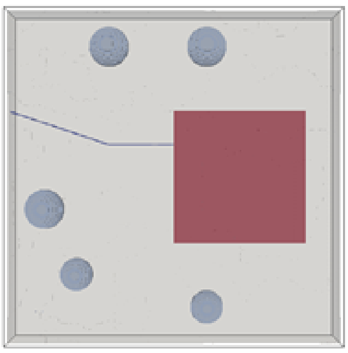	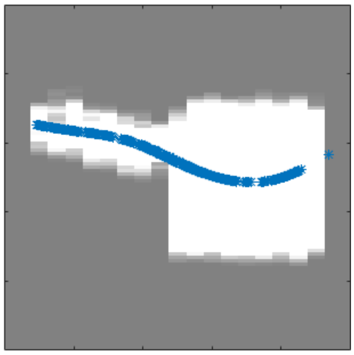
32	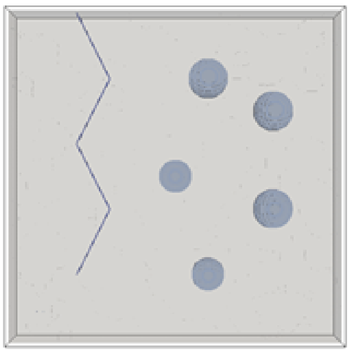	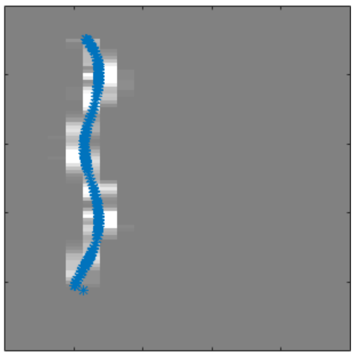

TableA.1: List of C-scan simulations - Continued

Number	Geometry	Pre-screener output and Reconstructed curves
33	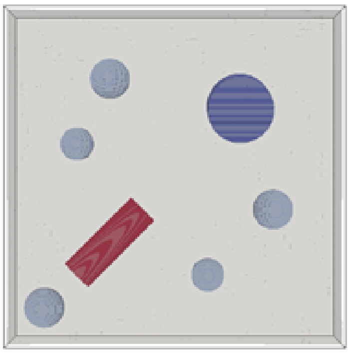	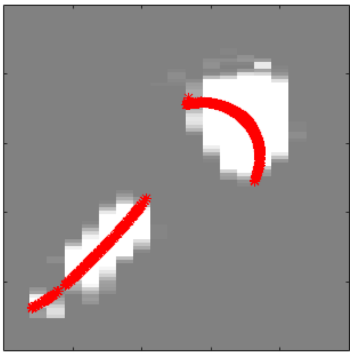
34	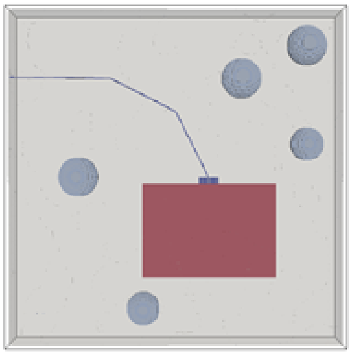	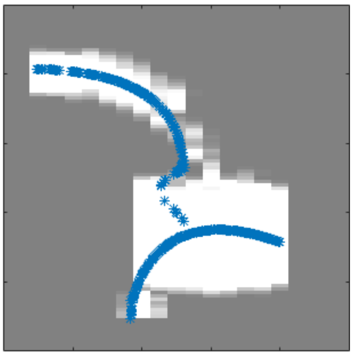
35	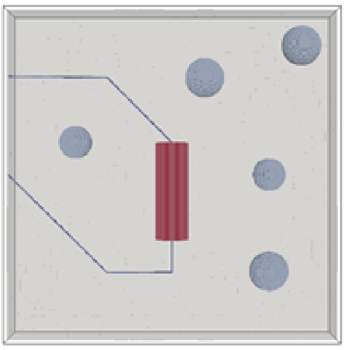	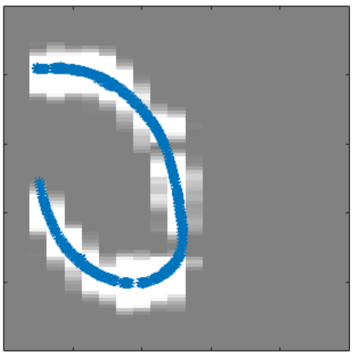
36	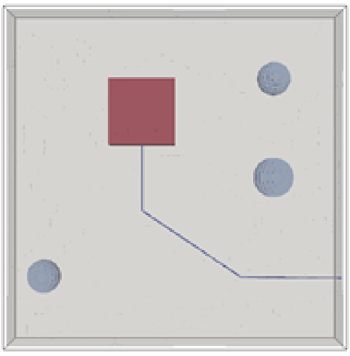	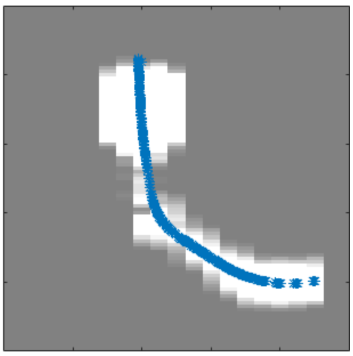

TableA.1: List of C-scan simulations - Continued

Number	Geometry	Pre-screener output and Reconstructed curves
37	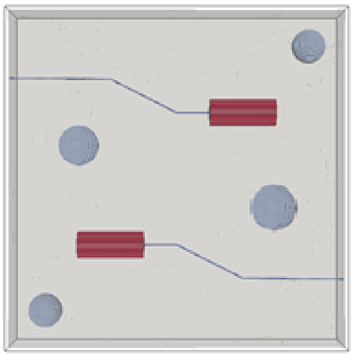	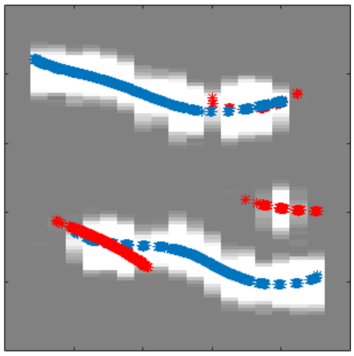
38	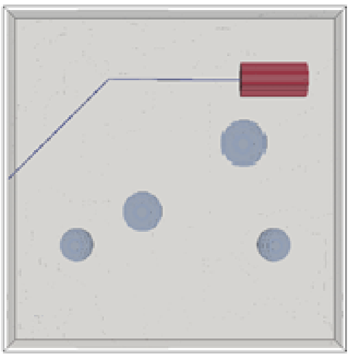	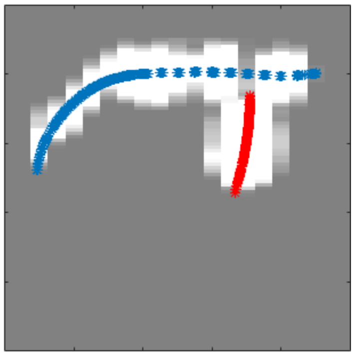
39	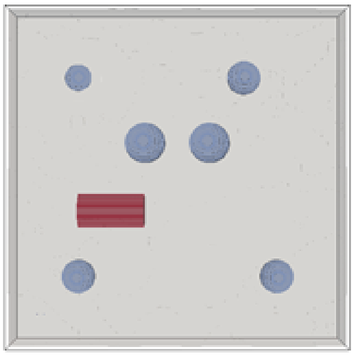	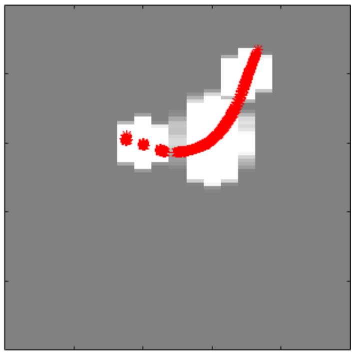
40	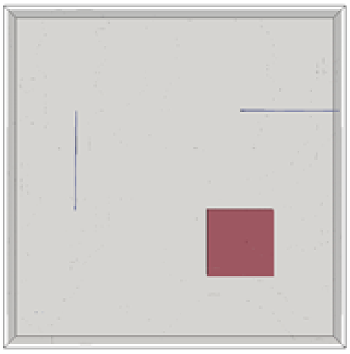	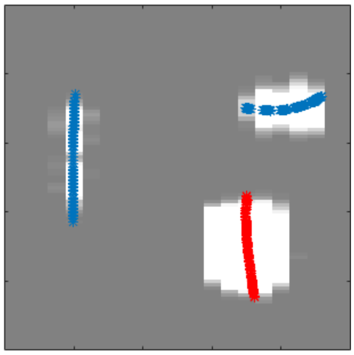

TableA.1: List of C-scan simulations - Continued

Number	Geometry	Pre-screener output and Reconstructed curves
41	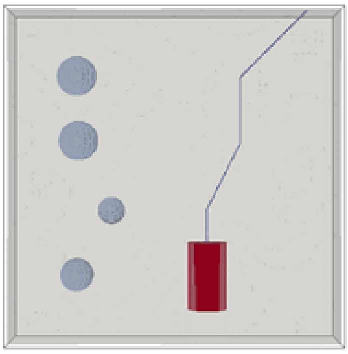	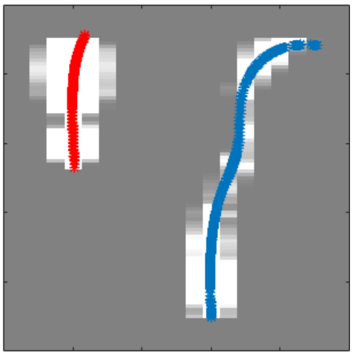
42	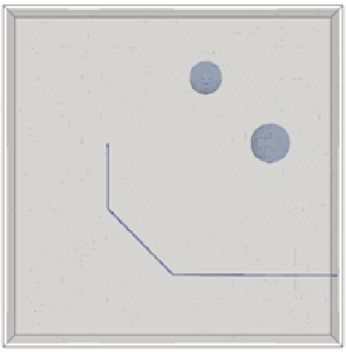	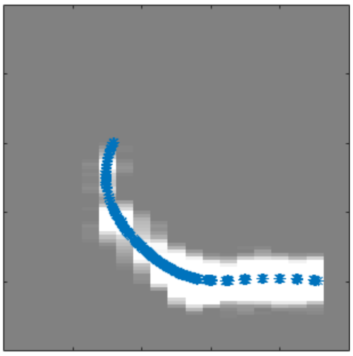
43	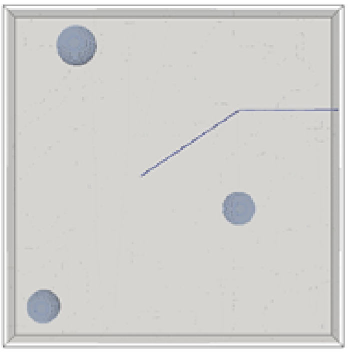	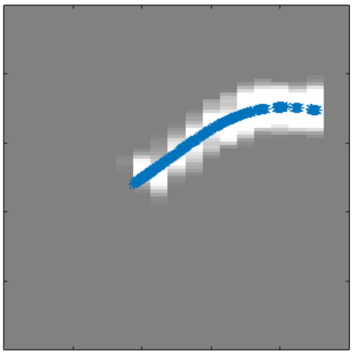
44	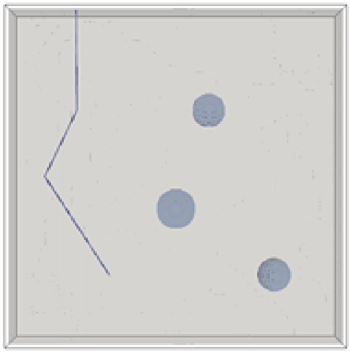	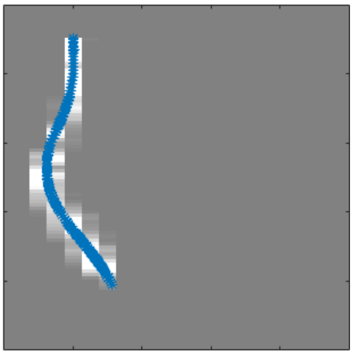

TableA.1: List of C-scan simulations - Continued

Number	Geometry	Pre-screener output and Reconstructed curves
45	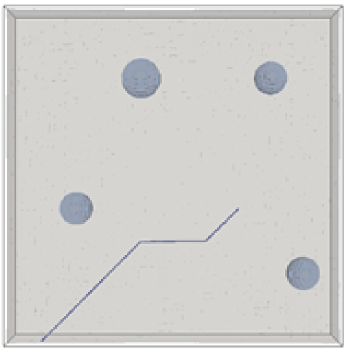	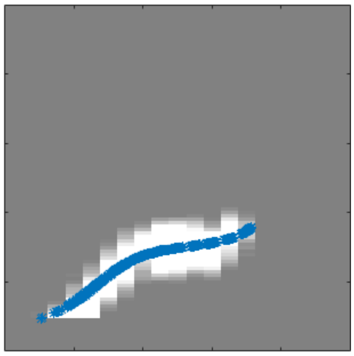
46	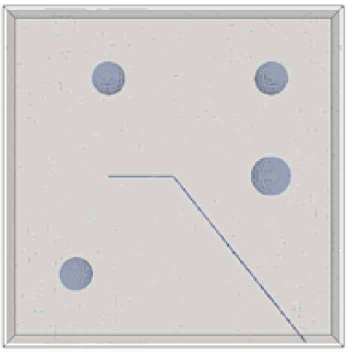	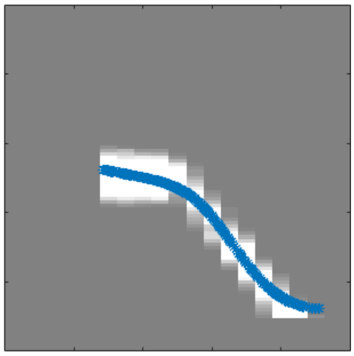
47	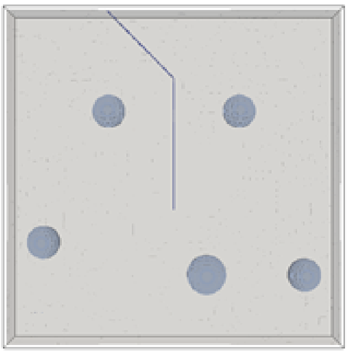	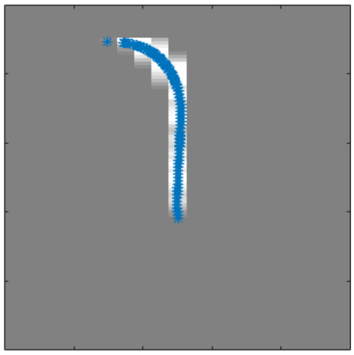
48	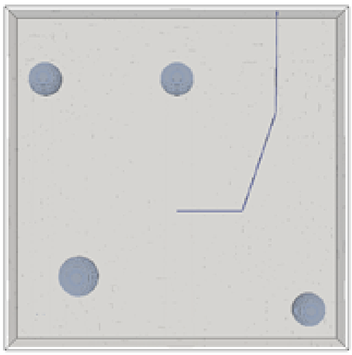	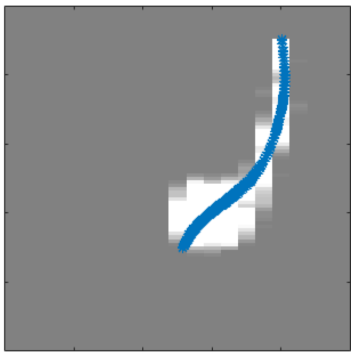

TableA.1: List of C-scan simulations - Continued

Number	Geometry	Pre-screener output and Reconstructed curves
49	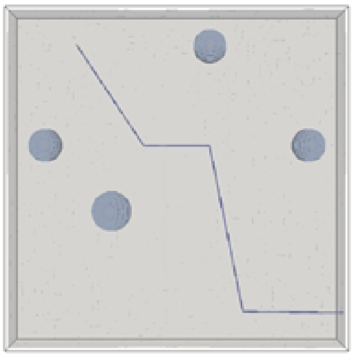	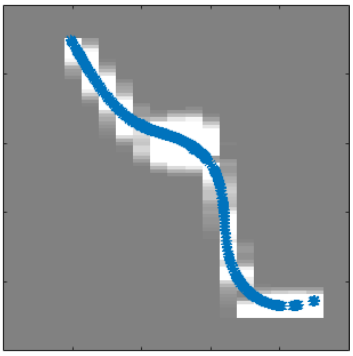
50	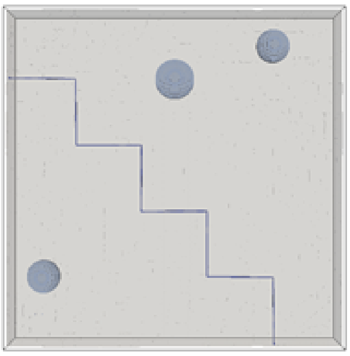	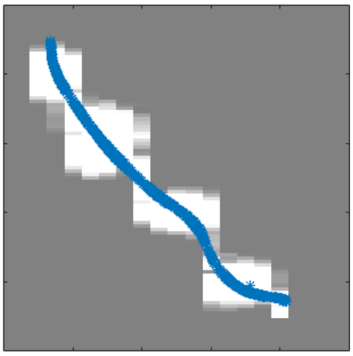
51	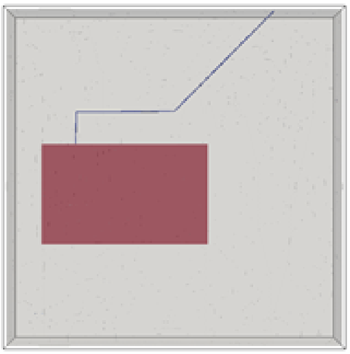	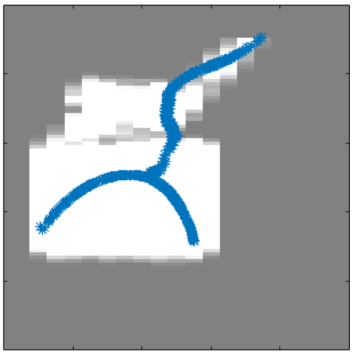
52	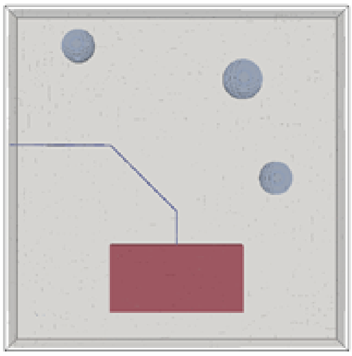	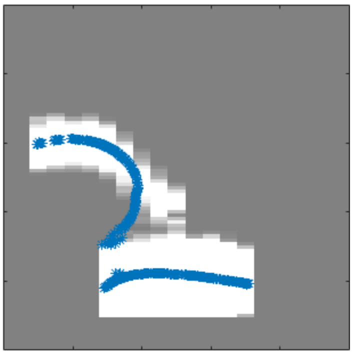

TableA.1: List of C-scan simulations - Continued

Number	Geometry	Pre-screener output and Reconstructed curves
53	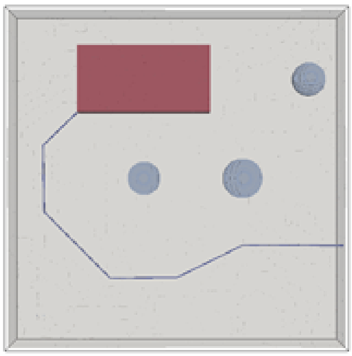	
54	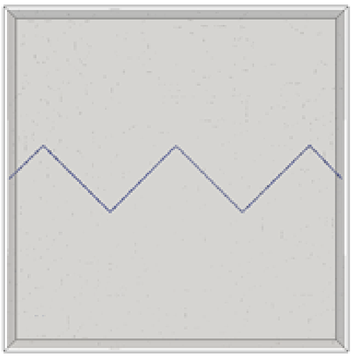	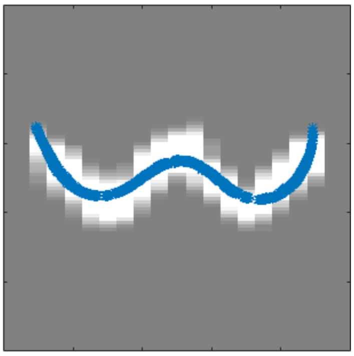
55	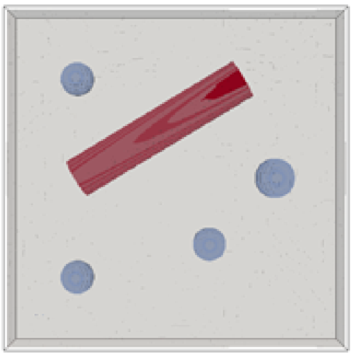	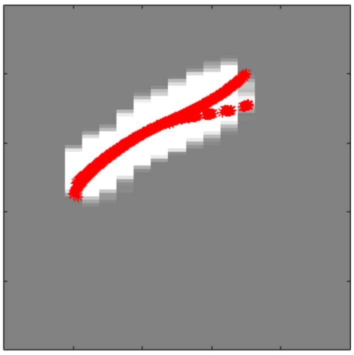
56	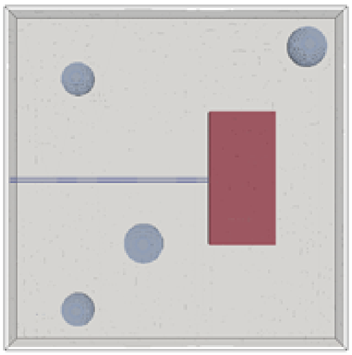	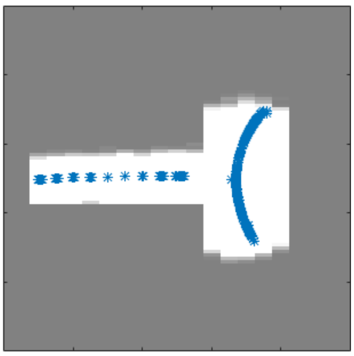

TableA.1: List of C-scan simulations - Continued

Number	Geometry	Pre-screener output and Reconstructed curves
57	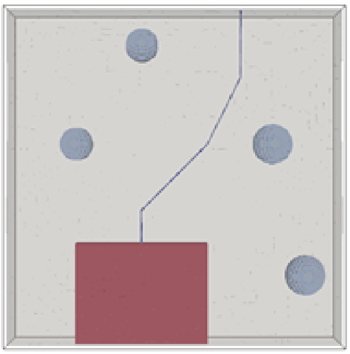	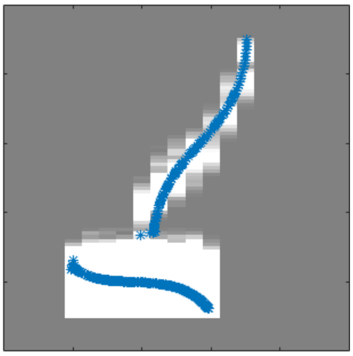
58	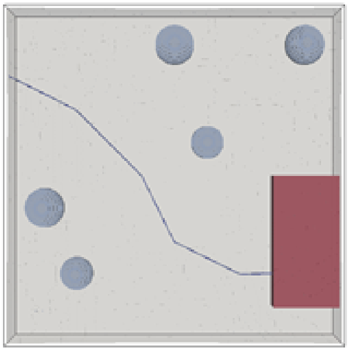	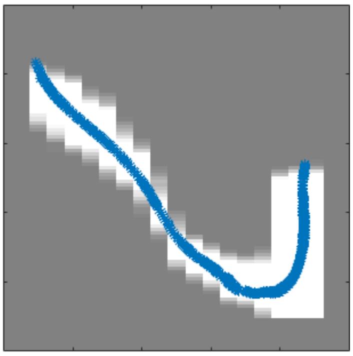
59	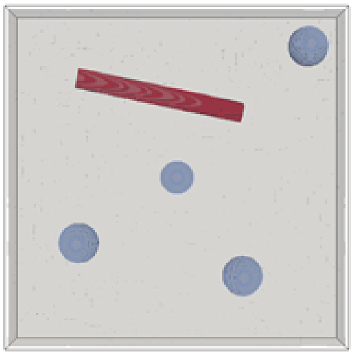	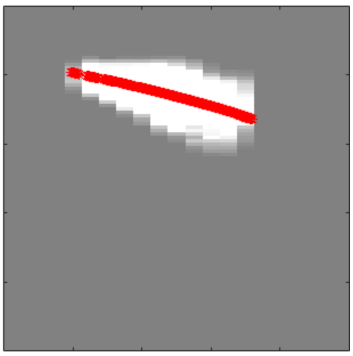
60	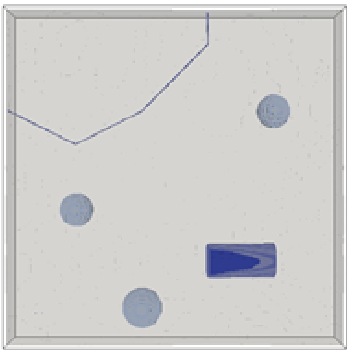	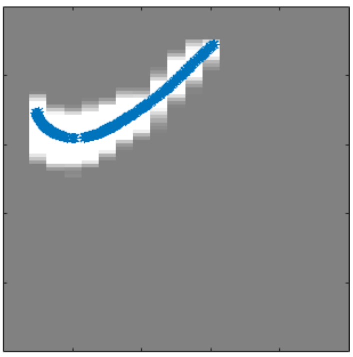

APPENDIX B

GPRMAX INPUT FILES

B.1 B-scan input file

The default simulation environment defined in Table 3.1 is generated with gprMax software, using the following script. The script is evaluated with the stepping parameter of 31.

```
#title: Bscan001
#domain: 0.30 0.50 0.15
#dx_dy_dz: 1e-3 1e-3 1e-3
#time_window: 7.5e-9
#num_threads: 8
#material: 6 1e-5 4 1e-2 soilX
#box: 0 0 0 0.30 0.50 0.10 soilX
#cylinder: 0 0.25 0.05 0.30 0.25 0.05 0.002 pec
#waveform: gaussiandot 1.00 2.5e9 src1
#hertzian_dipole: x 0.13 0.10 0.12 src1
#rx: 0.17 0.10 0.12
#src_steps: 0.00 0.01 0.00
#rx_steps: 0.00 0.01 0.00
```

B.2 C-scan input file

The 4^{th} C-scan simulation in the Appendix A is used for presenting the result of algorithms in Chapter 4 and Chapter 5. Its geometry is presented in Figure 4.1. The data of first T/R pair is generated with gprMax software, using the following script. The script is evaluated with the stepping parameter of 81. There are 17 scripts in total, evaluated in parallel in the HPC system provided by Aselsan for obtaining C-scan.

```
#title: Cscan004
#domain: 1 1 0.20
#dx_dy_dz: 2e-3 2e-3 2e-3
#time_window: 4e-9
#num_threads: 8
#material: 5 1e-4 5 1e-2 rockX
#soil_peplinski: 0.5 0.5 2.0 2.66 0.001 0.25 my_soil
#fractal_box: 0 0 0 1 1 0.15 1.5 1 1 1 50 my_soil soilBox 20
#add_surface_roughness: 0 0 0.15 1 1 0.15 1.5 1 1 0.140 0.150 soilBox 120
#cylinder: 0  0.5  0.1  0.6 0.7  0.1 0.002 pec
#sphere: 0.3 0.2 0.07 0.04 rockX
#sphere: 0.3 0.4 0.07 0.04 rockX
#sphere: 0.9 0.2 0.05 0.05 rockX
#sphere: 0.8 0.9 0.05 0.04 rockX
#sphere: 0.1 0.7 0.03 0.02 rockX
#sphere: 0.9 0.7 0.03 0.03 rockX
#sphere: 0.1 0.9 0.02 0.05 rockX
#cylinder: 0.5  0.2  0.05  0.5  0.2  0.10 0.10 pec
#waveform: gaussiandot 1.00 2.5e9 src1
#hertzian_dipole: x 0.11 0.10 0.18 src1
#rx: 0.09 0.10 0.18
#src_steps: 0.00 0.01 0.00
#rx_steps: 0.00 0.01 0.00
```

APPENDIX C

TOOLS USED FOR IMPROVING 2-D LMS

C.1 Connected Component Analysis

Connected component analysis is a powerful tool to identify and separate the connected points in 3-D space. A target will have a group of connected points in the C-scan GPR data. The connected component analysis groups the points that are connected with each other in terms of the neighbourhood definition. The connected component analysis in 3-D is performed using the 6, 18 and 26 neighbourhoods in general. The neighbourhood definitions are presented in Figure C.1. While the point of interest is located at the center of these cubes, the points inside the defined neighbourhood are considered to be connected with the point of interest. Starting from a random point in 3-D space, the point cloud of whole connected component can be found. Since, the temporal resolution in along depth axis is considerably good; the effect of different neighbourhoods are minimal. In the following algorithm, 18 connected neighbourhood is used for connected component analysis.

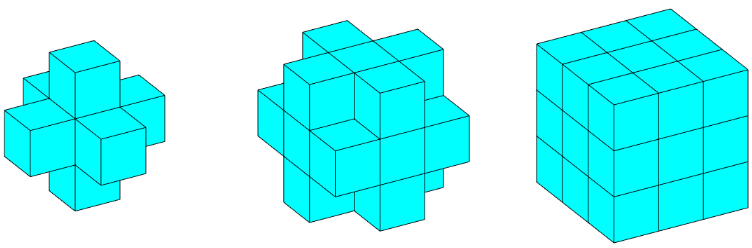

Figure C.1: Connectivity options of connected component analysis, 6 connected neighbourhood (left), 18 connected neighbourhood (middle) and 26 connected neighbourhood (right).

C.2 Mathematical Morphologies

Mathematical morphologies are useful tools in image processing. By applying these morphologies, distortions in the image can be reduced further [60]. These operations have been applied on binary detections, but they might be applied on the gray scale 3-D images as well.

C.2.1 Erosion

Erosion operation is one of the mathematical morphologies utilized in Algorithm 8, which erodes the outer border of the detection group and shrinks the volume of the point data, using the 3-D structuring element **se**. The structuring element was a binary cuboid in 3-D. Its lengths in along-track and cross-track dimensions are selected as 2, and length along depth axis is selected as 40 samples which are enough to get the secondary signals in the GPR signatures. The erosion operation is symbolised with a sign shown in Equation C.1, where **A** is the original 3-D image and **B** is the eroded 3-D image.

$$\mathbf{B} \leftarrow \mathbf{A} \ominus \mathbf{se} \tag{C.1}$$

C.2.2 Dilation

Dilation operation is the other mathematical morphology utilized in Algorithm 8, which dilates the outer border of the detection group. On the contrary to image erosion, dilation expands the volume of the point data, using the 3-D structuring element. The dilation operation is symbolised with a sign shown in Equation C.2, where **A** is the original 3-D image, **se** is the 3-D structuring element and **B** is the 3-D dilated image.

$$\mathbf{B} \leftarrow \mathbf{A} \oplus \mathbf{se} \tag{C.2}$$